UNIVERSITY OF COPENHAGEN
FACULTY OF SCIENCE

PhD Thesis

Near-infrared spectroscopy in the Extremely Large Telescope era

Atmospheric and instrumentational limits

J. K. M. Viuho

Supervised by J. P. U. Fynbo and M. I. Andersen

2nd December 2025
This thesis has been submitted
to the PhD School of The Faculty of Science,
University of Copenhagen

J. K. M. Viuho

Near-infrared spectroscopy in
the Extremely Large Telescope era

PhD Thesis, 2nd December 2025
This thesis has been submitted
to the PhD School of The Faculty of Science,
University of Copenhagen
Supervisors: J. P. U. Fynbo and M. I. Andersen

University of Copenhagen
Faculty of Science
Niels Bohr Institute, The Cosmic Dawn Center
Jagtvej 155A, 02.2.I.152
2200 Copenhagen N

"*Why not let us compromise*
about Denmark's proper size,
which will truly please us all,
since it's bigger than it's small."

– Piet Hein

Acknowledgements

First and foremost I would like express my gratitude towards my advisors Johan Fynbo and Michael I. Andersen for offering me a possibility to work on a such an intriguing project as this thesis has been. It has been a journey. You have been an inspirational role models for me, and will remain as such in the future.

I am very grateful for the time that you Michael I. Andersen and Anton Sørensen have spent to teach me the craft of astronomical instrument building. I would like to specially thank to Niels Michaelsen for manufacturing mechanical parts for the SKITLES spectrograph, and Akke Viitanen and Nicholas Jannsen for helping to develop control software for it. I would like to thank the past and present staff at the Nordic Optical Telescope, Sergio Armas, Thomas Augusteijn, Peter Brandt, Jacob Clasen, Graham Cox, Amanda Djupvik, Loida Fernández, Raquel López, Christian Moreno, Carlos Perez, Tapio Pursimo, Peter Sørensen, and Petri Väisänen, for hosting my equipment at the NOT facilities and enabling the data acquisition with the NOT. Over the past years, it has been a pleasure to work with you NTE team in Copenhagen, Aarhus, and Merate, Johan Fynbo, Jacob Clasen, Michael I. Andersen, Anton Sørensen, Lise Christensen, Bo Milvang-Jensen, Dennis Wistisen, Simon Fassel, Michael Bernt, Niels Michaelsen, John Andersen, and Marcello Scalera.

Finally, I would like to thank Jacob Clasen and Anton Sørensen for the numerous conversations over the years, James Munday and Akke Viitanen on their feedback, and Viktoria Pinter for her unwavering support and infinite patience.

Abstract

Historically, the astronomical spectroscopy has been limited by the detector noise. With the introduction of 10-meter class telescopes and the advances in several different detector technologies over the past two decades, the astronomical spectroscopy has become photon noise limited in the visible (VIS, 0.3 – 0.7 μm), the near infrared (NIR, 0.7 – 1.1 μm), and the shortwave infrared (SWIR, 1.1 – 2.5 μm) wavelengths. At the same time, the interest towards understanding the atmospheric radiation processes has grown within the astronomical community, due to the atmospheric foreground radiance limiting the scientific achievements of the 40-meter Extremely Large Telescopes.

The line emission processes are understood to a point that sophisticated models can be developed. On the other hand, the origin and behavior the airglow continuum, one of the key constituents to the night sky emission, has remained poorly understood. Despite its faintness, the airglow continuum will be the brightest continuum source, along with the zodiacal light, affecting ground-based astronomy under the dark sky conditions devoid of lunar and artificial illumination. The reasons for the poor understanding of the airglow continuum and the physical processes behind it is due to,

1. *the airglow continuum being faint,*
2. *and variable on a large range of timescales from minutes to decades,*
3. *and its modeling and analysis requiring cross-disciplinary research.*

The first point sets stringent requirements on the instrument design, especially in terms of grating scattered light in case of spectroscopy, and off-band blocking in case of narrow band photometry.

Two novel optical methods for controlling the instrumental stray light are presented: a new spectrograph design in Article I, and a shortpass filter not used before in Article III. The difficult to characterize airglow continuum is measured in Articles II, III, and IV.

Article II measures the airglow continuum surface brightness at the site of Observatorio del Roque de los Muchachos, La Palma, Spain with a method that limits the effect of grating scattered light. Article III studies a novel technique for suppressing the thermal emission from the sky and instrumentation, and also measures the airglow continuum at longer wavelengths in the NIR than was possible in Article II. Finally, Article IV uses the novel spectrograph presented in Article I for on-sky measurement of the airglow continuum at the Observatorio del Roques de los Muchachos. This thesis itself summarizes the state-of-the-art in the understanding of the chemiluminescent processes behind the airglow continuum.

Dansk resumé

Historisk set har astronomisk spektroskopi været begrænset af detektorstøj. Med introduktionen af 10-meter teleskoper og fremskridtene inden for flere forskellige detektorteknologier i løbet af de sidste to årtier er astronomisk spektroskopi blevet fotonstøjbegrænset i det synlige område (VIS, 0.3-0.7 μm), det nære infrarøde område (NIR, 0.7-1.1 μm) og det kortbølgede infrarøde område (SWIR, 1.1-2.5 μm). Samtidig er interessen for at forstå de atmosfæriske strålingsprocesser vokset inden for det astronomiske samfund på grund af den atmosfæriske forgrundsstråling, der begrænser de videnskabelige resultater med 40-meter Extremely Large Telescopes.

Linjeemissionsprocesserne er forstået i en sådan grad, at sofistikerede modeller kan udvikles. På den anden side er oprindelsen og opførslen af airglow-kontinuumet, en af nøglebestanddelene i nattehimlens emission, forblevet dårligt forstået. Trods sin svaghed, vil airglow-kontinuumet være den klareste kontinuumkilde, sammen med zodiakallyset, der påvirker, der påvirker jordbaseret astronomi under mørke himmelforhold uden måne og kunstig belysning. Årsagerne til den dårlige forståelse af airglow-kontinuumet og de fysiske processer bag det skyldes,

1. *airglow kontinuum er svagt,*
2. *og varierende over en lang række tidsskalaer fra minutter til årtier,*
3. *og dens modellering og analyse kræver tværfaglig forskning.*

Det første punkt sætter strenge krav til instrumentdesign, især med hensyn til spredt lys fra gitteret i tilfælde af spektroskopi og blokering uden for båndet i tilfælde af smalbåndsfotometri. To nye metoder til at kontrollere to forskellige

aspekter af det instrumentelle spredte lys præsenteres i Artikel I og Artikel III. Artiklerne II, III og IV har til formål at karakterisere airglow-kontinuumet.

Artikel I præsenterer et nyt spektrografkoncept, der ikke påvirkes af det gitterspredte lys, ideelt til måling af airglow-kontinuumet. Artikel II måler overfladelysstyrken på airglow-kontinuumet på Observatorio del Roque de los Muchachos, La Palma, Spanien med en metode, der begrænser effekten af spredt lys fra gitteret. Artikel III undersøger en ny teknik, der ikke er testet før, til at undertrykke termisk emission fra himlen og instrumenterne, og måler også airglow-kontinuumet dybere i NIR end det var muligt i artikel II. Endelig anvender anvender artikel IV (under forberedelse), den nye spektrograf der præsenteres i artikel I til måling af airglow kontinuummet på himlen ved Observatorio del Roques de los Muchachos. Denne afhandling forsøger i sig selv at opsummere den aktuelle viden inden for forståelsen af de kemiluminescerende processer bag airglow kontinuummet.

Contents

Abbreviations

Chemical compounds

CO	Carbon monoxide
CO_2	Carbon dioxode
CH_4	Methane
FeO	Iron monoxide
HgCdTe	Mercury-Cadmium-Telluride
H_2O	Water
HO_2	Hydroperoxyl
KH_2PO_4	Monopotassium dihydrogen phosphate, KDP
$K_2D_2PO_4$	Monopotassium dideuterium phosphate, D-KDP
NO	Nitrogen monoxide
NiO	Nickel monoxide
O_2	Oxygen
O_3	Ozone
OH	Hydroxyl

Acronyms

AR	Anti-reflection
AO	Adaptive Optics
APD	Avalanche Photo Diode
BRDF	Bidirectional Reflectance Distribution Function

CCD	Charge-Coupled Device
CDS	Correlated Double Sampling
CIB	Cosmic Infrared Background
CIC	Clock-Induced Charge
CIRPASS	the Cambridge Infra-red Panoramic Survey Spectrograph
CME	Coronal Mass Ejection
CMOS	Complementary Metal Oxide Semiconductor
COBE	COsmic Background Explorer
COHSI	the Cambridge OH Suppression Instrument
CTE	Charge Transfer Efficiency
DGL	Diffuse Galactic Light
DIRBE	(COBE) Diffuse Infrared Background Experiment
EMCCD	Electron Multiplication CCD
ELT	Extremely Large Telescope
ENF	Excess Noise Factor
ESO	European Southern Observatory
GDF	Grating Distribution Function
IPD	Inter-Planetary Dust
IR	InfraRed
IRAF	Image Reduction and Analysis Facility
IRAS	Infrared Astronomy Satellite
LED	Light Emitting Diode
LSF	Line Spread Function
MEC	MKID Exoplanet Camera (MEC)
MCT	Mercury-Cadmium-Telluride
MLT	Mesosphere-Lower Thermosphere
MKID	Microwave Kinectic Inductance Detector
MWIR	Mid-Wave InfraRed, 2.5 – 5 μm
NB	Narrow Band

NIR	Near InfraRed, 0.7 – 1.1μm
NOT	Nordic Optical Telescope
OHS	OH-airglow Suppressor
ORM	Observatorio Roque de los Muchachos
pCIC	parallel CIC
PDF	Probability Density Function
PMT	Photo Multiplier Tube
PSF	Point Spread Function
qCMOS	quantitative CMOS
QE	Quantum Efficiency
SAO	Semi-Annual Oscillation
SAID	SubAuroral Ion Drift
SAR	Stable Auroral Red arc
sCIC	serial CIC
SED	Spectral Energy Distribution
SNR	Signal-to-Noise Ratio
SNSPD	Superconductive Nanowire Single-Photon Detector
SKITLES	SKy Is The Limit Echelle Spectrograph
SPAD	Silicon Photo-Avalanche Diode
SQUID	Superconducting Quantum Interference Device
STEVE	Strong Thermal Emission Velocity Enhancement
STIS	Space Telescope Imaging Spectrograph
STJ	Superconductive Tunnel Junction
SWIR	Short-Wave InfraRed, 1.1 – 2.5μm
TES	Transition Edge Sensor
VIS	VISual, 0.3 – 0.7 μm
VLT	Very Large Telescope
ZL	Zodical Light

1 Introduction

At the dawn of the Extremely Large Telescope (ELT) era, the astronomical spectroscopy is becoming photon noise limited irrespective of the spectral resolution in the visible (VIS, 0.3 – 0.7 μm), the near infrared (NIR, 0.7 – 1.1 μm), and the shortwave infrared (SWIR, 1.1 – 2.5 μm) wavelengths. The dominant noise sources are moving away from the detectors, to the photon noise of the background, and to the photon noise of the instrumental stray light.

In astronomy, the term *background* collectively refers to all radiance that is originating from the object of interest, even though, a large majority of the *background* is emitted between the observer and the astronomical source, actually being a *foreground*. One of these *foreground* sources is the airglow, radiance from the atmospheric atoms and molecules. The term was coined by Otto Struve to distinguish between the atmospheric radiance, the zodiacal light, and the auroras (Elvey, 1950). In the earlier literature, the airglow is referred as *permanent aurora* or *non-polar aurora* due to their similarity in appearance.

The airglow consists of both line and continuum emission. The line emission is fairly well understood today, and even optical methods exist for filtering it away. On the other hand, a fair amount of uncertainty remains on the level and nature of the airglow continuum, which cannot be removed by instrumentation techniques. Since it cannot be optically removed, the only way to improve the signal-to-noise ratio in the presence of it, is to record multiple samples N of the background to bring the noise down to $1/\sqrt{N}$.

There are two key factors leading to the uncertainty on the airglow continuum level. On one hand the airglow continuum signal is relatively faint, and on the other it is indiscernible from the grating scattered light, a form of stray light that all dispersion gratings produce. Only a handful of airglow continuum measurements exist in the literature, and just a few of them have considered and quantified the effect of the grating scattered light. An exhaustive listing of all published works is shown in Table B.1 in Article II.

Late 1960s and 1970s were active time in the airglow research. At the time, the technology limited the reliable observation to the VIS wavelengths, since the NIR photo-multipliers suffered from low sensitivity. Some measurements showed a redder spectral energy distribution of the airglow continuum (Sternberg and Ingham, 1972; Gadsden and Marovich, 1973) than others (Noxon, 1978; Sobolev, 1978). Nitrogen monoxide (NO) was believed to be the main source of the airglow continuum, but did not explain the total observed NIR emission, leaving the question on origin of the NIR continuum open to speculation.

A long gap in the measuring the airglow continuum followed. Renewed interest towards the infrared continuum sparked when the SWIR Mercury-Cadmium-Telluride (HgCdTe) detectors started to become more broadly available. Especially, the SWIR continuum measurement of Maihara *et al.* (1993b) raised interest by showing that the SWIR continuum sky could be very dark. Several feasibility studies followed (Herbst, 1994; Content and Angel, 1994; Content, 1996), and OH line suppressor instruments were built (f.e. Maihara *et al.*, 1993a; Piche *et al.*, 1997; Iwamuro *et al.*, 2001; Parry *et al.*, 2004). The airglow line suppressors instruments seemed to have been deployed successfully. However no dedicated airglow continuum study based on their data followed. Only few dedicated continuum observations were published after the inauguration of the European Southern Observatory (ESO) Very Large Telescopes (VLTs; Cuby *et al.*, 2000; Hanuschik, 2003).

It was only later that Ellis and Bland-Hawthorn (2008) raised a revived interest towards the subject by arguing that a significant fraction of the observed continuum could be due to the grating scattered light. A series of papers followed with spectroscopic observations with and without OH suppressors (Ellis *et al.*, 2012; Sullivan and Simcoe, 2012; Trinh *et al.*, 2013; Oliva *et al.*, 2015), as well as dedicated narrow-band photometric observations (Nguyen

et al., 2016). A few narrow-band surveys also reported their background levels (f.e. Venemans *et al.*, 2009; Tilvi *et al.*, 2010; Milvang-Jensen *et al.*, 2013). No firm conclusion was drawn whether the continuum was instrumental artifact or not. Within the margins of error the results agreed with Maihara *et al.* (1993b). On the other hand it was found out that the Maihara *et al.* (1993b) bandpass was affected by faint line emission (Sullivan and Simcoe, 2012; Oliva *et al.*, 2015), and the H band continuum measured by Sullivan and Simcoe (2012) was consistent with their scattered light model.

It has been only very recently that the NIR – SWIR airglow continuum has been attempted to be explained exhaustively. Noll *et al.* (2024) and Noll *et al.* (2025) used a long time series of VLT/X-Shooter spectra to derive climatological models of the airglow line and continuum emission components. Their analysis attributing the large majority of the NIR – SWIR continuum to FeO and HO_2 radiance. The model is site specific to the Cerro Paranal, Chile, and their work does not discuss the potential effect of grating scattered light. It should be noted that their climatological model does not show correlation between the OH line emission and the HO_2 continuum, which were to be expected if their observations were to be due to the grating scattered light.

In this thesis the issue of grating scattered light is addressed by a number of observational and instrumental techniques with the aim to measure the airglow continuum unambiguously in the NIR. In addition to the original papers, the current understanding of the NIR – SWIR airglow radiance is summarized. Atmospheric and extra-atmospheric radiant sources are covered in Chapters 2 and 3 respectively. A short summary of the atmospheric radiative transfer relevant in the context of the articles is included in Chapter 4. The remaining chapters focus on the instrumentation aspects, beginning with stray light performance of the astronomical spectrographs in Chapter 5, followed by optical methods for limiting the effect of stray light are covered in Chapter 6. Some of the methods are novel, and are presented in more detail in the articles constituting to this thesis. A brief view into candidate photon counting detectors for the NIR astronomy has been included in Chapter 7. Finally, the papers published as a part of this work are summarized in Chapter 8 with concluding remarks included in Chapter 9.

2

Airglow

The night sky radiance consist of both atmospheric and extra-atmospheric components. Leaving the extra-atmospheric components to the next chapter, the atmospheric radiance consists of the airglow, various types of auroras, and auroral-like emission, and scattered light from the Moon, stars, artificial lighting, and occasional thunder.

A large number of chemiluminescent processes are known to generate the atmospheric airglow emission. A large fraction of the total radiance is due to various hydroxyl (OH) molecule rotational-vibration line emission. In addition to the OH line emission, other molecular line emission and atomic line emission can be observed on the night sky, and the atmospheric thermal blackbody emission becomes very strong in the long wavelength, at end of the SWIR range.

Especially, the behavior of the line emission is becoming known in a sufficient detail that site specific models can be developed (Noll *et al.*, 2012; Jones *et al.*, 2013; Noll *et al.*, 2017; Noll *et al.*, 2024; Noll *et al.*, 2025). However, the global picture of night-time airglow is still not fully solved, especially in the case of the airglow continuum. It has been only recently that a convincing explanation for the full NIR – SWIR airglow continuum has been given for the site ESO site of Cerro Paranal (Noll *et al.*, 2024; Noll *et al.*, 2025). It should be noted the Cerro Paranal model of Noll *et al.* provides only a local airglow continuum model, while different chemiluminescent processes have been reported to dominate at the polar latitudes in the VIS – NIR range (Gattinger *et al.*, 2010).

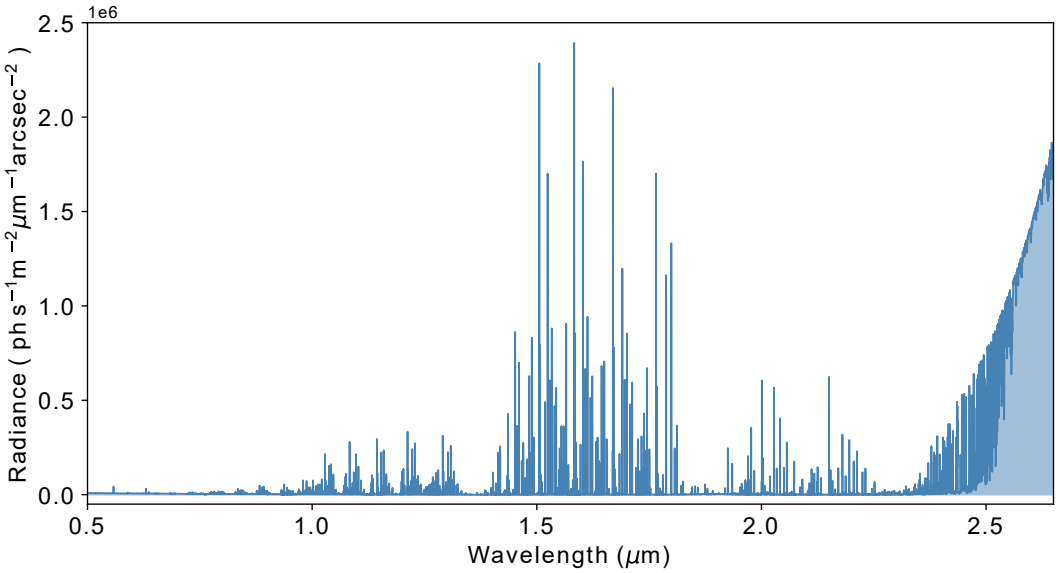

Figure 2.1: Night sky NIR emission is dominated by atmospheric line emission. Around 2.5 μm atmospheric thermal black body emission starts to peak. Figure based on ESO SkyCalc data (Noll *et al.*, 2012; Jones *et al.*, 2013).

The various different airglow phenomena have been featured in European Southern Observatory's (ESO) journal *The Messenger* (Christensen *et al.*, 2016; Horálek *et al.*, 2016a; Horálek *et al.*, 2016b). Figures in the articles are recommended for further visual illustration of the night sky radiance.

2.1 Airglow lines

2.1.1 Hydroxyl (OH)

A large majority of the NIR and SWIR airglow line emission is due to hydroxyl (OH) radical. The OH lines (Noll *et al.*, 2023, and references therein) are extremely bright and their existence has been known for a long time. After the NIR sensitive photographic emulsions became available, bright night sky emission lines at the NIR wavelengths were observed, and soon after attributed to the rotation-vibrational bands of the hydroxyl (OH) molecule (Meinel, 1950a; Meinel, 1950b; Elvey, 1950). A collisional processes between H atoms and O_3 molecules was suggested as an OH production mechanism, reaction R1 (Bates and Nicolet, 1950).

$$\mathrm{H} + \mathrm{O_3} \longrightarrow \mathrm{OH}^*(\nu \leq 9) + \mathrm{O_2} \tag{R1}$$

Despite the reaction R1 being the most dominant, it is not the only reaction producing OH. For example, the reactions

$$\mathrm{HO_2} + \mathrm{O} \longrightarrow \mathrm{OH}^*(\nu \leq 6) + \mathrm{O_2}, \tag{R2}$$

$$\mathrm{HO_2} + \mathrm{H} \longrightarrow \mathrm{OH}^*(\nu \leq 5) + \mathrm{OH} \tag{R3}$$

are known to produce excited OH (f.e. Bates and Nicolet, 1950). Importance of the reaction R2 is still debated in the literature (see, Xu *et al.*, 2012). Extensive OH line lists (f.e. Loo and Groenenboom, 2007; Loo and Groenenboom, 2008; Brooke *et al.*, 2016; Noll *et al.*, 2025) and line maps exist (f.e. Osterbrock *et al.*, 1996; Hanuschik, 2003; Rousselot *et al.*, 2000).

2.1.2 Atomic line emission

In addition to the geocoronal H and He line emission (Khomich *et al.*, 2008), some metal line can be observed in the airglow spectrum. The metals are deposited by micro-meteor ablation, and at least Fe, Mg, Si, and Na, and to lesser extent Ca and K are present (f.e. Plane *et al.*, 2015).

2.2 Airglow continuum

2.2.1 Hydroperoxyl (HO_2)

Very recently, hydroperoxyl has been identified to contribute to the airglow continuum radiance practically stretching the entire NIR – SWIR wavelength range (Noll *et al.*, 2024; Noll *et al.*, 2025). The strong HO_2 band structures are centered at 1.27 μm, 1.51 μm, and possibly 1.62 μm. The HO_2 is responsible majority of the NIR (pseudo)continuum in medium resolution spectra. The main emission mechanism is the reaction R4 (Noll *et al.*, 2025).

$$\mathrm{H} + \mathrm{O_2} + \mathrm{M} \longrightarrow \mathrm{HO_2}^* + \mathrm{M} \tag{R4}$$

Vibrational spectra of Becker *et al.* (1974) show strong emission features at 1.43 μm which cannot be observed from ground because of water vapor absorption (Noll *et al.*, 2025). HO_2 also participates in the OH photo-chemistry (Bates and Nicolet, 1950).

2.2.2 Iron monoxide (FeO)

FeO produces a broad pseudo-continuum spectrum ranging from the VIS wavelengths to NIR (West and Broida, 1975). FeO has identifiable spectral features in the VIS range and it has been detected on the night sky (Unterguggenberger *et al.*, 2017). FeO and NiO show very similar spectral signatures, and are difficult to separate (Evans *et al.*, 2011; Unterguggenberger *et al.*, 2017). The FeO is mainly excited by the reaction R5 (Evans *et al.*, 2010; Noll *et al.*, 2025).

$$\mathrm{FeO} + \mathrm{O_3} \longrightarrow \mathrm{FeO}^* + \mathrm{O_2} \tag{R5}$$

2.2.3 Nickel monoxide (NiO)

NiO produces a pseudo-continuum spectrum similar to FeO. NiO emission has been identified on the night sky from from space-borne limb measurements (Evans *et al.*, 2011). The main production mechanism generating excited NiO is

$$\mathrm{Ni} + \mathrm{O_3} \longrightarrow \mathrm{NiO^*} + \mathrm{O_2}. \tag{R6}$$

2.2.4 Nitrogen monoxide (NO)

The NO reaction R7 was the first proposed mechanisms to be cause the airglow continuum in the VIS and NIR wavelengths (Krassovsky *et al.*, 1951). At mesospheric pressure, the reaction R7 continuum peaks at 0.56 μm (Becker *et al.*, 1972; Kenner and Ogryzlo, 1984; Bates, 1993). There has been extensive discussion if the reaction R7 is sufficient to produce the amount of observed airglow continuum (Noxon, 1978; Wraight, 1986; Bates, 1993).

$$\mathrm{NO} + \mathrm{O} + \mathrm{M} \longrightarrow \mathrm{NO_2} + \mathrm{M} + \mathrm{h}\nu \tag{R7}$$

The reaction R7 is not the only NO reaction producing continuum emission. The reaction R8 produces a continuum spectrum peaking 0.86 μm (Kenner and Ogryzlo, 1984; Khomich *et al.*, 2008).

$$\mathrm{NO} + \mathrm{O_3} \longrightarrow \mathrm{NO_2} + \mathrm{O_2} + \mathrm{h}\nu \tag{R8}$$

Based on the literature, it is not clear to the author, if the NO reactions produce such a negligible amount of emission at middle and low latitudes that they can be ignored. The recent Noll *et al.* (2024) and Noll *et al.* (2025) continuum radiance models for the site of Cerro Paranal, Chile do not require the NO reactions to explain the observed airglow continuum. Noll *et al.* is able to

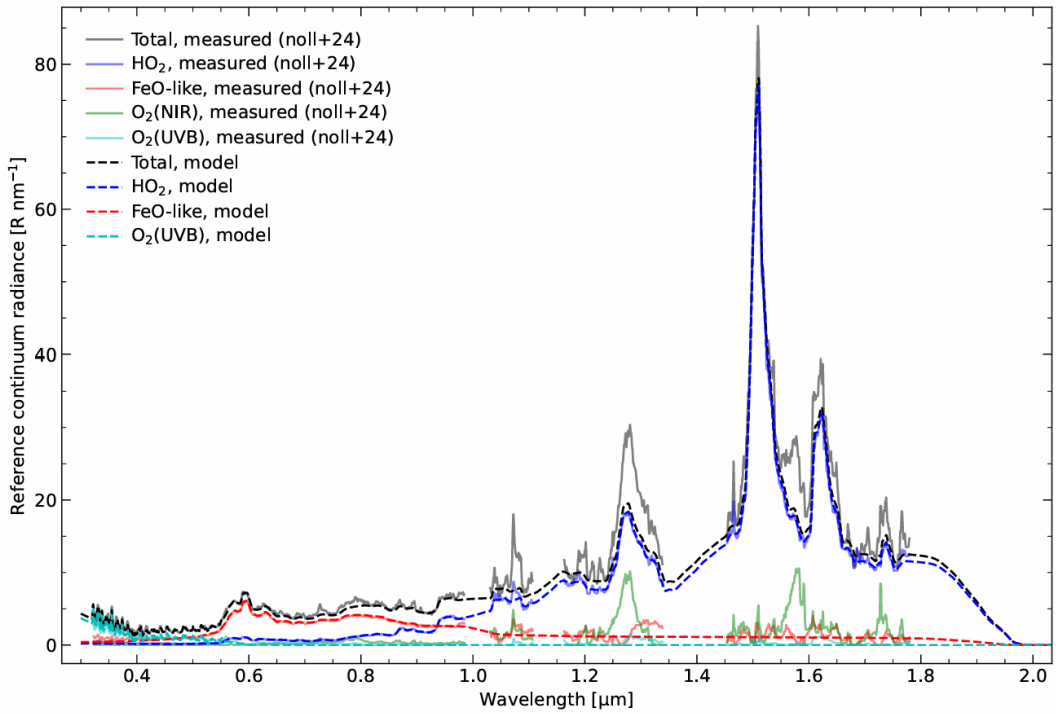

Figure 2.2: The airglow continuum at the observatory site of the Cerro Paranal, Chile has recently explained in terms of only to chemical compounds, namely FeO and HO_2. Figure from Noll *et al.* (2025).

explain the observed continuum in terms of FeO, HO_2, and O_2 only. It should be noted that the Noll *et al.* model is site specific. The NO reactions are shown to have an important role in the airglow at the polar regions (Gattinger *et al.*, 2010) due to auroral NO generation (Kirillov *et al.*, 2023, and references therein). Auroras also generate other reactants such as OH and HO_2 (f.e. Verkhoglyadova *et al.*, 2016).

2.3 Thermal continuum

The atmosphere emits as a blackbody in the SWIR. This is especially evident in the K band which is dominated by the thermal blackbody emission. The blackbody spectral radiance is given by Planck's law,

$$B(\lambda, T) = \frac{2hc^2}{\lambda^5} \frac{1}{e^{\frac{hc}{\lambda kT}} - 1} \tag{2.0}$$

where h, k, and c are Planck constant, Boltzmann constant, and speed of light. The thermal continuum becomes dominant at wavelengths $>2\,\mu\mathrm{m}$ at all current major observatory sites. Placing an observatory on Antarctica reduces the atmospheric thermal emission significantly (Ashley *et al.*, 1996; Nguyen *et al.*, 1996).

2.4 Auroras

Auroras (Knudsen *et al.*, 2021, and the series) are not covered in detail in this thesis. Nevertheless, their presence, even at very low geographical latitudes, should not be ignored. Auroras were observed at the Observatorio del Roque de los Muchachos, La Palma, located on the 28°N latitude on 10 May 2025 (Fig. 2.3), and several historical reports on aurora sightings at the Canary Islands exist (Vázquez and Vaquero, 2010). Low-latitude auroras have been also observed elsewhere around the globe (f.e. APOD 15 Sep 2000[1], Hayakawa *et al.*, 2017; Oliveira *et al.*, 2020).

Auroras are caused by the charged solar particles spiraling into the Earth's magnetic field, which are continuously transported by the solar wind. The area in the around the magnetic poles where the majority of the particles precipitate are referred as the auroral ovals. During periods of low solar activity the auroral ovals reside at 70 – 75° magnetic latitude. During stronger solar activity and geomagnetic storms, the auroral ovals can be pushed to magnetic latitudes <55°.

Several different sub-categories of auroras exist depending on their visual appearance, and spectral features (Vallance Jones and Gattinger, 1971; Knudsen *et al.*, 2021). Some of the auroral subtypes reside at subauroral regions, for example the Stable Auroral Red arcs, and isolated proton auroras (Martinis *et al.*, 2019; Gallardo-Lacourt *et al.*, 2021). Also distinct auroral activity exist over the South Atlantic Anomaly (He *et al.*, 2020).

[1] Astronomy Picture of the Day, 15 Sep 2000

Figure 2.3: Auroras viewed from the Nordic Optical Telescope at 29° N latitude on May 10th 2024. During the Solar storm, the northern auroral oval reached the level of Copenhagen at 55° N latitude. Image taken by Benjamin Nobre Hauptmann.

2.5 Strong Thermal Emission Velocity Enhancement

In addition to the auroras, another bright atmospheric optical phenomenon called Strong Thermal Emission Velocity Enhancement (STEVE) exists. STEVEs have come under scientific scurtiny only recently (Gallardo-Lacourt *et al.*, 2018). In contrast to the auroras, the STEVEs are not caused by particle precipitation, and they form narrow thousands of kilometers long structures (Gallardo-Lacourt *et al.*, 2018). While the STEVE spectrum contains prominent auroral 5577 and 6300 Å oxygen lines, a significant fraction of the total intensity is emitted as a continuum (Gillies *et al.*, 2019). Sometimes STEVEs are seen in conjunction with picket fence aurora (Gillies *et al.*, 2019), and they have been observed to develop from Stable Auroral Red arcs (Martinis *et al.*, 2022).

Figure 2.4: STEVE appears as a narrow up to thousands of kilometers long optical emission. Image credit: Wikimedia Commons/Elfiehall.

2.6 Scattered light

All observations to establish the dark sky continuum brightness in the articles of this thesis have been made either during new Moon, or when the Moon has been below 20° the horizon, and as such scattered moonlight has not needed correction in the data analysis. It should be noted that scattered moonlight is the brightest atmospheric continuum component even in the NIR. Scattered Moon light are available in the literature (f.e. Krisciunas and Schaefer, 1991; Jones *et al.*, 2013).

The scattered star light intensity varies over the sky as the stellar density varies, leading towards a stronger contribution when pointing towards the galactic equator than towards the galactic poles. The articles in this thesis, have ignored the scattered star light contribution. Based on the estimates of ESO SkyCalc (Noll *et al.*, 2012; Jones *et al.*, 2013), the scattered light illumination for the observed pointings is less than $5\,\mathrm{ph\,s^{-1}m^{-2}}\mu\,\mathrm{m^{-1}arcsec^{-2}}$, which is insignificant in comparison to the measured continuum values.

In addition to the natural illumination, the night sky is lit by artificial lights, to a point that it begins to be difficult to find a dark site globally (Falchi *et al.*, 2016; Falchi *et al.*, 2023). All observation part of this work have been carried out at the Observatorio del Roque de los Muchachos, La Palma, Canary Islands, Spain. The island of La Palma has artificial illumination restrictions in place, and significant fraction of the street lights still use high pressure sodium lamps which mostly emit lines at 5890 and 5896 Å (Benn and Ellison, 1998). All observations were made towards the North with little artificial lighting on the line of sight. The backscattering from the light of Santa Cruz de La Palma, Los Llanos, and El Paso could be modeled (Garstang, 1986; Garstang, 1989; Cinzano and Elvidge, 2004), but was not done in this thesis.

2.7 Airglow temporal variability

Variability of the infrared night sky radiance is well known from the phenomenon for the ground-based astronomers: ground-based IR telescopes either chop, or dither, to sample and subtract out the varying atmospheric background emission. The Mesophere-Lower Thermosphere (MLT) region

where the airglow emission is originating from hosts suitable conditions for occurrence of different types of wave and other density phenomena, which can be observed as intensity changes of the airglow with several different timescales (f.e. Smith, 2012).

At the timescale of minutes, the variability is caused by what is known as *gravity* or *buoyancy* waves. The buoyancy waves can cause the airglow intensity to vary ∼15% on timescales from a few up to tens of minutes (f.e. Moreels *et al.*, 2008). The buoyancy waves as a phenomenon are affected by the solar activity which affects their probability of occurrence and power spectrum (f.e. Laskar *et al.*, 2015). Another cause of short timescale airglow intensity changes are the atmospheric bore events (f.e. Knupp, 2006; Haghi and Durran, 2021). The bore events can drive soliton waves which can be observed as a strong step function like brightening of night sky emission (f.e. Smith *et al.*, 2006; Walterscheid *et al.*, 2012).

At the timescale of hours, the airglow intensity is affected by the atmospheric tides. In contrast to the ocean tides which are driven by the gravitational pull of the Moon and Sun, the atmospheric tides are mostly driven by the solar irradiance and follow 12 hour cycle (f.e. Smith, 2012). The atmospheric tides results to stronger airglow in the beginning and end of the night.

In addition, to the variability taking place during a single night, the airglow intensity is also affected by planetary waves, Earth's orbital position and the solar activity at timescales from days, to months, and even years. Semi-annual oscillation has been observed in the astronomical broadband data (Patat, 2008), and in the airglow line emission (Grygalashvyly *et al.*, 2021). The periodicity can be seen in several of the airglow components (Noll *et al.*, 2025). The longer term airglow solar cycle dependence has been reported at several major astronomical sites (f.e. Leinert *et al.*, 1995; Krisciunas, 1997; Patat, 2008; Roth *et al.*, 2016). O_2 and OH line emission respond to the solar activity (f.e. Pertsev and Perminov, 2008; Noll *et al.*, 2017).

2.8 Airglow geographical dependence

The geographical dependence of the airglow emission is not studied in this thesis, but it should be noted that latitudinal dependence should be expected from the varying solar irradiance conditions between the equator and the poles, dynamics of the atmosphere, and the Earth's magnetic field guiding the solar particles to the magnetic poles. Gattinger *et al.* (2010) shows a clear difference in the spectral energy distribution of the airglow continuum at the middle and polar latitudes in their VIS spectra. The airglow latitudinal dependency has been covered f.e. in Forsyth and Wraight (1987).

3 Extra-atmospheric radiance

Even if all atmospheric radiance is removed, the night sky will not be completely dark. Both ground-based and space-borne observations are affected by the Zodiacal Light (ZL) and the Milky Way, which are the two brightest extra-atmospheric sources. The ZL is even brighter than the airglow towards the ecliptic plane (Fig. 3.1). Both ZL and Milky Way are continuum sources posing a problem for the ground-based night sky airglow continuum observation: the ZL or Milky Way contribution must be subtracted from the measurement.

3.1 Zodiacal light

The Zodiacal Light (ZL) is scattered Sun light it is responsible for the majority of the extra-atmospheric surface brightness when pointing away from the galactic plane, and it can be even seen with unaided human eye under dark sky conditions (Fig. 3.1). The ZL is caused by scattering of the inter-planetary dust particles, and as such follows the solar blackbody spectral energy distribution (Leinert *et al.*, 1998).

The ZL is brighter in the ecliptic plane, especially at the low solar elongation angles. Additionally, there is a brighter back-scattering feature known as the *gegenschein* towards solar elongation 180° (see figures in, Horálek *et al.*, 2016b). Towards the direction of ecliptic poles, which is the darkest background available, the ZL has a surface brightness of $\sim$23 $\mathrm{mag_{AB}\,arcsec^{-2}}$, or 50 $\mathrm{ph\,s^{-1}m^{-2}}\mu\,\mathrm{m^{-1}arcsec^{-2}}$. This is a level which is slightly darker than the airglow continuum measured in Article II. The amount of ZL radiance for a

Figure 3.1: Zodiacal light seen from the Nordic Optical Telescope towards West at dusk.

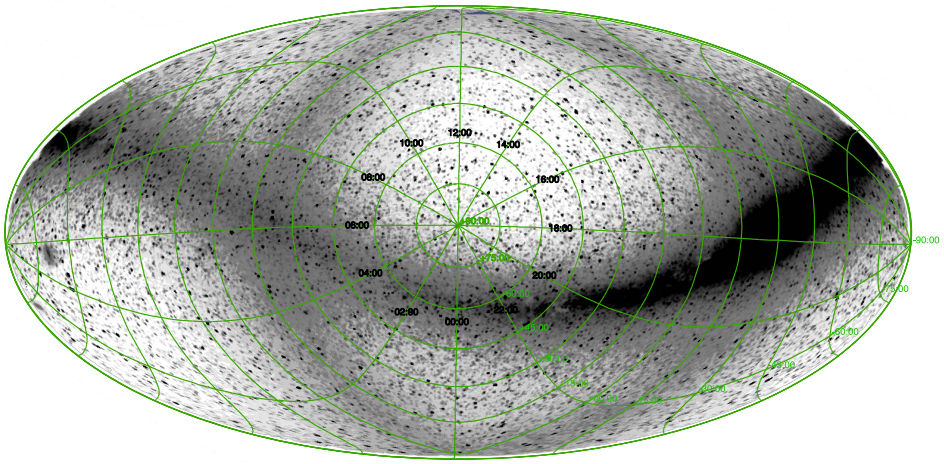

Figure 3.2: COBE/DIRBE Band-1 (1.25 μm) map of diffuse radiance above atmosphere pointing towards the ecliptic north pole. Milky Way crosses the map horizontally and the zodiacal light forms a ring around the ecliptic.

given astronomical position varies around the year due to Earth's movement around the sun, and varying viewing angle due to inclination of the Earth's orbital plane respective to the plane of zodiacal dust.

The inter-planetary dust (IPD) (f.e. Gustafson, 1994) cloud geometry responsible for the ZL scattering can be divided into three main components: *i)* Smooth cloud, *ii)* Dust bands, and *iii)* circum-solar ring with an Earth trailing *'blob'* (Kelsall *et al.*, 1998). The smooth cloud contributes majority of the ZL surface brightness (>90 %). There are three main dust bands (Low *et al.*, 1984; Jorgensen *et al.*, 2021) which are due to collisional debris. Their composition, origin, and dynamics is still an active field of study (f.e. Espy *et al.*, 2009; Jorgensen *et al.*, 2021).

To date, the most complete ZL models are based on the COsmic Background Explorer (COBE) Diffuse Infrared Background Experiment(DIRBE) data (Kelsall *et al.*, 1998; Wright, 1998; Gorjian *et al.*, 2000), although the look-up tables of Levasseur-Regourd and Dumont (1980) are still in use for the VIS wavelengths (f.e. ESO SkyCalc Noll *et al.*, 2012; Jones *et al.*, 2013). There are two different widely used models based on DIRBE data Kelsall *et al.* (1998) and Wright (1998) and Gorjian *et al.* (2000). The Kelsall *et al.* (1998) model is a physical model, while, Wright (1998) is more parametric. The Wright (1998) model assumes the ZL to be isotropic and constant in time at 25 μm towards the ecliptic poles, a restriction that Kelsall *et al.* (1998) does not impose. Consequently, Wright (1998) attributes a larger fraction of the total

surface brightness to ZL than Kelsall *et al.* (1998) on wavelengths shorter than 25 μm. There is an on going effort to build a better VIS – NIR ZL model based on Hubble Space Telescope (HST) data (SKYSURF, Windhorst *et al.*, 2022; Carleton *et al.*, 2022; O'Brien *et al.*, 2025).

Both Kelsall *et al.* (1998) and Wright (1998) models extrapolate the VIS – NIR the surface brightness at wavelengths $<$1.25 μm based on the assumption that the ZL follows a slightly reddened Solar spectrum (f.e. Leinert *et al.*, 1998). The spectral energy distribution of ZL is not well known in the NIR range due to the fact that the particle size and composition is still not well known. It has been reported on occasions that the DIRBE ZL models underestimate the ZL at wavelengths shorter than 3.5 μm (f.e. Tsumura *et al.*, 2013). We have used the Kelsall *et al.* (1998) model based InfraRed Science Archive (IRSA), Infrared Processing & Analysis Center (IPAC) *Euclid* background model calculator[1] for calculating the ZL contribution for a given right ascension, declination, and time in Articles II, III, and IV.

In the coming years, *Euclid* (Euclid Collaboration *et al.*, 2025) and Spectro-Photometer for the History of the universe, Epoch of Re-ionization, and Ices Explorer (SPHEREx, Bock *et al.*, 2025) will provide new data on the diffuse NIR – SWIR radiance extending and complementing the measurements of IRAS and COBE/DIRBE.

3.2 Diffuse Galactic Light

The NIR – SWIR emission of Milky Way is dominated by stellar light (Arendt *et al.*, 1998, and references therein). Consequently, the majority of the galactic illumination for large telescopes is spatially resolved point sources, and does not affect diffuse background measurement. The Diffuse Galactic Light (DGL) is due to scattering of stellar light in the Inter-Stellar Medium (ISM). Milky Way geometry can be divided into the bulge, disk, and interstellar cirrus (Leinert *et al.*, 1998; Arendt *et al.*, 1998). The bulge consists of older stars than the spiral arms, and the bulge SED is generally redder than the spiral arms. The interstellar cirrus has complex geometry with filament structures extending over large area on sky (f.e. Gillmon and Shull, 2006) which tend

[1] `https://irsa.ipac.caltech.edu/applications/BackgroundModel/`

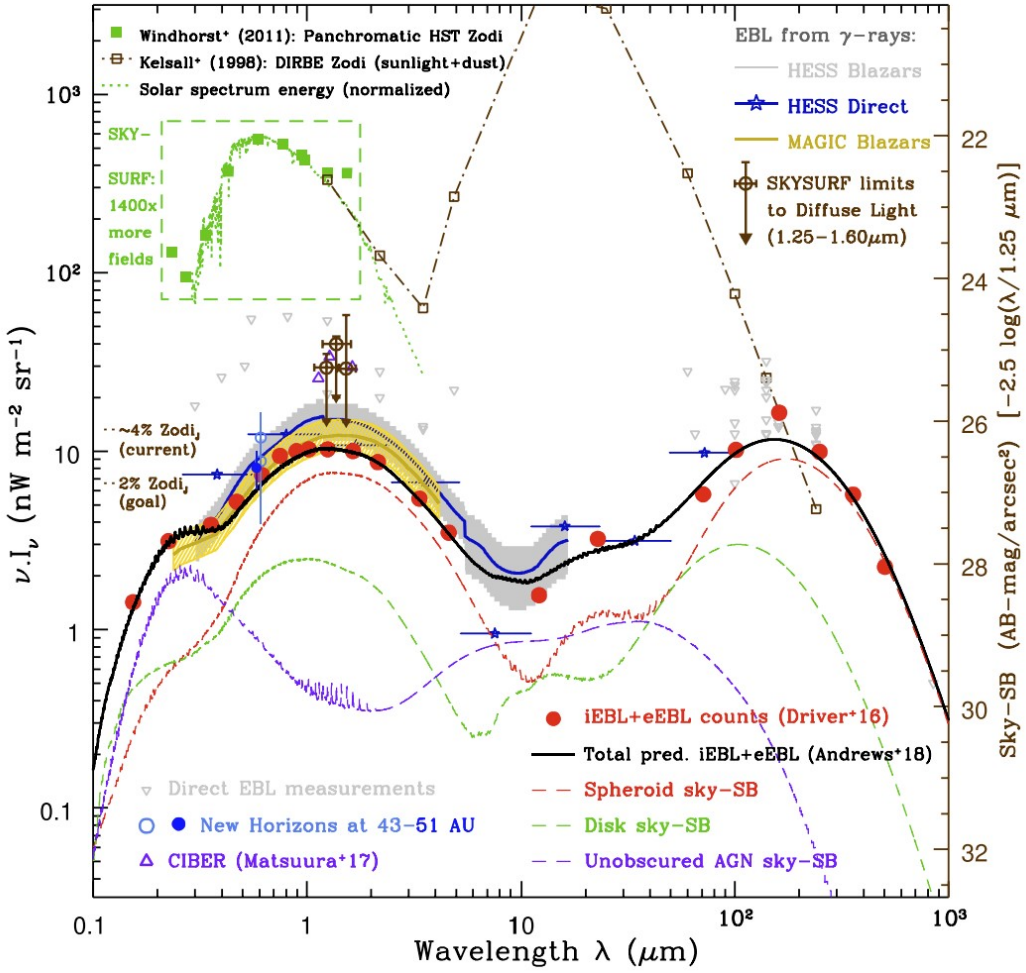

Figure 3.3: The extra-atmospheric diffuse radiance divided into its components. The zodiacal light (green squares Windhorst *et al.*, 2011), and thermal emission from the inter-planetary dust (brown squares Kelsall *et al.*, 1998) are the brightest background components in the inner Solar System, much brighter than the extra-galactic background level (black continuous line). Figure from Carleton *et al.* (2022).

to have redder color than the disk (Leinert *et al.*, 1998). For the purposes of the articles in this thesis, it has been sufficient to avoid observing towards the galactic plane with galactic latitudes $\beta_{\rm gal} > 20°$.

3.3 Cosmic Infrared Background

The Cosmic Infrared Background (CIB) with an upper limit surface brightness of $>$26 mag arcsec^{-2}, or a few ph s^{-1}m$^{-2}\mu$ m^{-1}arcsec^{-2} (f.e. Dwek and Arendt, 1998; Sano *et al.*, 2020) is significantly fainter than the airglow continuum or the ZL, and has been ignored as a contributing factor in the measurements.

4

Atmospheric radiative transfer

Airglow emission is electromagnetic radiation and as such it is fully described by the typical equations of radiative transfer. Measurement of an extended radiant surface spanning a large solid angle differs from that of a point source. The measurement of an extended source is affected by the scattering to the line-of-sight from the source itself. This must be taken into account if a non-zenithal observations are to be compared between different altitude pointings. The scattering integrals for different geometries are not solved in this thesis, and solutions provided in the literature are used instead. The chapter is intended to provide a summary of factors involved in the measurement surface brightness of large solid angle extended radiant sources.

Total apparent observed intensity I_{tot}, consist of the source itself I_0, background emission I_{bkg}, absorption on the lines of sight I_{abs}, scattering away from the line-of-sight $I_{\mathrm{sct,\,out}}$, and scattering to the line-of-sight $I_{\mathrm{sct,\,in}}$.

$$I_{tot} = I_0 + I_{\mathrm{bkg}} - I_{\mathrm{abs}} - I_{\mathrm{sct,\,out}} + I_{\mathrm{sct,\,in}} \tag{4.1}$$

Each term is briefly covered in this chapter. The radiant sources have been covered in more detail in the two preceding chapters.

4.1 Radiance

Understanding the atmospheric background radiance is a key for optimizing the operation of the ground-based observatories, especially for the upcoming Extremely Large Telescopes (ELTs). In astronomy, all different background sources are typically summed together into a single *background* since the photons can be assumed to be Poisson distributed. However, this is less convenient when attempting to separate the different background sources.

In order to measure the airglow continuum, there has to be an estimate on the extra-atmospheric background level. Also, the altitude and thickness of the emitting airglow layer needs to be known to derive zenith equivalent values that can be compared to each other, and other studies. Majority of the atmospheric radiance is emitted from a relatively thin layer at an altitude of ~90 km (Baker and Stair, 1988; Savigny *et al.*, 2012). Due to the airglow being emitted from a layer of finite thickness, the airglow intensity $I_{\mathrm{ag}}(z)$ scales less steeply with zenith angle z than that of point source. The airglow scaling can be described with van Rhijn function (Eq. 4.2). The airglow intensity $I_{\mathrm{ag}}(z)$ scales as a function of zenith angle z to

$$\frac{I_{\mathrm{ag}}(z)}{I_{\mathrm{ag}}(0)} = \left[1 - \left(\frac{R\sin(z)}{R+h}\right)^2\right]^{-1/2}, \tag{4.2}$$

where the $I_{ag}(0)$ is the airglow intensity at zenith, R is the radius of Earth, and h is the height of the emitting layer above Earth's surface (van Rhijn, 1921). Eq. 4.2 neglected the thickness of the emitting layer, which is valid for low zenith angles. If the observer is either close to the emitting layer (satellites), or points very low in the horizon, as we do in Articles II and IV, it is better to use an earlier stage of van Rhijn (1921) derivation (their Eq. 19)

$$\begin{aligned}\frac{I_{\mathrm{ag}}(z)}{I_{\mathrm{ag}}(0)} =& \sqrt{R^2\cos^2(z) + 2Rh_2 + h_2^2} \\ &- \sqrt{R^2 cos^2(z) + 2Rh_1 + h_1^2}.\end{aligned} \tag{4.3}$$

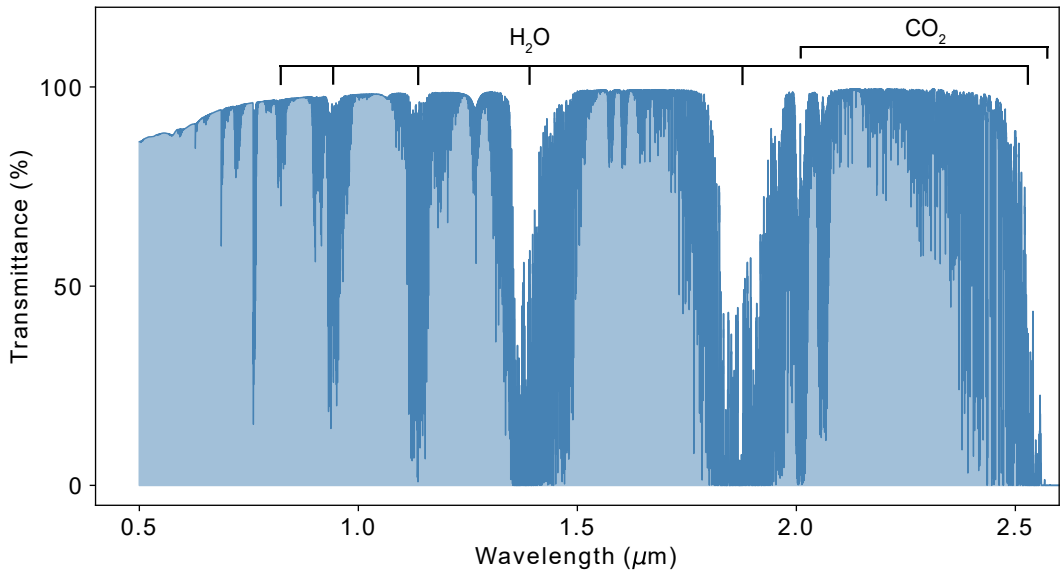

Figure 4.1: The zenithal atmospheric NIR – SWIR transmittance for altitude of 2400 m including both absorption and scattering effects as a function of wavelength. Figure based on ESO SkyCalc data (Noll *et al.*, 2012; Jones *et al.*, 2013).

The form of Eq. 4.3 has been used in Article II when observing at a low altitude in the atmosphere.

4.2 Absorption

Water vapor H_2O is the main absorber in the entire VIS – SWIR wavelength range (Fig. 4.1). Water vapor has several absorption bands in the range 0.7 – 3 μm. Additionally, CO_2, CH_4, and O_2 absorb in the NIR – SWIR. CO_2 absorption becomes more significant at longer wavelengths. The atmospheric water vapor content and consequently the absorption varies significantly from night to night. In this thesis, spectral regions affected by the H_2O are avoided to the extent possible, and the only bandpasses free of H_2O absorption have been selected for analysis.

4.3 Scattering

Rayleigh scattering describes scattering by particles smaller than the scattered wavelength and it is the most significant scattering component in the blue end of spectrum.

$$I = I_0 \frac{8\pi^4 N \alpha^2}{\lambda^4 R^2} \left(1 + \cos^2 \theta\right) \tag{4.4}$$

Optical depth due to Rayleigh scattering is pressure dependent, even though for a fixed site the difference is negligible. Liou (2002) gives

$$\tau_{0,\,R}(\lambda, h, p) = \frac{p}{p_s} \left(a + bh\right) \lambda^{-(c + d\lambda + e/\lambda)}, \tag{4.5}$$

for optical depth due to Rayleigh scattering, where, h is altitude in kilometers, p is pressure, $p_S = 1013.25$ hPa, and the constants are $a = 0.00864$, $b = 6.5 \times 10^{-6}$, $c = 3.916$, $d = 0.074$, and $e = 5 \times 10^{-2}$. For a given altitude, the pressure variation can be neglected, and observatory specific parametrization may be used. King (1985) has parametrized extinction for Observatorio Roque de los Muchachos (ORM), on La Palma, Canary Islands, where all observations in this work have been executed.

4.4 Extinction

Extinction is the combination of absorption and scattering processes. Atmospheric transmission t depends on the optical depth τ of the atmosphere which can be presented as

$$t(\lambda) = e^{-\tau_0(\lambda) X}. \tag{4.6}$$

Extinction airmass X for a point source outside the atmosphere can be calculated from the typical $X = \sec(z)$ plane parallel atmosphere assumption in which z is the zenith angle. The plane parallel atmosphere assumption does not hold well in the low atmosphere, and we calculate the point source airmass based on Kasten (1965) approximation Eq. 4.7, with updated coefficients from Kasten and Young (1989), giving the airmass X as a function of altitude angle θ as

$$X(\theta) = \left(\sin(\theta) + a(\theta + b)^{-c}\right)^{-1}, \tag{4.7}$$

where the coefficients are $a = 0.50572$, $b = 6.07995°$, and $c = 1.6364$.

Due to the line-of-sight scattering the point source airmass scaling cannot be used for the large solid angle zodiacal light and the airglow radiance. Large angular area radiant sources have lower effective optical depth due to line-of-sight scattering (Wolstencroft and Breda, 1967; Garstang, 1986; Garstang, 1989). Due to the differing geometry of the ZL (Krisciunas and Schaefer, 1991) and airglow (Noll *et al.*, 2012), we take

$$X_{\rm zl}(z) = \left[1 - 0.96 \sin^2(z)\right]^{-1/2} \tag{4.8}$$

$$X_{\rm ag}(z) = \left[1 - 0.972 \sin^2(z)\right]^{-1/2} \tag{4.9}$$

Optical densities of the different scattering components scale differently as a function of airmass X. According to Noll *et al.* (2012), the reduction can be presented as an effective optical depth $\tau_{\rm eff} = f_{\rm ext}\tau_0$, where $f_{\rm ext}$ is the reduction factor, and τ_0 zenithal optical depth. According to Noll *et al.* (2012), the reduction factors $f_{\rm ext}$ for ZL Rayleigh and Mie scattering are,

$$f_{\rm ext,\,zl,\,R} = 1.407 \log I_0 - 2.692 \tag{4.10}$$

$$f_{\rm ext,\,zl,\,M} = 1.309 \log I_0 - 2.598 \tag{4.11}$$

where I_0 is the ZL surface brightness outside of the atmosphere in the units of $10^{-8} \times \mathrm{W\,m^{-2}\,\mu m^{-1}\,sr^{-1}}$, and requiring that $\log I_0 \leq 2.44$, which is a criterion filled in this work. Similarly, we take the extinction reduction factors for airglow emission Rayleigh and Mie components from Noll *et al.* (2012) as,

$$f_{\mathrm{ext,\,ag,\,R}} = 1.669 \log X_{\mathrm{ag}} - 0.146 \tag{4.12}$$

$$f_{\mathrm{ext,\,ag,\,M}} = 1.732 \log X_{\mathrm{ag}} - 0.318 \tag{4.13}$$

where X_{ag} is given in Eq. 4.9.

5 Spectrograph stray light

Stray light is defined as any light detected in a non-intended location. Stray light, and control over it, is a key aspect for the thesis since the airglow continuum measurement is specifically susceptible to it. The grating scattered light has been even suggested to be the reason for the observed NIR – SWIR airglow continuum (Ellis and Bland-Hawthorn, 2008), since it appears as a false continuum like signal. The measured airglow continuum has been reported to be consistent with the grating scattered light at spectral regions most densely populated by the atmospheric OH lines (Sullivan and Simcoe, 2012). The impact of the grating scattered light is rarely analyzed or discussed in the articles studying the airglow continuum. This chapter presents stray light sources in a spectrograph, focusing on the grating scattered light.

5.1 Diffraction grating scattered light

The grating scattered light (Dravins, 1978; Woods *et al.*, 1994; Koch *et al.*, 2021) contributes a large fraction of the total scattered light budget of a spectrograph. A typical astronomical medium to high-resolution ($R > 5000$) spectrograph is designed to be a cross-dispersing echelle spectrograph. The echelle spectrographs operate in high orders, requiring large distance between the grating grooves and a steep grating facet angle. The echelle gratings are almost exclusively reflection gratings. Broadly, the grating scattered light can be divided into two components, *i.)* groove spacing related errors known as *ghosts* and *grating grass*, and *ii.)* diffuse surface micro-roughness related stray light.

5.1.1 Grating Distribution Function

An ideal grating can be considered as a N-slit diffraction experiment. The response function to a monochromatic light source is the called Grating Distribution Function (GDF). For an ideal grating, the normalized intensity profile with N grooves is

$$\frac{I}{I_0} = \left(\frac{\sin\beta}{\beta}\right)^2 \left(\frac{\sin N\gamma}{N\sin\gamma}\right)^2, \tag{5.1}$$

in which $\beta = \frac{kb}{2}\sin\theta$, and $\gamma = \frac{kh}{2}\sin\theta$ where k is the wavenumber, b is the groove width, h is the groove spacing (Woods *et al.*, 1994; Ellis and Bland-Hawthorn, 2008).

No grating is ideal, and in practice variability in the groove spacing and groove width leads to multiple dislocated monochromatic images of the entrance aperture, the grating *ghosts*. The highest achievable spectral resolution is limited by the number of consecutive equal grating grooves (Woods *et al.*, 1994; Ellis and Bland-Hawthorn, 2008). The GDF can be measured, but in case of astronomical spectrographs, it is rarely reported leading the end user to estimate the grating performance from the line spread function instead.

5.1.2 Grating ghosts

Gratings ghosts are dislocated copies of a parent line which originate from groove spacing errors. The ghosts can be divided into ones originating from periodic, and from random ruling errors (Loewen and Popov, 1997; Palmer, 2020). The periodic errors are classically divided further into what is known as Rowland ghosts and Lyman ghosts.

The periodic errors are typically associated with the diamond ruling machine used for ruling the master grating. The Rowland ghosts originate from long period ruling errors resulting into copies of the parent line in the proximity of the parent line, while the Lyman ghosts appear further away from the parent

line and are caused by more localized ruling errors (Loewen and Popov, 1997; Palmer, 2020). The Rowland ghosts can be seen close to the Helium-Neon laser line in the Fig. 6.1.

The *satellites*, or the *grating grass* are a result of localized random groove spacing errors. The grating grass is the responsible for the grating scattered light that can be misidentified as the airglow continuum. The grating grass is impossible to correct for in the data processing due to the multitude of low intensity copies of the parent line. The grating grass can be seen forming an X-like pattern in the PSF of the Article I spectrograph (Fig. 6.1).

5.1.3 Line spread function

When a grating is installed in a spectrograph, the final image on the detector is drawn through a train of geometrical optics, and as a result the GDF gets convolved with the instrument's Point Spread Function (PSF). The resulting convolution is known as the Line Spread Function (LSF).

The spectrograph LSF can be approximated as a combination of Gaussian and Lorentzian functions, together with a constant background in the proximity of the parent line (Woods *et al.*, 1994; Ellis and Bland-Hawthorn, 2008). The contrast between the LSF peak and the constant background depends on the quality of the grating. Thus, there is a fundamental limit on how faint continuum can be observed in presence of bright emission lines. In the SWIR astronomy, the integrated line wings of plethora of OH lines can contribute to a significant instrumentally introduced continuum.

Ideally, the LSF is measured with a bright monochromatic light source such as single mode laser which has been done in Article I using a Helium-Neon laser. Achieving the same can be more difficult at an observatory site, and in case of Article II the LSF has been approximated based on the spectral lines of an arc lamp instead. Using arc lamp lines provides a worst case estimate for the LSF fit since the spectral lines are not necessarily singlets.

5.2 Thermal stray light

Since the current state-of-the-art SWIR HgCdTe detectors have a sensitivity cutoff at 2.5 μm, they are sensitive to the thermal blackbody radiance of the ambient temperature air, as well as the telescope and instrument structures. The thermal leakage may happen through the optical train by having insufficient blocking density outside of the desired bandpass, or by leaks through the radiation shields and other thermal insulation. Examples of such cases of unwanted thermal leaks have been reported in the literature. Two such instruments relevant for this thesis include X-shooter (Vernet *et al.*, 2011) and PRAXIS (Ellis *et al.*, 2020). A possible remedy for blocking thermal stray light is studied in Article III.

5.3 Other sources of stray light

While not as relevant as the grating scattered light, other sources exist in the astronomical spectrographs. Any incoming off-axis light results into unwanted illumination. Typically, the off-axis light is already blocked by the telescope baffles. If the telescope baffles do not take care of the off-axis illumination, there is a risk that thermal radiance, for example, from the dome floor could reach the detector. Microscopic surface roughness and particles deposited on the optical surfaces cause scatter light. In addition to surface scattering, optical components such as glass lenses may exhibit volumetric defects such as bubbles, inclusions, and striae (Gerhard, 2017), leading to unwanted refraction inside the optical element.

6 Spectrograph scattered light reduction

As discussed in the previous chapter, the spectrograph performance is mainly limited by the grating scattered light. A few technical and observational strategy related choices are presented below. In addition to what is described here, the spectrograph stray light performance can be ensured by use of high performance anti-reflection coatings, correct baffle and stop placement, and in case of infrared observation telescope design. In case of background limited point source observation, the effect of the background can be further limited by concentrating the emitted energy from a point source to a smaller angular area, i.e. by using adaptive optics in case of astronomical telescopes. Additionally, use of high surface and material quality components reduces the total amount of stray light.

6.1 Interference or holographic gratings

While the spectral purity of ruled reflection gratings has gained from the improved interferometric control of the ruling machines resulting in less ghosts and grating grass. The ghost performance can be further improved by using interferometric manufacturing methods. Manufacturing of holographic gratings makes use of two or more interfering monochromatic light beams to produce practically ideally spaced groove pattern without periodic errors (Loewen and Popov, 1997). This results into ghost free gratings (see f.e. LSF profiles of, Dravins, 1978). The downside of holographic gratings is that the groove profile becomes sinusoidal, making them difficult to manufacture with blazed grooves

(Loewen and Popov, 1997). Thus, they are typically manufactured for use in low spectral orders, and are not practical for echelle spectrographs. However, ion beam etching can be used to adjust the lithographic groove profiles to shape the grooves (Loewen and Popov, 1997). Recently, the holographic writing process has been applied to silicon etched gratings, in which the silicon's crystal orientation specific etching speed is utilized to produce nearly ideal grating facets (f.e. Sadlowski *et al.*, 2020). The silicon etched gratings can be blazed to be used in high orders making them an interesting type of grating for future astronomical spectrographs.

6.2 Spectrograph design

White pupil echelle design (Baranne, 1972) brings the non-cross dispersed spectrum into a focus which allows placing an aperture in this secondary limiting stray light before cross dispersion. In terms of stray light performance, the most of the white pupil design can be made in a multi-pass configuration, where the light will pass the grating more than once. This can be implemented as a double-pass scanning monochromators (f.e. Bass *et al.*, 1995, Chpt. 5.5) greatly reducing the scattered light. An example of a double dispersing scanning spectrograph for astronomical use is Coude Echelle Spectrograph (CES) at ESO-3.6 (Enard, 1982), which has been designed for high resolution, high spectral purity spectroscopy of spectro-photometric standard stars.

A variation of the white-pupil echelle design is presented in Article I. Instead of implementing the spectrograph as a double-pass as a monochromator, the light is dispersed twice by a single grating. The two individual dispersion are directed 90° respective to each other. The spectrum after the two dispersions is a vector sum of the two dispersions and emerges to 45° respective to the individual dispersions (6.1). We call this design *'double-X-dispersed'* spectrograph and it is practically grating scattered light free since it direct the grating scattered light of the two individual dispersion away from the dispersion axis. Performance of this design is limited by the surface quality and cleanliness of the optical components. The design concept is from Andersen and Andersen (1992), and the spectrograph has been designed as a MSc project of the author (Viuho, 2018).

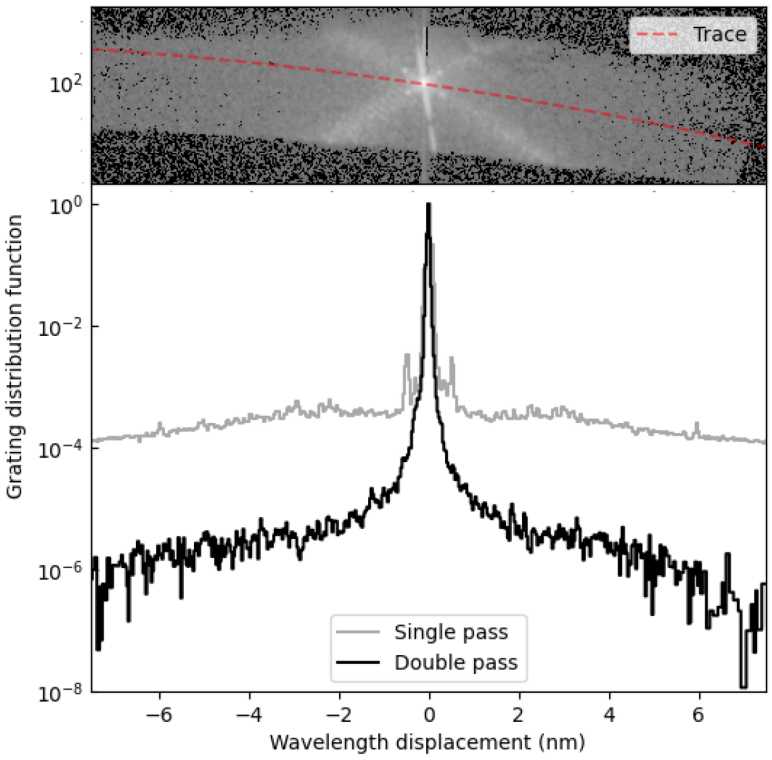

Figure 6.1: SKITLES spectrograph's PSF in double pass (top), and LSF in both the single pass (gray) and the double pass (black) at HeNe-laser wavelength of 632.8 nm. Rowland ghosts are visible in the single pass with a ± 0.5 nm displacement from the HeNe line. In double pass, the Rowland ghosts are placed off the dispersion axis, see four copies around the parent line on the top panel. The grating grass is responsible for the X-shaped PSF of the spectrograph, and hence the name *'double-X-dispersed'* design. Figure from Article I.

6.3 Line suppression and avoidance

One way to prevent the detector seeing bright instrumental scattering wings is to prevent the emission lines reaching the grating altogether. These strategies can be called line suppression and line avoidance. In line suppression, only the light from the spectral lines blocked only. At least three distinct types of line suppressors can be found from the literature: line masks (Maihara *et al.*, 1993a, f.e.), Fiber Bragg Gratings (FBG) (f.e. Ellis *et al.*, 2012), and photonic ring resonators (Ellis *et al.*, 2017). Line masks and FBGs will be described below briefly. An alternate strategy of line avoidance consists of selecting a bandpasses with either little or no OH line emission to improve on the SNR of the measurement. Line avoidance methods have been utilized in Articles II and III.

Line masks

The earliest invention to suppress OH lines was to use a line mask in combination with pre-dispersion optics. Practically, the optical system is a tandem of two spectrographs (f.e. Maihara *et al.*, 1993a). A reflective line mask is placed in the focus of the pre-disperser spectrograph the beam is sent back to the grating. The dispersion is reversed on the second pass on the grating, and thus white-light leaves the pre-disperser unit (see, Maihara *et al.*, 1993a). The combined white-light can be then dispersed again by the main spectrograph. The masked out emission lines will not appear in the second dispersion and consequently their wings will not contribute to the total grating scattered light on the second grating reducing it significantly. The practical limitation of the technology is the number of masked lines in the pre-disperser. Examples of such line mask OH suppressor spectrographs include the OH-airglow Suppressor (OHS, Iwamuro *et al.*, 2001), the Cambridge OH Suppression Instrument (COHSI, Piche *et al.*, 1997; Ennico *et al.*, 1998), and The Cambridge Infra-red Panoramic Survey Spectrograph (CIRPASS, Parry *et al.*, 2004).

Fiber Bragg Gratings

Fiber Bragg Gratings (FBGs) are optical fibers in which the core has varying refractive index. By engraving suitable notch spacing in the core the transmission properties of the fiber can be manipulated to generate destructive interference at specific wavelength bands which can be designed to match for example the atmospheric OH lines (Bland-Hawthorn *et al.*, 2004; Bland-Hawthorn *et al.*, 2008). FBGs work only in single mode and thus can not be directly coupled with telescope optics and they require a photonic lantern to convert a large core area fiber coming from telescope to several single mode fibers (Ellis *et al.*, 2020). In the recent years, the FBGs have been the favored method to suppress OH line emission in the SWIR airglow continuum measurement (Ellis *et al.*, 2012; Trinh *et al.*, 2013; Ellis *et al.*, 2020).

6.4 Thermal blocking

The current state-of-the-art HgCdTe detectors used in the NIR and SWIR spectrographs have red sensitivity cutoff at 2.5 μm making them sensitive to the atmospheric and instrumental thermal blackbody radiation (Amado *et al.*, 2012). The atmospheric blackbody radiance increases exponentially close to the cutoff of these detectors, leading to a race condition between the falling detector QE and increasing atmospheric radiance. The peak emission that the detector seems might be close to its cutoff (Amado *et al.*, 2012). Use of monopotassium dihydrogen phosphate (KDP) as a thermal blocking filter for astronomical use has been suggested in the literature (Amado *et al.*, 2012), however no record of its practical application has been found.

KDP and its isomorphic crystals are practically fully transparent in the VIS–NIR wavelengths, but absorb highly in the SWIR (Eimerl, 1987; Weber, 2020), making their transmission properties ideal for use as a NIR shortpass filter. However, two factors make use of KDP challenging: high water solubility (Weber, 1994), and a Curie temperature that is higher than the ambient temperature of a typical astronomical SWIR instrument. Practical application of KDP is studied in Article III.

7 Single-photon sensitive detectors

The spectrograph in Articles I and IV uses an Electron Multiplication Charge-Coupled Device (EMCCD) detector as a statistical photon counter. The EMCCDs are not the only single photon sensitive detector type available, and the ELT era will be characterized by a broader availability of single photon sensitive detector technologies. Some of the detector types usable at the NIR – SWIR wavelengths are presented in this chapter. Several of these types have reached sufficient maturity to be considered for the future astronomical workhorse instrumentation. In addition to the photo-detector technologies, advances have been made in time keeping equipment. Picosecond time resolution has become available with commercial equipment (f.e. Kaur *et al.*, 2017), making photon-counting a viable option for observing brighter targets. In addition to the devices based on photoelectric effect, a variety of superconductive detectors have become available. Typically, the superconductive detectors are found in use at the long-wave IR and sub-millimeter wavelengths, with the trend of moving towards shorter wavelengths.

The history of photon counting in the field of astronomy goes hand-in-hand with the adoption of electronic imaging. The first electronic imaging systems were based on video camera tubes. The working concept of a fully electronic photon-counting system was presented and implemented (Boksenberg *et al.*, 1968; Boksenberg, 1972) around the same time as the Charge-Coupled Devices (CCDs) were invented (Boyle and Smith, 1970). Curious combination of video tube and nuclear emulsion plate (photographic plate with extra thick emulsion layer) called electronograph was also presented (McMullan, 1972).

7.1 Photo-electric effect – multi-sampling

Silicon photo-detectors are very well studied, and especially CCDs are close to becoming a fully mature technology, i.e. their theory is full understood, and the manufactured devices are perfected to the theoretical limit. Silicon band gap at 1.14 eV limits the use of silicon photo-detectors to wavelengths shorter than 1.1 μm. The NIR sensitivity of silicon photo-detectors can be improved by using thicker epitaxial silicon (f.e Groom *et al.*, 2017), possibly further enhanced by applying a nano-textured *'black Silicon'* coating (f.e. Setala *et al.*, 2023).

Skipper CCDs

CCDs can be considered as a mature technology which means that they have been developed to the maximum theoretical achievable performance. Their advantages compared to many other detector types include extremely low dark current, high QE, and 100% filling factor. The limitation of a traditional CCD is their readout noise. The lowest reachable noise in single correlated double sampling (CDS) read is $\sim$2 e^- (f.e. Janesick and Tower, 2016), and the only way beyond $\sim$2 e^- readnoise is to sample the charge multiple times non-destructively. The idea of a floating output gate for CCDa was already suggested soon after their invention (Wen, 1974), but it took decades before the first were manufactured (Chandler *et al.*, 1990; Janesick *et al.*, 1990). The floating output gate CCDs were coined as the *'Skipper'* CCDs (Janesick *et al.*, 1990). The first Skipper CCDs already demonstrated sub-electron readnoise (Chandler *et al.*, 1990; Janesick *et al.*, 1990), but at a level which was still not sufficient for resolving the electron number count in a pixel (meaning $<$0.3 e^-, Janesick and Tower (f.e. 2016)). It took almost 30 years until electron number resolved Skipper CCD was demonstrated (Tiffenberg *et al.*, 2017). These detectors have been applied to dark matter direct detection (Abramoff *et al.*, 2019; Castelló-Mor, 2020; Aguilar-Arevalo *et al.*, 2022).

The practical issue of Tiffenberg *et al.* (2017) results was that it several hours to reach the 0.07 e^- readnoise. Faster readout schemes have been demonstrated since including a selective readout, 'Smart-Skipper', with regions of interest readout multiple times (Chierchie *et al.*, 2021), and Multi-Amplifier Sensing

CCD (MAS-CCD) with multiple output amplifier in series (f.e. Holland, 2023; Lin *et al.*, 2024), which has raised a lot interest in the astronomical community (see the proceedings of the Image Sensors for Precision Astronomy 2024, and the Scientific Detector Workshop 2025).

The advantage of the Skipper CCDs over the other single-photon sensitive detector types is that they can reach the single photon sensitivity simultaneously with high dynamic range, and do not suffer from significant intrinsic noise sources. The Skipper CCDs will exhibit Clock-Induced Charge (CIC) in the same way as EMCCDs, but will suffer from it less than the EMCCDs in statistical photon counting mode. The first Skipper CCDs have been prepared for on-site use (Villalpando *et al.*, 2024)

Electron number resolving CMOS

Similarly to the multi-sampling Skipper and MAS CCDs, multi-sampling Complementary Metal Oxide Semiconductor (CMOS) architectures have been presented recently (f.e. Min-Woong *et al.*, 2015; Ma *et al.*, 2017). This type of detectors are already commercially available, branded as quantitative CMOS (qCMOS)[1]. New multi-sampling CMOS designs being worked on by several manufacturers at the moment, and it may become a norm that the high-end CMOS detectors systematically reach electron number resolving performance. Also, deep-depletion CMOS detectors are being developed (priv. comm. ESO Short Course on High Performance Visible and Infrared Focal Plane Arrays 2025).

7.2 Photo-electric effect – electron avalanche

Silicon CCD and CMOS detectors exist with electron avalanche multiplication schemes. Also, hydrid CMOS for SWIR exists. Electron avalanche process is chaotic. The electron avalanche photo-detectors can be further divided to temporally resolving, and temporally non-resolving types. The temporally non-resolving kind, such as EMCCDs, suffer from the chaotic nature of the electron

[1] `https://www.hamamatsu.com/eu/en/product/cameras/qcmos-cameras.html`

avalanche multiplication, and can count photons only *statistically*. Temporally resolving are true photon counters, but are constrained to observation of relatively faint targets only, since every arriving photon needs to be temporally resolved by the readout circuitry.

EMCCDs

An EMCCD is conceptually very similar to a traditional CCD with the difference of an additional Electron Multiplication (EM) register. After the charge has been shifted to the serial register, it will be clocked through the EM register. Charges in the EM register are shifted with high voltage resulting to an impact ionization events generating more electrons. Probability for a single impact ionization event is low, but once the input signal is clocked through the hundreds of stages in the EM register, the cascade amplification becomes significant.

Since the cascade process is stochastic, the input electron count entering the EM register cannot be unambiguously solved (Harpsøe *et al.*, 2012). However, detections and non-detections can be told apart. Given that the flux λ is kept sufficiently low, this allows using the EMCCDs for statistical photon counting. The thresholding method for statistical photon counting described by Harpsøe *et al.* (2012) has been implemented as a part of *pc-em-tools* software package which has been developed for analysing the data in Article IV [2].

The EMCCDs as statistical photon counting suffers from drawbacks that limit their dynamic range. Due to the EMCCDs performing worse at lower temperatures (Daigle *et al.*, 2008; Daigle *et al.*, 2009), they have to be operated at higher temperatures than conventional CCDs (conventional CCDs at -120°C, EMCCDs at -95°C) which leads to higher dark current observable in longer integrations. In the high flux case, the dynamic range is limited by the probability of generating parallel shift Clock-Induced Charge (pCIC) electrons that are indistinguishable from the photo-electrons. The current state-of-the-art detector controllers[3] reach total CIC of 0.0015 e^- px^{-1} $frame^{-1}$.

[2] https://github.com/JoJoScholarly/pc-em-tools/releases/tag/v0.1.1-beta
[3] https://www.nuvucameras.com/

Avalanche Photodiodes

Avalanche Photo-diodes (APDs) function with the similar cascade multiplication principle as the EMCCDs. In the recent years, there has been a lot development on the silicon APDs. Close to single photon sensitivity has been also demonstrated with HgCdTe silicon hybrid APDs usable at the NIR and SWIR wavelengths (Lanthermann *et al.*, 2019).

7.3 Superconductive detectors

In addition to the classical photo-electric effect based detectors, several different superconductive detector types have been presented in the literature, and some of them have already been applied to astronomical instrumentation. The earliest types to be adopted for astronomical use are Superconductive Tunnel Junctions (STJ) (Peacock *et al.*, 1996) and Microwave Kinetic Inductance Detectors (MKIDs) (Day *et al.*, 2003). Both of them have seen astronomical use, STJs in S-Cam (Rando *et al.*, 2000) and MKIDs in MKID Exoplanet Camera (MEC) (Walter *et al.*, 2020), and DARK-speckle Near-infrared Energy-resolving Superconducting Spectrophotometer (DARKNESS, Meeker *et al.*, 2018).

Both STJs and MKID are based on principle of Cooper pair breaking. An arriving photon breaks Cooper pair and the resulting tunneling current is detected. STJ can be either used as a heterodyne detector, or in combination with Superconducting Quantum Interference Devices (SQUIDs) for direct detection. In direct detection, the concept is similar to that of the MKIDs.

Additionally, Transition Edge Sensors (TES) (f.e. Miller *et al.*, 2003) and Superconductive Nanowire Single-Photon Detector (SNSPD) (Esmaeil Zadeh *et al.*, 2021) are usable in the NIR and SWIR wavelength range.

8 Publications

Article I

Measuring the Near-IR Airglow Continuum with Stray Light Reduced Spectrograph

J. K. M. Viuho, M. I. Andersen and J. P. U. Fynbo

Proc. SPIE 12184, Ground-based and Airborne Instrumentation for Astronomy IX, 2022

In the Article I *"Measuring the Near – IR Airglow Continuum with Stray Light Reduced Spectrograph"* (Viuho *et al.*, 2022) we present a new type white pupil echelle spectrograph which is dedicated for the airglow continuum measurement. The concept is based on an idea originally presented in Andersen and Andersen (1992). Article I spectrograph name Sky Is The Limit Echelle Spectrograph (SKITLES) is the first materialization of the spectrograph type. The concept is simple: a single grating is used in a double-pass with a 90° beam rotation between the two consecutive passes at the grating. As a result, the grating scattered light is directed away from the dispersion axis (Fig. 1 in Article I). We call this design double-X-dispersed spectrograph. As such, the concept is unique, the closest comparison being the double-pass scanning monochromators (Bass *et al.*, 1995, Chpt. 5.5). Double-pass scanning spectrographs have been applied to astronomical observation, for example Coude Echelle Spectrometer (CES, Enard, 1982). The main benefit over a double-pass scanning spectrograph is the fact that the entire spectrum can be recorded at once, in contrast to recording a single spectral element at a time in a scanning spectrograph. The design can be used for applications which require high fidelity spectra, for example to the airglow continuum measurement, the grat-

ing scattered light from the extremely bright atmospheric OH lines pose a risk of contaminating the continuum.

We apply the spectrograph to observations in the publication Article IV. The spectrograph design has been a part of the MSc thesis *"Sky is the limit – an echelle spectrograph with a twist"* (Viuho, 2018).

Article II

The near infrared airglow continuum conundrum – Constraints for ground-based faint object spectroscopy
J. K. M. Viuho, J. P. U. Fynbo, and M. I. Andersen

Published in Astronomy & Astrophysics, 699, A241 (2025)
A draft of this manuscript has been presented on the arXiv with DOI:10.48550/arXiv.2506.02102

In a situation in which the grating scattered light cannot be removed by optical techniques, the total intensity in the atmospheric line scattering wings can be reduced by reducing the spectral bandwidth reaching the grating surface, i.e. OH line avoidance. We have used this strategy in Article II *"The near infrared airglow continuum conundrum – Constraints for ground-based faint object spectroscopy"* (Viuho *et al.*, 2025a), by limiting the total amount of sky light entering the optical train by using a set of $\sim$10 nm wide narrow band filters. The filters are centered at 6700, 7700, 8700 and 10 500 Å. The bandpasses are selected to contain the minimum number of atmospheric OH lines, and are also chosen to be clean of atmospheric water vapor absorption.

We observe at the geographical site of Observatorio del Roque de los Muchachos (ORM), on La Palma, Spain towards a direction that avoids being affected by local light pollution, zodiacal light, and Milky Way. While the SWIR airglow continuum has be studied before at the site (Oliva *et al.*, 2015), we provide the first dedicated measurement in the NIR. We find the zenith equivalent airglow continuum radiance to be 60 – 170 ph $s^{-1}m^{-2}\mu$ $m^{-1}arcsec^{-2}$ in the 6700, 7700, and 8700 Å bandpasses. At 10 500 Å we derive an upper limit of 250 ph $s^{-1}m^{-2}\mu$ $m^{-1}arcsec^{-2}$ since we do not reach a detection due to low

system sensitivity. Allowing for relatively large uncertainties due to temporal variability, zenith scaling, and zodiacal light model used, the results in the 6700 and 7700 Å bands are in line with several earlier measurements at other major observatory sites. The 8700 Å measurement is in accordance to the lower values found in the literature, but also shows statistically significant variability.

Article III

KDP as a thermal blocking filter –
Deep infrared observations with warm narrow band filter

J. K. M. Viuho, A. A. Djupvik, A. N. Sørensen, D. Kumar, P. Steiner, J. P. U. Fynbo, S. Armas, and M. I. Andersen

Submitted to Publications of the Astronomical Society of the Pacific
A draft of this manuscript has been presented on the arXiv with DOI:10.48550/arXiv.2511.11806

Article III differs from the rest of articles by not revolving around grating scattered light. Instead, the article *"KDP as a thermal blocking filter – Deep near IR observations with a warm narrow band filter"* (Viuho *et al.*, 2025b) studies the use of monopotassium dihydrogen phosphate (KDP, KH_2PO_4) as a shortpass filter for use in the NIR and SWIR astronomy. The unique property of KDP and its isomorphic crystals are that they are practically fully transparent from UV to 1.3 μm, while being practically fully opaque at wavelengths longer than 1.3 μm.

This property opens up possibilities for astronomical instrument and filters design. KDP and its isomorphisms can be used as shortpass filter *"glass"* in the filter design. Since wavelengths longer than $\sim$1.8 μm can be blocked by the KDP crystal itself, the dielectric coating defining the filter bandpass does not need to block in the SWIR. As a consequence, the coating can be optimized for a narrower wavelength range, yielding a higher peak transmission, better defined bandpass edges, and better off-band blocking characteristics. Additionally, KDP can be applied to purely thermal blocking applications to limit thermal emission from the sky, or from the instrument structure itself.

We demonstrate KDP practical use in astronomical context by designing an optimized narrow band filter to measure the airglow continuum at 11 910 Å. The measurement extends the wavelength coverage of the Article II towards longer wavelengths. We find the airglow continuum at 11 910 Å to be 19.4 $\mathrm{mag_{AB}}$ $\mathrm{arcsec^{-2}}$, or 770 ph $\mathrm{s^{-1}m^{-2}}\mu$ $\mathrm{m^{-1}arcsec^{-2}}$.

Article IV

On the airglow continuum –
Non-scattered light biased measurement in the range 5500–11 000Å
J. K. M. Viuho, J. P. U. Fynbo, and M. I. Andersen

In preparation

In Article IV *"On the airglow continuum – Non-scattered light biased measurement in the range 5500–11 000 Å"* we present on-sky measurements with the spectrograph described in the Article I. The airglow continuum is clearly visible in the wavelength range 5500 – 9500 Å. In the range 9500 – 11 000 Å the spectrograph sensitivity falls and an upper limit on the airglow continuum level is derived instead. The airglow continuum and the grating scattered light are easily discernible, due to the unique PSF shape of the double-X-dispersed spectrograph design which distributes the grating scattered light away from the dispersion axis.

At the time of submission of the thesis, the data for the publication has been recorded, and a set of software tools called *pc-em-tools*[1] has been implemented for statistically photon counting the EMCCD data. In addition to the quantification of the general level of the airglow continuum radiance at the site of Observatorio del Roque de los Muchachos over a broad wavelength range, the spectral features of FeO and NiO can be searched for and analyzed, shedding light on the site specific photochemistry. HO_2 has distinguishable spectral features in the range 0.8 – 1 μm allowing detection of its presence, or lack of it, at the site broadening the global picture on the origins of the airglow continuum emission.

[1] `https://github.com/JoJoScholarly/pc-em-tools/releases/tag/v0.1.1-beta`

9 Conclusions

With the ever larger telescopes and new detector technologies the sensitivity of astronomical instruments is increasing. The grating scattered light and atmospheric airglow continuum radiance which so far have been largely ignored, are becoming important noise sources. This work has described the current understanding of the atmospheric NIR and SWIR background emission affecting the future ELT era photon-noise limited spectroscopy. The publications included in the thesis have presented original research on the airglow continuum, and studied ways to reduce the effects of instrumental scattered light.

No evidence is found in this thesis that the airglow continuum in the NIR wavelengths would be an instrumental artifact. In fact, the continuum radiance measured with the stray light controlled instrument setups is in accordance with the values reported in the literature, given the relatively large systematic uncertainties due to temporal, spatial, and geographical variability, and the different zodiacal light models used. While the grating scattered light does not seem to be an issue in the NIR, its effect should not be ignored in the SWIR. The brightest and most dense OH lines are located in the H band (1.48 – 1.78 μm), and it has been shown that the observed H band continuum is consistent with grating scattered light in some of the measurements (Sullivan and Simcoe, 2012). To get a certainty on the level in the H band, a double-X-dispersed spectrograph similar to the one presented in Article I should be deployed at these wavelengths.

The airglow continuum radiance has significant latitudinal dependency, and site specific chemiluminescence can be expected (Gattinger *et al.*, 2010). While

the origin of airglow continuum radiance at the site of ORM is not solved in this thesis, other authors have presented a convincing model for the middle latitude airglow radiance in the meanwhile. Recently, the NIR and SWIR continuum radiance climatology at the site of Cerro Paranal, Chile has been modeled in terms of FeO and HO_2 emission (Noll *et al.*, 2024; Noll *et al.*, 2025). The model is based on medium resolution spectra from the VLT/X-Shooter instrument, which might be still affected by the grating scattered light. However, the climatological variability of the OH (the main source of SWIR line emission) and HO_2 (the main source SWIR continuum emission in their model) do not seem to correlate, which were to be expected if the model is affected by the grating scattered light.

The night sky chemiluminescence is a very complex phenomena and is yet to be understood at a global scale. Research on its temporal and geographical behavior should continue in terms of a long-term global monitoring campaign with standardized equipment and simultaneous observation at multiple sites. Such a network could consist of all sky imagers in combination with zenith pointing double-X-dispersed spectrographs presented in this thesis. The temporal cadence must cover the time scales ranging from minutes to years to study the phenomena fully. Such an effort in combination with the revised zodiacal light models should be compiled into a work similar to the *The 1997 reference of diffuse night sky brightness* of Leinert *et al.* (1998).

Bibliography

10

Abramoff, O., L. Barak, I. M. Bloch, *et al.* (2019). In: *Physical Review Letters* 122.16. ISSN: 0031-9007 1079-7114. DOI: 10.1103/PhysRevLett.122.161801.

Aguilar-Arevalo, A., B. Fabricio Alcalde, N. Avalos, *et al.* (2022). In: *arXiv.org*. ISSN: 2331-8422. DOI: 10.48550/arxiv.2202.10518.

Amado, P. J., R. Lenzen, M. C. Cardenas, *et al.* (2012). In: *Modern Technologies in Space- and Ground-based Telescopes and Instrumentation II*. Ed. by R. Navarro, C. R. Cunningham, and E. Prieto. Vol. 8450. Society of Photo-Optical Instrumentation Engineers (SPIE) Conference Series, 84501U. DOI: 10.1117/12.928619.

Andersen, M. I. and J. Andersen (1992). In: *ESO Workshop on High Resolution Spectroscopy with the VLT*. Vol. 40. European Southern Observatory, pp. 235–238. ISBN: 3-923524-43-9.

Arendt, R. G, N. Odegard, J. L Weiland, *et al.* (1998). In: *The Astrophysical Journal* 508.1, pp. 74–105. ISSN: 0004-637X 1538-4357. DOI: 10.1086/306381.

Ashley, M. C. B., M. G. Burton, J. W. V. Storey, *et al.* (1996). In: *Publications of the Astronomical Society of the Pacific* 108, p. 721. DOI: 10.1086/133792.

Baker, D. J. and A. T. Stair (1988). In: *Physica Scripta* 37.4, 611–622. ISSN: 1402-4896. DOI: 10.1088/0031-8949/37/4/021.

Baranne, A. (1972). In: *Auxiliary instrumentation for large telescopes*. Ed. by S. Laustsen and R. A. ESO/CERN, pp. 227–239. eprint: https://www.eso.org/sci/libraries/historicaldocuments/ESO_Conferences_Workshops/Auxiliary_Instrumentation_for_Large_Telescopes.pdf.

Bass, M., E. W. V. Stryland, D. R. Williams, *et al.* (1995). ISBN: 978-0070479746.

Bates, D. R. (1993). In: *Proceedings of the Royal Society of London. Series A: Mathematical and Physical Sciences* 443.1917, pp. 227–237. ISSN: 0962-8444 2053-9177. DOI: 10.1098/rspa.1993.0141.

Bates, D. R. and M. Nicolet (1950). In: *Journal of Geophysical Research (1896-1977)* 55.3, pp. 301–327. ISSN: 2156-2202. DOI: 10.1029/JZ055i003p00301.

Becker, K. H., E. H. Fink, P. Langen, *et al.* (1974). In: *The Journal of Chemical Physics* 60.11, pp. 4623–4625. ISSN: 0021-9606 1089-7690. DOI: 10.1063/1.1680950.

Becker, K. H., W. Groth, and D. Thran (1972). In: *Chemical Physics Letters* 15.2, pp. 215–220. ISSN: 00092614. DOI: 10.1016/0009-2614(72)80152-0.

Benn, C. R. and S. L. Ellison (1998). In: *New Astronomy Reviews* 42.6-8, pp. 503–507. ISSN: 13876473. DOI: 10.1016/s1387-6473(98)00062-1.

Bland-Hawthorn, J., A. Buryak, and K. Kolossovski (2008). In: *Journal of the Optical Society of America A* 25.1, p. 153. DOI: 10.1364/JOSAA.25.000153.

Bland-Hawthorn, J., M. Englund, and G. Edvell (2004). In: *Optics Express* 12.24, p. 5902. DOI: 10.1364/OPEX.12.005902.

Bock, J. J., A. M. Aboobaker, J. Adamo, *et al.* (2025). In: *arXiv e-prints*, arXiv:2511.02985. DOI: 10.48550/arXiv.2511.02985.

Boksenberg, A. (1972). In: *Auxiliary instrumentation for large telescopes*. Ed. by S. Laustsen and R. A. ESO/CERN, pp. 295 –316. eprint: https://www.eso.org/sci/libraries/historicaldocuments/ESO_Conferences_Workshops/Auxiliary_Instrumentation_for_Large_Telescopes.pdf.

Boksenberg, A., R. L. F. Boyd, and J. C. Jones (1968). In: *Nature* 220.5167, p. 5. DOI: 10.1038/220556a0.

Boyle, W. S. and G. E. Smith (1970). In: *Bell System Technical Journal* 49.4, pp. 587–593. ISSN: 00058580. DOI: 10.1002/j.1538-7305.1970.tb01790.x.

Brooke, J. S. A., P. F. Bernath, C. M. Western, *et al.* (2016). In: *Journal of Quantitative Spectroscopy and Radiative Transfer* 168, pp. 142–157. ISSN: 0022-4073. DOI: https://doi.org/10.1016/j.jqsrt.2015.07.021.

Carleton, T., R. A. Windhorst, R. O'Brien, *et al.* (2022). In: *The Astronomical Journal* 164.5. ISSN: 0004-6256 1538-3881. DOI: 10.3847/1538-3881/ac8d02.

Castelló-Mor, N. (2020). In: *Nuclear instruments & methods in physics research. Section A, Accelerators, spectrometers, detectors and associated equipment* 958, p. 162933. ISSN: 0168-9002. DOI: 10.1016/j.nima.2019.162933.

Chandler, C. E., R. A. Bredthauer, J. R. Janesick, *et al.* (1990). In: *Charge-Coupled Devices and Solid State Optical Sensors*. Ed. by M. M. Blouke. Vol. 1242. Society of Photo-Optical Instrumentation Engineers (SPIE) Conference Series, pp. 238–251. DOI: 10.1117/12.19457.

Chierchie, F., G. F. Moroni, L. Stefanazzi, *et al.* (2021). In: *Phys Rev Lett* 127.24, p. 241101. ISSN: 1079-7114. DOI: 10.1103/PhysRevLett.127.241101.

Christensen, L. L., S. Noll, and P. Horálek (2016). In: *The Messenger* 163, pp. 40–42. eprint: https://www.eso.org/sci/publications/messenger/archive/no.163-mar16/messenger-no163-40-42.pdf.

Cinzano, P. and C. D. Elvidge (2004). In: *Monthly Notices of the Royal Astronomical Society* 353.4, pp. 1107–1116. DOI: 10.1111/j.1365-2966.2004.08132.x.

Content, R. (1996). In: *The Astrophysical Journal* 464.1, pp. 46–53. ISSN: 0004-637X 1538-4357. DOI: 10.1086/177332.

Content, R. and J. R. P. Angel (1994). In: *Instrumentation in Astronomy VIII*. Ed. by D. L. Crawford and E. R. Craine. Vol. 2198. Society of Photo-Optical Instrumentation Engineers (SPIE) Conference Series, pp. 757–762. DOI: 10.1117/12.176730.

Cuby, J. G., C. Lidman, and C. Moutou (2000). In: *The Messenger* 101, pp. 2–8. eprint: https://www.eso.org/sci/publications/messenger/archive/no.101-sep00/messenger-no101.pdf.

Daigle, O., C. Carignan, J.-L. Gach, *et al.* (2009). In: *Publications of the Astronomical Society of the Pacific* 121.882, p. 866. ISSN: 1538-3873. DOI: 10.1117/12.788929.

Daigle, O., J.-L. Gach, C. Guillaume, *et al.* (2008). Vol. 7014. SPIE Astronomical Telescopes + Instrumentation. SPIE. DOI: 10.1117/12.788929.

Day, P. K., H. G. LeDuc, B. A. Mazin, *et al.* (2003). In: *Nature* 425.6960, pp. 817–821. ISSN: 1476-4687. DOI: 10.1038/nature02037.

Dravins, D. (1978). In: *Applied Optics* 17.3, pp. 404–414. ISSN: 2155-3165. DOI: 10.1364/AO.17.000404.

Dwek, E. and R. G. Arendt (1998). In: *The Astrophysical Journal* 508.1, pp. L9–L12. DOI: 10.1086/311714.

Eimerl, D. (1987). In: *Ferroelectrics* 72.1, pp. 95–139. DOI: 10.1080/00150198708017942.

Ellis, S. C. and J. Bland-Hawthorn (2008). In: *Monthly Notices of the Royal Astronomical Society* 386.1, pp. 47–64. ISSN: 00358711 13652966. DOI: 10.1111/j.1365-2966.2008.13021.x.

Ellis, S. C., J. Bland-Hawthorn, J. Lawrence, *et al.* (2012). In: *Monthly Notices of the Royal Astronomical Society* 425.3, pp. 1682–1695. ISSN: 00358711. DOI: 10.1111/j.1365-2966.2012.21602.x.

Ellis, S. C., J. Bland-Hawthorn, J. S. Lawrence, *et al.* (2020). In: *Monthly Notices of the Royal Astronomical Society* 492.2, pp. 2796–2806. ISSN: 0035-8711. DOI: 10.1093/mnras/staa028.

Ellis, S. C., S. Kuhlmann, K. Kuehn, *et al.* (2017). In: *Opt Express* 25.14, pp. 15868–15889. ISSN: 1094-4087 (Electronic) 1094-4087 (Linking). DOI: 10.1364/OE.25.015868.

Elvey, C. T. (1950). In: *The Astrophysical Journal* 111. ISSN: 0004-637X 1538-4357. DOI: 10.1086/145278.

Enard, D. (1982). In: *Instrumentation in Astronomy IV*. Ed. by D. L. Crawford. Vol. 331. Society of Photo-Optical Instrumentation Engineers (SPIE) Conference Series, pp. 232–242. DOI: 10.1117/12.933460.

Ennico, K. A., I. R. Parry, M. A. Kenworthy, *et al.* (1998). In: *Infrared Astronomical Instrumentation*. Ed. by A. M. Fowler. Vol. 3354. Society of Photo-Optical Instrumentation Engineers (SPIE) Conference Series, pp. 668–674. DOI: 10.1117/12.317329.

Esmaeil Zadeh, I., J. Chang, J. W. N. Los, *et al.* (2021). In: *Applied Physics Letters* 118.19. ISSN: 0003-6951 1077-3118. DOI: 10.1063/5.0045990.

Espy, A. J., S. F. Dermott, T. J. J. Kehoe, *et al.* (2009). In: *Planetary and Space Science* 57.2, pp. 235–242. ISSN: 00320633. DOI: 10.1016/j.pss.2008.06.011.

Euclid Collaboration, Y. Mellier, Abdurro'uf, *et al.* (2025). In: *Astronomy & Astrophysics* 697, A1. DOI: 10.1051/0004-6361/202450810.

Evans, W. F. J., R. L. Gattinger, A. L. Broadfoot, *et al.* (2011). In: *Atmospheric Chemistry and Physics* 11.18, pp. 9595–9603. ISSN: 1680-7324. DOI: 10.5194/acp-11-9595-2011.

Evans, W. F. J., R. L. Gattinger, T. G. Slanger, *et al.* (2010). In: *Geophysical Research Letters* 37.22. ISSN: 0094-8276 1944-8007. DOI: 10.1029/2010gl045310.

Falchi, F., P. Cinzano, D. Duriscoe, *et al.* (2016). In: *Science Advances* 2.6, e1600377. DOI: 10.1126/sciadv.1600377.

Falchi, F., F. Ramos, S. Bará, *et al.* (2023). In: *Monthly Notices of the Royal Astronomical Society* 519.1, pp. 26–33. ISSN: 0035-8711 1365-2966. DOI: 10.1093/mnras/stac2929.

Forsyth, R. J. and P. C. Wraight (1987). In: *Planetary and Space Science* 35.11, pp. 1449–1461. ISSN: 00320633. DOI: 10.1016/0032-0633(87)90057-2.

Gadsden, M. and E. Marovich (1973). In: *Journal of Atmospheric and Terrestrial Physics* 35.9, pp. 1601–1614. ISSN: 00219169. DOI: 10.1016/0021-9169(73)90179-7.

Gallardo-Lacourt, B., H. U. Frey, and C. Martinis (2021). In: *Space Science Reviews* 217.1. ISSN: 0038-6308 1572-9672. DOI: 10.1007/s11214-020-00776-6.

Gallardo-Lacourt, B., J. Liang, Y. Nishimura, *et al.* (2018). In: *Geophysical Research Letters* 45.16, pp. 7968–7973. ISSN: 0094-8276 1944-8007. DOI: 10.1029/2018gl078509.

Garstang, R. H. (1986). In: *Publications of the Astronomical Society of the Pacific* 98, pp. 364–375. DOI: 10.1086/131768.

Garstang, R. H. (1989). In: *Publications of the Astronomical Society of the Pacific* 101. ISSN: 0004-6280 1538-3873. DOI: 10.1086/132436.

Gattinger, R. L., I. C. McDade, A. L. Alfaro Suzán, *et al.* (2010). In: *Journal of Geophysical Research: Atmospheres* 115.D12. ISSN: 0148-0227. DOI: 10.1029/2009jd013205.

Gerhard, C. (2017). eng. Optical Sciences and Applications of Light. CRC Press. ISBN: 1-4987-6461-4.

Gillies, D. M., E. Donovan, D. Hampton, *et al.* (2019). In: *Geophysical Research Letters* 46.13, pp. 7207–7213. ISSN: 0094-8276 1944-8007. DOI: 10.1029/2019gl083272.

Gillmon, K. and J. M. Shull (2006). In: *The Astrophysical Journal* 636.2, pp. 908–915. DOI: 10.1086/498055.

Gorjian, V., E. L. Wright, and R. R. Chary (2000). In: *The Astrophysical Journal* 536.2, pp. 550–560. ISSN: 0004-637X 1538-4357. DOI: 10.1086/308974.

Groom, D. E., S. Haque, S. E. Holland, *et al.* (2017). In: *Journal of Applied Physics* 122.5, p. 055301. DOI: 10.1063/1.4986506.

Grygalashvyly, M., A. I. Pogoreltsev, A. B. Andreyev, *et al.* (2021). In: *Annales Geophysicae* 39.1, pp. 255–265. ISSN: 1432-0576. DOI: 10.5194/angeo-39-255-2021.

Gustafson, B. A. S. (1994). eng. In: *Annual review of earth and planetary sciences* 22.1, pp. 553–595. ISSN: 0084-6597.

Haghi, K. R. and D. R. Durran (2021). In: *Journal of the Atmospheric Sciences* 78.1, pp. 313–327. ISSN: 0022-4928 1520-0469. DOI: 10.1175/jas-d-20-0181.1.

Hanuschik, R. W. (2003). In: *Astronomy and Astrophysics* 407.3, pp. 1157–1164. ISSN: 0004-6361 1432-0746. DOI: 10.1051/0004-6361:20030885.

Harpsøe, K. B. W., M. I. Andersen, and P. Kjægaard (2012). In: *Astronomy & Astrophysics* 537, A50. ISSN: 0004-6361, 1432-0746. DOI: 10.1051/0004-6361/201117089.

Hayakawa, H., K. Iwahashi, Y. Ebihara, *et al.* (2017). In: *The Astrophysical Journal* 850.2. ISSN: 2041-8213. DOI: 10.3847/2041-8213/aa9661.

He, F., Y. Wei, and W. Wan (2020). In: *Natl Sci Rev* 7.10, pp. 1606–1615. ISSN: 2053-714X (Electronic) 2095-5138 (Print) 2053-714X (Linking). DOI: 10.1093/nsr/nwaa083.

Herbst, T. M. (1994). In: *Publications of the Astronomical Society of the Pacific* 106, p. 1298. DOI: 10.1086/133507.

Holland, S. E. (2023). In: *Astronomische Nachrichten* 344.8-9. ISSN: 0004-6337 1521-3994. DOI: 10.1002/asna.20230072.

Horálek, P., L. L. Christensen, J. Bór, *et al.* (2016a). In: *The Messenger* 163, pp. 43–45. eprint: https://www.eso.org/sci/publications/messenger/archive/no.163-mar16/messenger-no163-43-45.pdf.

Horálek, P., L. L. Christensen, D. Nesvorný, *et al.* (2016b). In: *The Messenger* 164, pp. 45–47. eprint: https://www.eso.org/sci/publications/messenger/archive/no.164-jun16/messenger-no164-45-47.pdf.

Iwamuro, F., K. Motohara, T. Maihara, *et al.* (2001). In: *Publications of the Astronomical Society of Japan* 53.2, pp. 355–360. DOI: 10.1093/pasj/53.2.355.

Janesick, J. and J. Tower (2016). In: *Sensors (Basel)* 16.5. ISSN: 1424-8220 (Electronic) 1424-8220 (Linking). DOI: 10.3390/s16050688.

Janesick, J. R., T. Elliott, A. Dingizian, *et al.* (1990). In: *Charge-Coupled Devices and Solid State Optical Sensors*. Ed. by M. M. Blouke. Vol. 1242. Society of Photo-Optical Instrumentation Engineers (SPIE) Conference Series, pp. 223–237. DOI: 10.1117/12.19452.

Jones, A., S. Noll, W. Kausch, *et al.* (2013). In: *Astronomy & Astrophysics* 560. ISSN: 0004-6361 1432-0746. DOI: 10.1051/0004-6361/201322433.

Jorgensen, J. L., M. Benn, J. E. P. Connerney, *et al.* (2021). In: *Journal of Geophysical Research: Planets* 126.3. ISSN: 2169-9097 2169-9100. DOI: 10.1029/2020je006509.

Kasten, F. (1965). In: *Archives for Meteorology Geophysics and Bioclimatology Series B Theoretical and Applied Climatology* 14.2, pp. 206–223. DOI: 10.1007/BF02248840.

Kasten, F. and A. T. Young (1989). In: *Appl. Opt.* 28.22, pp. 4735–4738. DOI: 10.1364/AO.28.004735.

Kaur, N., F. Frank, P.-E. Pottie, *et al.* (2017). In: *2017 Joint Conference of the European Frequency and Time Forum and IEEE International Frequency Control Symposium (EFTF/IFCS)*, pp. 86–90. DOI: 10.1109/FCS.2017.8088808.

Kelsall, T., J. L Weiland, B. A Franz, *et al.* (1998). In: *The Astrophysical Journal* 508.1, pp. 44–73. ISSN: 0004-637X 1538-4357. DOI: 10.1086/306380.

Kenner, R. D. and E. A. Ogryzlo (1984). In: *Journal of Chemical Physics* 80.1, pp. 1–6. DOI: 10.1063/1.446479.

Khomich, V. Y., A. I. Semenov, and N. N. Shefov (2008). eng. 1. Aufl. Berlin, Heidelberg: Springer-Verlag. ISBN: 9783540758327.

King, D. L (1985). RGO/La Palma technical note no 31. eprint: https://www.ing.iac.es/Astronomy/observing/manuals/ps/tech_notes/tn031.pdf.

Kirillov, A. S., V. B. Belakhovsky, E. A. Maurchev, *et al.* (2023). In: *Geomagnetism and Aeronomy* 63.6, pp. 802–810. DOI: 10.1134/S0016793223600637.

Knudsen, D. J., J. E. Borovsky, T. Karlsson, *et al.* (2021). In: *Space Science Reviews* 217.1. ISSN: 0038-6308 1572-9672. DOI: 10.1007/s11214-021-00798-8.

Knupp, K. (2006). In: *Journal of the Atmospheric Sciences* 63.8, pp. 2016–2035. DOI: 10.1175/JAS3731.1.

Koch, F., M. Zilk, and T. Glaser (2021). In: *Modeling Aspects in Optical Metrology VIII*. Ed. by B. Bodermann, K. Frenner, and B. M. Barnes. Vol. 11783. Society of Photo-Optical Instrumentation Engineers (SPIE) Conference Series, p. 1178304. DOI: 10.1117/12.2591771.

Krassovsky, V. I., N. N. Shefov, and V. I. Yarin (1951). In: *Bokl. Akad. Nauk. SSSR* 78, pp. 669–672.

Krisciunas, K. (1997). In: *Publications of the Astronomical Society of the Pacific* 109, pp. 1181–1188. DOI: 10.1086/133993.

Krisciunas, K. and B. E. Schaefer (1991). In: *Publications of the Astronomical Society of the Pacific* 103. ISSN: 0004-6280 1538-3873. DOI: 10.1086/132921.

Lanthermann, C., N. Anugu, J. B. Le Bouquin, *et al.* (2019). In: *Astronomy & Astrophysics* 625. ISSN: 0004-6361 1432-0746. DOI: 10.1051/0004-6361/201935043.

Laskar, F. I., D. Pallamraju, B. Veenadhari, *et al.* (2015). In: *Advances in Space Research* 55.6, pp. 1651–1659. ISSN: 02731177. DOI: 10.1016/j.asr.2014.12.040.

Leinert, C., P. Vaisanen, K. Mattila, *et al.* (1995). In: *Astronomy and Astrophysics Supplement Series* 112, p. 99. eprint: https://ui.adsabs.harvard.edu/abs/1995A&AS..112...99L.

Leinert, C., S. Bowyer, L. K. Haikala, *et al.* (1998). In: *Astronomy and Astrophysics Supplement Series* 127.1, pp. 1–99. ISSN: 0365-0138 1286-4846. DOI: 10.1051/aas:1998105.

Levasseur-Regourd, A. C. and R. Dumont (1980). In: *Astronomy & Astrophysics* 84, pp. 277–279. eprint: https://ui.adsabs.harvard.edu/abs/1980A&A...84..277L.

Lin, K. W., A. Karcher, J. Guy, *et al.* (2024). In: *Publications of the Astronomical Society of the Pacific* 136.9. ISSN: 0004-6280 1538-3873. DOI: 10.1088/1538-3873/ad716c.

Liou, K.-N. (2002). eng. 2. ed. International geophysics series ; 84. San Diego, Calif. ; Academic. ISBN: 0124514510.

Loewen, E. G. and E. Popov (1997). eng. First edition. Optical engineering ; 58. Boca Raton, FL: CRC Press. ISBN: 9781351830737.

Loo, M. P. J. van der and G. C. Groenenboom (2007). In: *The Journal of Chemical Physics* 126.11, p. 114314. ISSN: 0021-9606. DOI: 10.1063/1.2646859.

Loo, M. P. J. van der and G. C. Groenenboom (2008). In: *The Journal of Chemical Physics* 128.15, p. 159902. ISSN: 0021-9606. DOI: 10.1063/1.2899016.

Low, F. J., D. A. Beintema, T. N. Gautier, *et al.* (1984). In: *Astrophysical Journal, Letters* 278, pp. L19–L22. DOI: 10.1086/184213.

Ma, J., S. Masoodian, D. A. Starkey, *et al.* (2017). In: *Optica* 4.12. ISSN: 2334-2536. DOI: 10.1364/optica.4.001474.

Maihara, T., F. Iwamuro, D. N. B. Hall, *et al.* (1993a). In: *Infrared Detectors and Instrumentation*. Vol. 1946. International Society for Optics and Photonics, pp. 581–586. DOI: 10.1117/12.158709.

Maihara, T., F. Iwamuro, T. Yamashita, *et al.* (1993b). In: *Publications of the Astronomical Society of the Pacific* 105.691, p. 940. ISSN: 1538-3873. DOI: 10.1086/133259.

Martinis, C., J. Baumgardner, M. Mendillo, *et al.* (2019). In: *Journal of Geophysical Research: Space Physics* 124.6, pp. 4658–4671. ISSN: 2169-9380 2169-9402. DOI: 10.1029/2018ja026017.

Martinis, C., I. Griffin, B. Gallardo-Lacourt, *et al.* (2022). In: *Journal of Geophysical Research Letters* 49.11, e98511. DOI: 10.1029/2022GL098511.

McMullan, D. (1972). In: *Auxiliary Instrumentation for Large Telescopes*. Ed. by S. Laustsen and A. Reiz, pp. 433–443. eprint: https://ui.adsabs.harvard.edu/abs/1972ailt.conf..433M.

Meeker, S. R., B. A. Mazin, A. B. Walter, *et al.* (2018). In: *Publications of the Astronomical Society of the Pacific* 130.988, p. 065001. DOI: 10.1088/1538-3873/aab5e7.

Meinel, A. B. (1950a). In: *The Astrophysical Journal* 111. ISSN: 0004-637X 1538-4357. DOI: 10.1086/145296.

Meinel, A. B. (1950b). In: *The Astrophysical Journal* 112. ISSN: 0004-637X 1538-4357. DOI: 10.1086/145321.

Miller, A. J., S. W. Nam, J. M. Martinis, *et al.* (2003). In: *Applied Physics Letters* 83.4, p. 791. DOI: 10.1063/1.1596723.

Milvang-Jensen, B., W. Freudling, J. Zabl, *et al.* (2013). In: *Astronomy & Astrophysics* 560, A94. DOI: 10.1051/0004-6361/201321814.

Min-Woong, S., S. Kawahito, K. Kagawa, *et al.* (2015). In: *IEEE Electron Device Letters* 36.12, pp. 1344–1347. ISSN: 0741-3106 1558-0563. DOI: 10.1109/led.2015.2496359.

Moreels, G., J. Clairemidi, M. Faivre, *et al.* (2008). In: *Experimental Astronomy* 22.1, p. 87. ISSN: 1572-9508. DOI: 10.1007/s10686-008-9089-6.

Nguyen, H. T., B. J. Rauscher, S. A. Severson, *et al.* (1996). In: *Publications of the Astronomical Society of the Pacific* 108, p. 718. DOI: 10.1086/133791.

Nguyen, H. T., M. Zemcov, J. Battle, *et al.* (2016). In: *Publications of the Astronomical Society of the Pacific* 128.967, p. 094504. ISSN: 0004-6280 1538-3873. DOI: 10.1088/1538-3873/128/967/094504.

Noll, S., W. Kausch, M. Barden, *et al.* (2012). In: *Astronomy & Astrophysics* 543. ISSN: 0004-6361 1432-0746. DOI: 10.1051/0004-6361/201219040.

Noll, S., C. Schmidt, W. Kausch, *et al.* (2023). In: *Journal of Geophysical Research: Atmospheres* 128.9. ISSN: 2169-897X 2169-8996. DOI: 10.1029/2022jd038275.

Noll, S., S. Kimeswenger, B. Proxauf, *et al.* (2017). In: *Journal of Atmospheric and Solar-Terrestrial Physics* 163, pp. 54–69. ISSN: 1364-6826. DOI: 10.1016/j.jastp.2017.05.012.

Noll, S., J. M. C. Plane, W. Feng, *et al.* (2024). In: *Atmospheric Chemistry and Physics* 24.2, pp. 1143–1176. ISSN: 1680-7324. DOI: 10.5194/acp-24-1143-2024.

Noll, S., C. Schmidt, P. Hannawald, *et al.* (2025). In: *Geoscientific Model Development* 18.14, pp. 4353–4398. ISSN: 1991-9603. DOI: 10.5194/gmd-18-4353-2025.

Noxon, J. F. (1978). In: *Planetary and Space Science* 26.2, pp. 191–192. ISSN: 00320633. DOI: 10.1016/0032-0633(78)90019-3.

O'Brien, R., R. G. Arendt, R. A. Windhorst, *et al.* (2025). In: *arXiv e-prints*, arXiv:2510.18231. DOI: 10.48550/arXiv.2510.18231.

Oliva, E., L. Origlia, S. Scuderi, *et al.* (2015). In: *Astronomy & Astrophysics* 581, A47. ISSN: 0004-6361, 1432-0746. DOI: 10.1051/0004-6361/201526291.

Oliveira, D. M., H. Hayakawa, A. Bhaskar, *et al.* (2020). In: *Earth, Planets and Space* 72.1, p. 82. DOI: 10.1186/s40623-020-01208-z.

Osterbrock, D. E., J. P. Fulbright, A. R. Martel, *et al.* (1996). In: *Publications of the Astronomical Society of the Pacific* 108. ISSN: 0004-6280 1538-3873. DOI: 10.1086/133722.

Palmer, C. (2020). Richardson Gratings, MKS Instruments, Inc. eprint: https://www.newport.com/mam/celum/celum_assets/np/resources/MKS_Diffraction_Grating_Handbook.pdf.

Parry, I., A. Bunker, A. Dean, *et al.* (2004). In: *Ground-based Instrumentation for Astronomy*. Ed. by A. F. M. Moorwood and M. Iye. Vol. 5492. Society of Photo-Optical Instrumentation Engineers (SPIE) Conference Series, pp. 1135–1144. DOI: 10.1117/12.552012.

Patat, F. (2008). In: *Astronomy & Astrophysics* 481.2, pp. 575–591. ISSN: 0004-6361 1432-0746. DOI: 10.1051/0004-6361:20079279.

Peacock, A., P. Verhoeve, N. Rando, *et al.* (1996). In: *Nature* 381.6578, pp. 135–137. ISSN: 0028-0836 1476-4687. DOI: 10.1038/381135a0.

Pertsev, N. and V. Perminov (2008). In: *Annales Geophysicae* 26.5, pp. 1049–1056. ISSN: 0992-7689. DOI: https://doi.org/10.5194/angeo-26-1049-2008.

Piche, F., I. R. Parry, K. Ennico, *et al.* (1997). In: *Optical Telescopes of Today and Tomorrow*. Ed. by A. L. Ardeberg. Vol. 2871. Society of Photo-Optical Instrumentation Engineers (SPIE) Conference Series, pp. 1332–1341. DOI: 10.1117/12.269025.

Plane, J. M., W. Feng, and E. C. Dawkins (2015). In: *Chem Rev* 115.10, pp. 4497–541. ISSN: 1520-6890. DOI: 10.1021/cr500501m.

Rando, N., J. Verveer, S. Andersson, *et al.* (2000). In: *Review of Scientific Instruments* 71.12. ISSN: 00346748. DOI: 10.1063/1.1326055.

Roth, K. C., A. Smith, A. Stephens, *et al.* (2016). In: *Observatory Operations: Strategies, Processes, and Systems VI*. Ed. by A. B. Peck, R. L. Seaman, and C. R. Benn. Vol. 9910. Society of Photo-Optical Instrumentation Engineers (SPIE) Conference Series, 99101B. DOI: 10.1117/12.2233891.

Rousselot, P., C. Lidman, J.-G. Cuby, *et al.* (2000). In: *Astronomy and Astrophysics* 354, p.1134–1150. eprint: http://telbib.eso.org/detail.php?bibcode=2000A%26A...354.1134R.

Sadlowski, S., T. Harzendorf, S. Schwinde, *et al.* (2020). In: *Advances in Optical and Mechanical Technologies for Telescopes and Instrumentation IV*. Ed. by R. Navarro and R. Geyl. Vol. 11451. Society of Photo-Optical Instrumentation Engineers (SPIE) Conference Series, p. 114511D. DOI: 10.1117/12.2562546.

Sano, K., S. Matsuura, K. Yomo, *et al.* (2020). In: *The Astrophysical Journal* 901.2, p. 112. DOI: 10.3847/1538-4357/abad3d.

Savigny, C. von, I. C. McDade, K. U. Eichmann, *et al.* (2012). In: *Atmospheric Chemistry and Physics* 12.18, pp. 8813–8828. ISSN: 1680-7324. DOI: 10.5194/acp-12-8813-2012.

Setala, O. E., M. J. Prest, K. D. Stefanov, *et al.* (2023). In: *Small* 19.47, e2304001. ISSN: 1613-6829 (Electronic) 1613-6810 (Linking). DOI: 10.1002/smll.202304001.

Smith, A. K. (2012). In: *Surveys in Geophysics* 33.6, pp. 1177–1230. DOI: 10.1007/s10712-012-9196-9.

Smith, S. M., J. Scheer, E. R. Reisin, *et al.* (2006). In: *Journal of Geophysical Research Space Physics* 111.A9. ISSN: 0148-0227. DOI: 10.1029/2005ja011197.

Sobolev, V. G. (1978). In: *Planetary and Space Science* 26.7, pp. 703–704. ISSN: 00320633. DOI: 10.1016/0032-0633(78)90103-4.

Sternberg, J. R. and M. F. Ingham (1972). In: *Monthly Notices of the Royal Astronomical Society* 159.1, pp. 1–20. ISSN: 0035-8711 1365-2966. DOI: 10.1093/mnras/159.1.1.

Sullivan, P. W. and R. A. Simcoe (2012). In: *Publications of the Astronomical Society of the Pacific* 124.922, p. 1336. ISSN: 1538-3873. DOI: 10.1086/668849.

Tiffenberg, J., M. Sofo-Haro, A. Drlica-Wagner, *et al.* (2017). In: *Physical Review Letters* 119.13, p. 131802. DOI: 10.1103/PhysRevLett.119.131802.

Tilvi, V., J. E. Rhoads, P. Hibon, *et al.* (2010). In: *The Astrophysical Journal* 721.2, pp. 1853–1860. ISSN: 0004-637X, 1538-4357. DOI: 10.1088/0004-637x/721/2/1853.

Trinh, C. Q., S. C. Ellis, J. Bland-Hawthorn, *et al.* (2013). In: *Monthly Notices of the Royal Astronomical Society* 432.4, pp. 3262–3277. ISSN: 0035-8711. DOI: 10.1093/mnras/stt677.

Tsumura, K., T. Matsumoto, S. Matsuura, *et al.* (2013). In: *Publications of the Astronomical Society of Japan* 65.6. ISSN: 0004-6264 2053-051X. DOI: 10.1093/pasj/65.6.119.

Unterguggenberger, S., S. Noll, W. Feng, *et al.* (2017). In: *Atmospheric Chemistry & Physics* 17.6, pp. 4177–4187. DOI: 10.5194/acp-17-4177-2017.

Vallance Jones, A. and R. L. Gattinger (1971). In: *The Radiating Atmosphere*. Ed. by B. M. McCormack. Vol. 24. Astrophysics and Space Science Library, p. 176. DOI: 10.1007/978-90-277-0184-8_17.

van Rhijn, P. J. (1921). In: *Publications of the Kapteyn Astronomical Laboratory Groningen* 31, pp. 1–83. eprint: https://ui.adsabs.harvard.edu/abs/1921PGro...31....1V.

Venemans, B. P., R. G. McMahon, I. R. Parry, *et al.* (2009). In: *Science with the VLT in the ELT Era*. Vol. 9. Astrophysics and Space Science Proceedings, p. 187. DOI: 10.1007/978-1-4020-9190-2_32.

Verkhoglyadova, O. P., J. M. Wissing, S. Wang, *et al.* (2016). In: *Journal of Geophysical Research: Space Physics* 121.7, pp. 6017–6030. ISSN: 2169-9380 2169-9402. DOI: 10.1002/2015ja022217.

Vernet, J., H. Dekker, S. D'Odorico, *et al.* (2011). In: *Astronomy & Astrophysics* 536, A105. DOI: 10.1051/0004-6361/201117752.

Villalpando, E. M., A. Drlica-Wagner, A. A. Plazas Malagón, *et al.* (2024). In: *Publications of the Astronomical Society of the Pacific* 136.4. ISSN: 0004-6280 1538-3873. DOI: 10.1088/1538-3873/ad2865.

Viuho, J. (2018). MSc Thesis, The sky is the limit : An echelle spectrography with a twist.

Viuho, J. K. M., A. A. Djupvik, A. N. Sørensen, *et al.* (2025b). In: *arXiv e-prints*, arXiv:2511.11806. DOI: 10.48550/arXiv.2511.11806.

Viuho, J. K. M., J. P. U. Fynbo, and M. I. Andersen (2025a). In: *Astronomy & Astrophysics* 699, A241. DOI: 10.1051/0004-6361/202553726.

Viuho, J., M. I. Andersen, and J. U. Fynbo (2022). In: *Ground-based and Airborne Instrumentation for Astronomy IX*. Ed. by C. J. Evans, J. J. Bryant, and K. Motohara, p. 1218456. DOI: 10.1117/12.2630668.

Vázquez, M. and J. M. Vaquero (2010). In: *Solar Physics* 267.2, pp. 431–444. ISSN: 0038-0938 1573-093X. DOI: 10.1007/s11207-010-9650-0.

Walter, A. B., N. Fruitwala, S. Steiger, *et al.* (2020). In: *Publications of the Astronomical Society of the Pacific* 132.1018. ISSN: 1538-3873. DOI: 10.1088/1538-3873/abc60f.

Walterscheid, R. L., J. H. Hecht, L. J. Gelinas, *et al.* (2012). In: *Journal of Geophysical Research: Atmospheres* 117.D22. ISSN: 0148-0227. DOI: 10.1029/2012jd017847.

Weber, M. J. (1994). eng. The CRC Press laser and optical science and technology series. Boca Raton: CRC Press. ISBN: 1-00-306795-6.

Weber, M. J. (2020). eng. 1st edition. Vol. 8. CRC Handbook of Laser Science and Technology. United Kingdom: CRC Press. ISBN: 9781000102772.

Wen, D. D. (1974). In: *IEEE Journal of Solid-State Circuits* 9.6, pp. 410–414. ISSN: 1558-173X. DOI: 10.1109/JSSC.1974.1050535.

West, J. B. and H. P. Broida (1975). In: *The Journal of Chemical Physics* 62.7, pp. 2566–2574. ISSN: 0021-9606 1089-7690. DOI: 10.1063/1.430837.

Windhorst, R. A., T. Carleton, R. O'Brien, *et al.* (2022). In: *The Astronomical Journal* 164.4. ISSN: 0004-6256 1538-3881. DOI: 10.3847/1538-3881/ac82af.

Windhorst, R. A., S. H. Cohen, N. P. Hathi, *et al.* (2011). In: *The Astrophysical Journal Supplement* 193.2, p. 27. DOI: 10.1088/0067-0049/193/2/27.

Wolstencroft, R. D. and I. G. van Breda (1967). In: *The Astrophysical Journal* 147. ISSN: 0004-637X 1538-4357. DOI: 10.1086/148997.

Woods, T. N., R. T. Wrigley, G. J. Rottman, *et al.* (1994). In: *Applied Optics* 33.19, pp. 4273–4285. ISSN: 2155-3165. DOI: 10.1364/AO.33.004273.

Wraight, P. C. (1986). In: *Planetary and space science* 34.12, pp. 1373–1373. DOI: 10.1016/0032-0633(86)90073-5.

Wright, E. L. (1998). In: *The Astrophysical Journal* 496.1, pp. 1–8. ISSN: 0004-637X 1538-4357. DOI: 10.1086/305345.

Xu, J., H. Gao, A. K. Smith, *et al.* (2012). In: *Journal of Geophysical Research: Atmospheres* 117.D2. ISSN: 2156-2202. DOI: 10.1029/2011JD016342.

List of publications

11

Article I **Measuring the Near-IR Airglow Continuum with Stray Light Reduced Spectrograph**
J. K. M. Viuho, M. I. Andersen and J. P. U. Fynbo

Proc. SPIE 12184, Ground-based and Airborne Instrumentation for Astronomy IX, 2022

Article II **The near infrared airglow continuum conundrum – Constraints for ground-based faint object spectroscopy**
J. K. M. Viuho, J. P. U. Fynbo, and M. I. Andersen

Published in Astronomy & Astrophysics, 699, A241 (2025)
A draft of this manuscript has been presented on the arXiv with DOI: 10.48550/arXiv.2506.02102

Article III **KDP as a thermal blocking filter – Deep infrared observations with warm narrow band filter**
J. K. M. Viuho, A. A. Djupvik, A. N. Sørensen, D. Kumar, P. Steiner, J. P. U. Fynbo, S. Armas, and M. I. Andersen

Submitted to Publications of the Astronomical Society of the Pacific
A draft of this manuscript has been presented on the arXiv with DOI: 10.48550/arXiv.2511.11806

Article IV **On the airglow continuum – Non-scattered light biased measurement in the range 5500–11 000Å**
J. K. M. Viuho, J. P. U. Fynbo, and M. I. Andersen

In preparation

Article I

Measuring the Near-IR Airglow Continuum with Stray Light Reduced Spectrograph

J. K. M. Viuho, M. I. Andersen and J. P. U. Fynbo

Proc. SPIE 12184, Ground-based and Airborne Instrumentation for Astronomy IX 2022

https://doi.org/10.1117/12.2630668

Measuring the Near-IR Airglow Continuum with Stray Light Reduced Spectrograph

Joonas K. M. Viuho[1,2], Michael I. Andersen[1,2], and Johan P. U. Fynbo[1,2]

[1]The Cosmic Dawn Center (DAWN)
[2]Niels Bohr Institute, University of Copenhagen, Jagtvej 128, 2200 Copenhagen N, Denmark

ABSTRACT

We present an experimental spectrograph based on a new type of a white pupil echelle spectrograph designed for interline sky continuum measurement. This is an application which requires extremely low instrumental scattered light background and high spectral fidelity due to the faintness of the signal and the fact that the night sky is illuminated by bright hydroxyl emission lines from the red-end of visual spectrum through near infrared wavelengths. The conceptual design is a white pupil echelle spectrograph using a single grating in double pass. The xy-plane of the optical beam is rotated between the two consecutive dispersions thus redirecting the scattered 'grating grass' light from the grating to different direction respective to the spectrum. A mask in the secondary focus prevents this scattered light reaching the camera. The beam rotation is achieved with a normal right-angle prism allowing us to use off-the-shelf optical components and classical geometrical optics to mitigate the issue of hydroxyl airglow emission lines.

Keywords: Airglow, airglow continuum, near infrared, spectroscopy, echelle, spectral purity, atmospheric emission

1. INTRODUCTION

The airglow continuum in the near infrared is challenging to measure due to its faintness and the fact that the night sky spectrum is populated by a large number of bright hydroxyl (OH) emission lines. Under dark Moon conditions, the line emission from OH lines can be orders of magnitude brighter than the brightest continuum emission components, the airglow continuum and the zodiacal light. OH line emission and the airglow continuum vary with a large range of timescales from minutes to decades[1] making consistent measurement even more challenging.

Typically, the airglow continuum measurements have been carried out either with grating spectrographs or narrow band filters. The difficulty with narrow band filters is to find a band that is clear of atmospheric emission lines so resolving the emission is important. However, grating spectrographs are known to suffer from scattered light produced by the grating itself.[2] The grating scattered light is especially a problem for near infrared observation due to the bright OH emission lines. The broad wings of the spectrograph line spread function (LSF) can result in a significant artificial continuum burying the "true" continuum underneath it.[3,4]

The theory of airglow continuum is still not fully understood even though several contributing mechanisms are known, and consequently, the latest state-of-the-art airglow continuum models are semi-empirical.[1] The input data used for the models can be biased towards higher continuum values due to the grating scattered light and a higher spectral purity measurement would allow better understanding of the level and behaviour of the airglow continuum. Understanding the airglow continuum should be of prime interest at the dawn of ground based observation with Extremely Large Telescopes (ELTs) since its value will set the limits for ELT spectroscopic observation.

Here a new type of stray light reducing double pass echelle spectrograph design is presented with the main purpose to overcome the grating scattered light issue. The spectrograph will be used to measure the airglow continuum in the course of the coming year. The built concept design is based on an idea that has been originally

Correspondence to
E-mail: joonas.viuho@nbi.ku.dk

proposed as a design improvement for the ESO/VLT first generation high resolution spectrograph.[5] Essentially, it is a textbook example of a white-pupil echelle spectrograph with a "twist". The design uses a grating in double pass, dispersing the light along two different axes, practically, redirecting the grating scattered light away from the trace of the spectrum. The main limitation of the built prototype is that it utilises a CCD as a detector and thus has a spectral cutoff at 1100 Å. The new design should bring the most benefits in J and H bands where the atmospheric OH lines are the brightest and most abundant.

2. SCIENCE GOAL AND DESIGN DRIVERS

The purpose of this project is to measure the airglow continuum detectable by a silicon detector and demonstrate the performance of a new echelle design. Ideally, the experiment would be repeated with similar type of instrument in J and H bands. Four key design drivers are identified.

Resolution

The resolution should be high enough to allow finding OH line free spectral regions between the OH lines. Taking the Ref. 3 OH doublet separation distribution peaking between 0.1 Å– 0.2 Å, a resolution of $R \sim$12 000 is chosen which allows resolving all but the closest OH doublets.

Stray light reduction

The scattered light reduction scheme originally described in Ref. 5 is implemented for the first time. The design requires an intermediate focus in which the scattered light is masked before cross dispersion. Two different gratings were purchased and tested for the project, the better performing one is used for the measurement. The spectrograph housing is sectioned into compartments to limit off-axis light reaching the detector.

Wavelength coverage and cross dispersion

The upper limit for the wavelength coverage is set by the detection cutoff of a CCD at 11000 Å. The lower limit is set by the CCD area since the grating scattered light reduction scheme requires large order separation. An order separation of 50 pixels is needed to separate the secondary slit (the decker) at the final focal plane. Too small order spacing would lead to order cross-talk since the scattered light is redirected diagonally respective to the trace, see Fig. 2 for point spread function (PSF).

Detectable flux level

In principle, the continuum level could be as low as the zodiacal light level, which is about 50 ph/s/m^2/μm/arcsec^2 towards the ecliptic North pole,[6] which is estimated to give about 0.2ph/px in a 10min exposure, which should be suitable for photon counting.

3. INSTRUMENT DESIGN

3.1 Optical Design

SKy Is The Limit Echelle Spectrograph (SKITLES) is a traditional white pupil echelle with a 'twist'. The layout with two equal focal length collimator mirrors is familiar from many astronomical high-resolution spectrographs (See Fig. 1). The extra introduced to the traditional design is a double pass scheme of the grating originally described in Ref. 5. Between the two consecutive dispersions on the grating, the xy-plane of the optical beam is rotated using a right-angle prism (see Fig. 3). Because of the beam rotation in the grating scattered light reduction scheme, a circularly symmetric aperture was considered to be the most practical and a steel pinhole was chosen as an aperture.

The optical layout is dictated by the budget of the project. The double pass use of the grating is due to the fact that the grating is 1/6th of the total budget of the project. Using single grating in double pass forces one to bring the secondary focus in the very same location as the spectrograph entrance. In the case of SKITLES, the beam is folded in terms of a 3mm high prism right after the entrance pinhole. The folding mini prism baffle and pedestal give the characteristic look of the 2D spectrum where the central wavelengths are shadowed (see Fig. 2). This is a drawback of the presented design. However, using two separate dispersion elements would offer different packaging options.

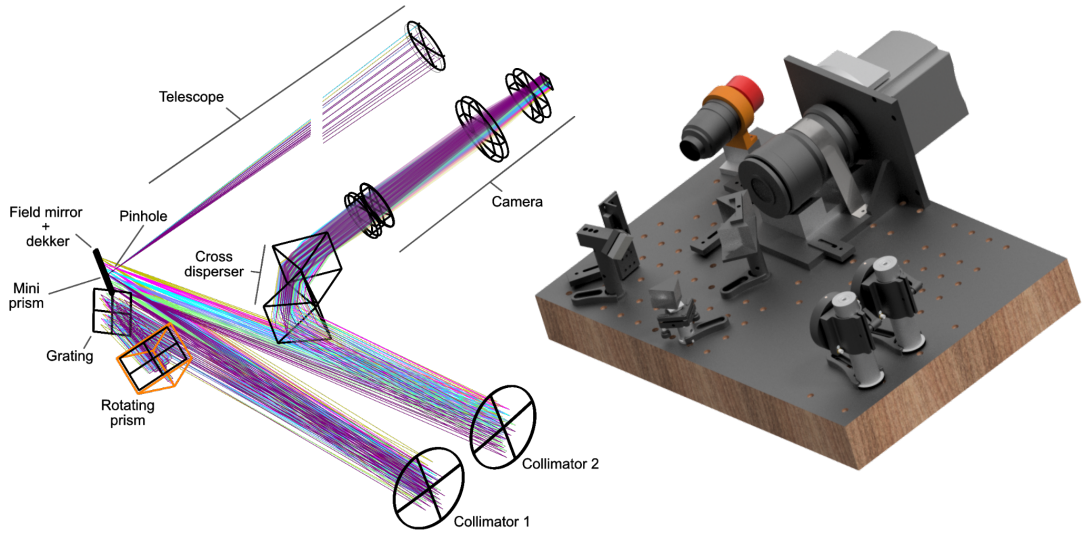

Figure 1. Side-by-side illustration of the optical and mechanical layout. The beam is tilted 90° with micro prism right after the entrance pinhole. Note the entrance prims in front of the folding mirror in the optical layout that shades the central wavelengths of each order (see Fig. 2. The dimensions of the optical table are 720mm x 480mm

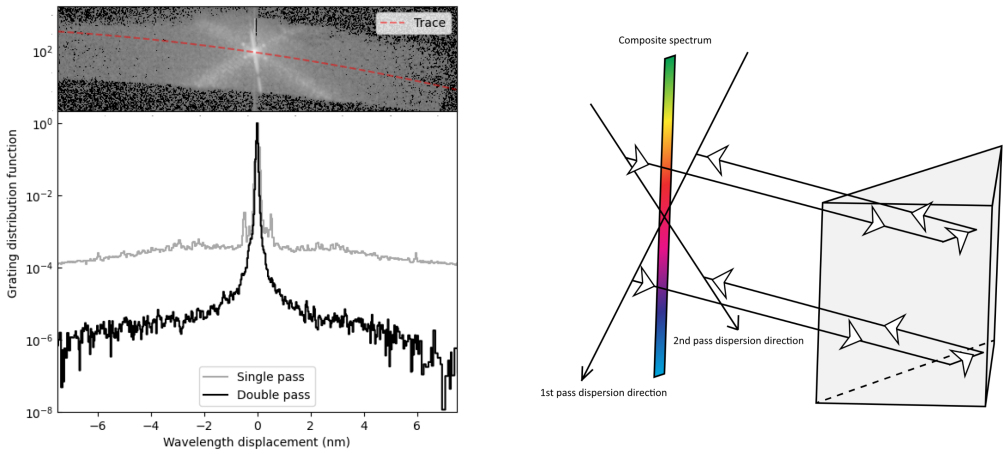

Figure 2. (Left panel) The spectrograph point spread function (PSF) on the top and line spread function (LSF) measured with HeNe laser (632.8nm)on the bottom. The LSF has a high contrast of 6 orders of magnitude between the core and the wings. (Right panel) A schematic illustrating the beam rotation scheme. The beam is dispersed twice along two different axes causing the scattered light to follow different axis than the trace (see PSF on the left panel).

3.1.1 Fore optics

SKITLES has a built-in 50mm diameter f=750mm telescope fixed on its optical table. Adding a fixed telescope on the optical bench simplifies the overall optical design. An auxiliary system is required to help with the pointing on the sky and the setup is accompanied with a siderostat. Tracking requirements for the experiment are relatively relaxed and the siderostat will consist of an astro-hobbyist star tracker and a silver mirror. A mirror with a circular hole is placed in the telescope focus allowing an auxiliary guide camera system to monitor the pinhole position on the sky.

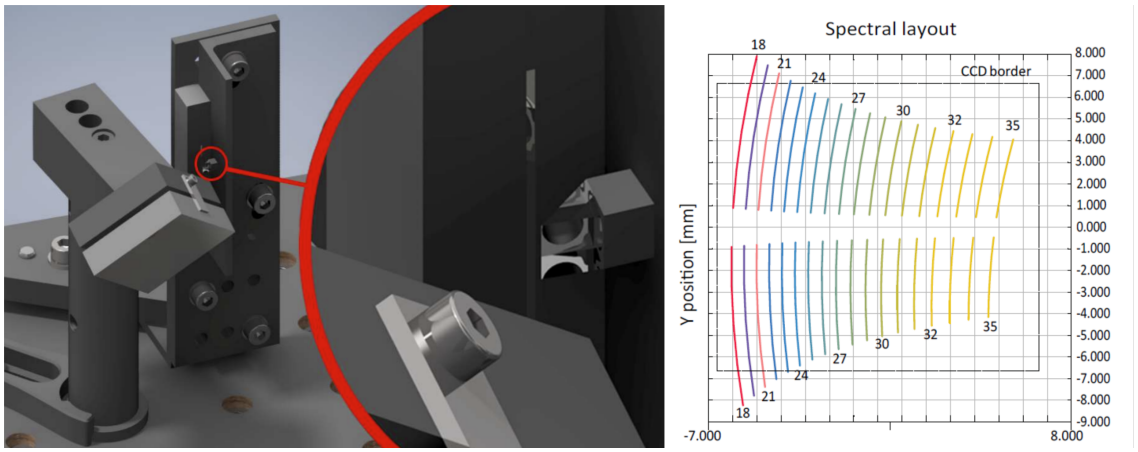

Figure 3. (Left panel) Close-up of the secondary focus with a mini prism which folds the beam into the spectrograph. (Right panel) Spectral layout illustrating the shadow cast by the mini prism located right in front of the secondary focus, a drawback of the design.

Table 1. SKITLES spectrograph key characteristics.

Wavelength coverage	550 - 1100nm
Resolving power	12 000
Groove frequency	45g/mm
Blaze angle	26.7°
Operating orders	18-34
Pinhole size	75μm, 20”
Beam diameter	34mm
Collimator focal lenght	500mm
Camera focal lenght	154mm
Camera focal ratio	f/4.4

3.1.2 Collimators

The collimator mirrors are spherical silver coated commercial-of-the-shelf mirrors.

3.1.3 Grating

Two different gratings were ordered for the spectrograph and they were characterized. The grating with the better performance, in terms of scattered light, was chosen. This grating is a 40x40mm ruled diffraction grating from Newport/Richardson Grating Lab. It has 45g/mm and a blaze angle of 26.7°.

3.1.4 Rotating prism

The rotating prism is a 40mm N-BK7. The rotating prism is in close proximity of the main beam and the unused footprint has been cut off. The beam rotation is illustrated in Fig.3. The collimated beam passes the grating twice and it is rotated between the two dispersions. The scattered light will leave to different directions than the dispersed spectrum which is a vector sum of the individual dispersions. The scattered light from the grating follows the single dispersion directions whereas the twice dispersed beam will follow third direction being the vector sum of the two individual dispersions. With a 90° beam rotation the scattered light will fall 45° from the spectrum. The scattered light can be masked out in intermediate focus.

3.1.5 Cross disperser

In order to prevent the scattered light images of the secondary slit overlapping, and create entirely dark patches between the secondary slit images for diffuse scattered light analysis, an order separation of 40-60pixels is needed. This is achieved with two 50mm F2 equilateral prisms. F2 provides high transmission over the covered wavelength range.

3.1.6 Camera

The camera is a relatively old spectrograph camera, which is recycled in this experiment. It has five lenses organized in three air spaced groups. The first group consist of a cemented triplet of UBK7 sandwiched between FK54. The triplet has residual spherical aberration which is corrected for with the bi-concave UBK7 forming the second group. The image formed by the first two groups is reasonably well corrected apart from the lateral color and field curvature. These groups are enclosed inside a common barrel which is a decommissioned camera of the Alhambra Faint Object Spectrograph and Camera (ALFOSC) at the Nordic Optical Telescope (NOT). The last group is a field flattener which is a COTS plano-convex lens from Thorlabs. The field flattener provides sub-optimal performance since it needs to be placed afar from the detector surface due to the long flange distance of the CCD. Despite this shortcoming the system offers reasonable spot quality (see Fig. 4).

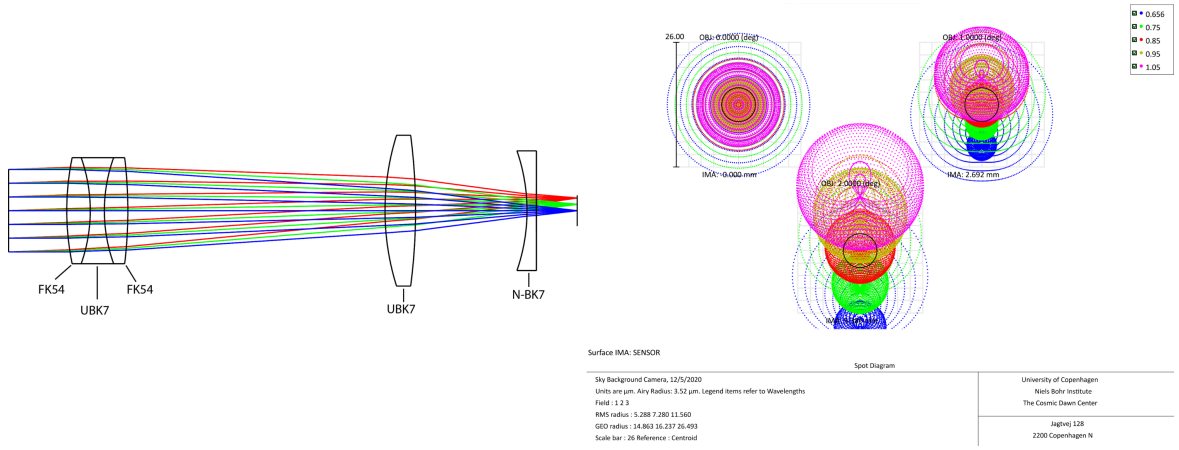

Figure 4. Camera optical layout and spot diagram. Two first lens groups are enclosed in common barrel that is recycled from another instrument project. Vacuum windows of the commercial camera system forces a long flange distance and sub-optimal but acceptable image quality.

3.2 Detector

SKITLES uses an older generation Andor DU-888 iXon -Electron Multiplication CCD (EMCCD) as its detector. An EMCCD was chosen due to it statistical photon counting capability which is required to reach the low detection levels needed for measuring the airglow continuum. Photon detections are done by calculating a threshold level above which pixels are interpreted to have receive one or more photons. The rate parameter is derived from a series of exposures by means of dead time correction in which count rate of no-detections are counted. A detailed description of the applied photon counting scheme and associated statistics are described in Ref. 7.

False positive detection rate of this method depends on the read noise of the detector and the false rate positive on the gain. The best threshold level With the optimized camera parameters leads to 3% false negative and false positive rates. The Clock-Induced Charge (CIC) of the older EMCCD is higher than its more modern counterparts and it is measured to be 1.4%, which is 10 times more than what could be reached with a more modern controller.[8] The CIC will appear as a constant background which can be subtracted with the dark current.

The effect of dark current needs to be taken into account in the experiment. EMCCDs can not be operated at as low temperature as conventional CCDs since the charge transfer efficiency (CTE) of the EM register degrades as the temperature is lowered and the optimal operating point is a compromise between the dark current and CTE.[9]

4. DISCUSSION

A stray light reducing high resolution spectrograph design has been presented and its potential for improving spectral fidelity has been demonstrated. The design relies only on classical geometrical optics making it easy to implement in an astronomical high resolution spectrograph. The design has the potential to limit the affected spectral range contaminated by the scattering wings of bright atmospheric OH lines. This should be of interest when regarding the future ELT spectrograph designs which will be sky noise dominated. The presented stray light reduction scheme can be combined with a OH line suppression techniques to improve the performance even further and different methods have been demonstrated in the literature. During the past decade, there has been lot of development on Fiber Bragg Gratings (FBGs) and their use has been already demonstrated in astronomical instruments.[10]

Due to the PSF geometry, it makes most sense to implement the presented stray light reduction scheme around a circularly symmetric aperture. Typically astronomical high-resolution spectrographs are fiber-fed so this is not a significant limitation. The drawback of the design is the extra light losses introduced by the second dispersion and beam rotation. Typical peak efficiencies of ruled gratings are around 70% and the additional dispersion has a significant penalty on the total efficiency. Nevertheless, the penalty imposed by the double dispersion scheme might be a trade-off worth accepting if the observing time lost due to lower efficiency can be gained on the sky thanks to improved spectral purity and less significant OH line scattered light contribution. The actual gain depends on the airglow continuum level but the improvement could be significant especially in H band where the OH lines are extremely bright.

We will address the question of the level of the airglow continuum with SKITLES spectrograph and an observing campaign is planned on the site Roque de los Muchachos on La Palma, Canary Islands later this year. The airglow continuum can be measured up till 10 000Å and an upper limit will be derived until 11 000Å. We will not be able to address the level of the airglow continuum in J and H bands with these measurements, but we will constrain the profile of the continuum emission and possibly giving an indication what to expect also at the longer wavelengths. Hopefully, similar observation can be carried out in J and H band in the near future.

ACKNOWLEDGMENTS

The Cosmic Dawn Center (DAWN) is funded by the Danish National Research Foundation under grant No. 140. Support for purchasing optical and opto-mechanical components from the Dr. N.P. Wieth-Knudsens Observatorium Fund is gratefully acknowledged. Special thanks for Niels Michaelsen for manufacturing custom aluminum parts, and Akke Viitanen and Nicholas Janssen for their significant contribution to the camera control software user interface.

REFERENCES

[1] Noll, S., Kausch, W., Barden, M., Jones, A. M., Szyszka, C., Kimeswenger, S., and Vinther, J., "An atmospheric radiation model for cerro paranal," *Astronomy & Astrophysics* **543** (2012).

[2] Woods, T. N., Wrigley, R. T., Rottman, G. J., and Haring, R. E., "Scattered-light properties of diffraction gratings," *Applied Optics* **33**(19), 4273–4285 (1994).

[3] Ellis, S. C. and Bland-Hawthorn, J., "The case for oh suppression at near-infrared wavelengths," *Monthly Notices of the Royal Astronomical Society* **386**(1), 47–64 (2008).

[4] Sullivan, P. W. and Simcoe, R. A., "A calibrated measurement of the near-ir continuum sky brightness using magellan/fire," *Publications of the Astronomical Society of the Pacific* **124**(922), 1336 (2012).

[5] Andersen, M. I. and Andersen, J., "Possible design features of an ultraviolet - near infrared vlt high-resolution spectrograph," in [*ESO Workshop on High Resolution Spectroscopy with the VLT*], **40**, 235–238, European Southern Observatory (1992).

[6] Tsumura, K., Battle, J., Bock, J., Cooray, A., Hristov, V., Keating, B., Lee, D. H., Levenson, L. R., Mason, P., Matsumoto, T., Matsuura, S., Nam, U. W., Renbarger, T., Sullivan, I., Suzuki, K., Wada, T., and Zemcov, M., "Observations of the near-infrared spectrum of the zodiacal light with ciber," *The Astrophysical Journal* **719**(1), 394–402 (2010).

[7] Harpsøe, K. B. W., Andersen, M. I., and Kjægaard, P., "Bayesian photon counting with electron-multiplying charge coupled devices (emccds)," *Astronomy and Astrophysics* **537**, A50 (2012).

[8] Daigle, O., Dorn, D. A., Quirion, P.-O., and Lessard, S., "The darkest emccd ever," in [*High Energy, Optical, and Infrared Detectors for Astronomy IV*], **7742**, 774203–7742011, SPIE (2010).

[9] Daigle, O., Carignan, C., Gach, J.-L., Guillaume, C., Lessard, S., Fortin, C.-A., and Blais-Ouellette, S., "Extreme faint flux imaging with an emccd," *Publications of the Astronomical Society of the Pacific* **121**(882), 866 (2009).

[10] Ellis, S. C., Bland-Hawthorn, J., Lawrence, J. S., Horton, A. J., Content, R., Roth, M. M., Pai, N., Zhelem, R., Case, S., Hernandez, E., Leon-Saval, S. G., Haynes, R., Min, S. S., Giannone, D., Madhav, K., Rahman, A., Betters, C., Haynes, D., Couch, W., Kewley, L. J., McDermid, R., Spitler, L., Sharp, R. G., and Veilleux, S., "First demonstration of oh suppression in a high-efficiency near-infrared spectrograph," *Monthly Notices of the Royal Astronomical Society* **492**(2), 2796–2806 (2020).

Article II

The near infrared airglow continuum conundrum – Constraints for ground-based faint object spectroscopy

J. K. M. Viuho, J. P. U. Fynbo, and M. I. Andersen

Published in Astronomy & Astrophysics, 699, A241 (2025)

https://doi.org/10.1051/0004-6361/202553726

arXiv preprint 2506.02102 [astro-ph.IM]

https://doi.org/10.48550/arXiv.2506.02102

A&A, 699, A241 (2025)
https://doi.org/10.1051/0004-6361/202553726

Astronomy & Astrophysics

The near-infrared airglow continuum conundrum

Constraints for ground-based faint object spectroscopy

J. K. M. Viuho[1,2,3,4,⋆], J. P. U. Fynbo[1,2], and M. I. Andersen[1,2]

[1] Cosmic Dawn Center (DAWN), Denmark
[2] Niels Bohr Institute, University of Copenhagen, Jagtvej 155A, 2200 Copenhagen N, Denmark
[3] Nordic Optical Telescope, Rambla José Ana Fernández Pérez 7, 38711 Breña Baja, Spain
[4] Department of Physics and Astronomy, Aarhus University, Munkegade 120, 8000 Aarhus C, Denmark

Received 10 January 2025 / Accepted 31 May 2025

ABSTRACT

Context. The airglow continuum in the near-infrared is challenging to quantify due to its faintness and the grating-scattered light from atmospheric hydroxyl (OH) emission lines. Despite its faintness, the airglow continuum sets fundamental limits for ground-based spectroscopy of faint targets and accounts for the difference between ground- and space-based observations in the interline regions between atmospheric emission lines.

Aims. We aim to quantify the level of airglow continuum radiance in the visible- to near-infrared wavelength range observable with silicon photodetectors at the Observatorio del Roque de los Muchachos, in such a way that our measurement is not biased by the grating-scattered light. We aim to do this by measuring the airglow continuum radiance with minimal and controlled contamination from the broad instrumental scattering wings caused by the bright atmospheric OH lines.

Methods. We measured the airglow continuum radiance using a long-slit $\lambda/\Delta\lambda \sim 4000$ spectrograph in ∼100 Å-wide narrow bandpasses centered at 6720, 7700, 8700, and 10 500 Å (corresponding to the R, I, and Z broadbands) with the 2.5-meter Nordic Optical Telescope under photometric dark-sky conditions. The bandpasses were chosen to be as free as possible from atmospheric absorption and OH line emission, thereby minimizing the radiation reaching the grating surface.

Results. We observe the zenith-equivalent airglow continuum to be 22.5 mag arcsec^{-2} at 6720 Å and 22 mag arcsec^{-2} at 8700 Å. We derive upper limits of 22 mag arcsec^{-2} at 7700 Å, due to difficulties in finding a clean part of the spectrum for measurement, and 20.8 mag arcsec^{-2} at 10 500 Å, due to low system sensitivity. Within measurement errors and the natural variability expected for airglow emission, our results for the Observatorio del Roque de los Muchachos are comparable to the values reported for other major observatory sites. With our medium-resolution spectra, we are unable to comment on the origin of the radiance, which could still be due to faint unresolved spectral lines or the true (pseudo)continuum. The measurement uncertainty on the zenith-scaled continuum radiance is dominated by detector effects, assumptions on atmospheric scattering, and the choice of zodiacal light model.

Conclusions. We conclude that the airglow continuum radiance is not due to instrumental effects in our bandpasses and measure it to be two to four times brighter than the zodiacal light toward the ecliptic poles, the darkest foreground available for both ground- and space-based observatories. While the level is not negligible, it is dark enough to encourage further investigations into novel optical technologies and apply known stray light reduction techniques to future near-infrared and short-wave infrared spectroscopic instrumentation.

Key words. atmospheric effects – instrumentation: spectrographs – methods: observational – infrared: diffuse background

1. Introduction

Astronomy has entered the photon noise-limited era, driven by even lower-noise photodetectors and larger aperture telescopes, as highlighted by the forthcoming extremely large telescopes (ELTs). Both ground- and space-based observatories are affected by the zodiacal light (ZL), while ground-based facilities experience additional emission from the foreground sky, the continuum radiance of which is still not well understood. To set a reference for the foreground brightness, the darkest VIS–NIR[1] foreground available from both ground and space is toward the ecliptic poles, making them ideal zones for deep fields such as the Hubble deep field (HDF; Williams et al. 1996) and the Great Observatories Origins Deep Survey (GOODS; Giavalisco et al. 2004) fields. The yearly average ZL foreground in HDF is ∼50 ph s^{-1}m^{-2}μm^{-1}arcsec^{-2} at 1.25 μm, corresponding to 22.4 mag arcsec^{-2}. Similarly, the cosmic evolution survey (COSMOS; Scoville et al. 2007; Weaver et al. 2022) field, located at a lower ecliptic latitude, $\beta_{ec} = -9°$, offers a background of ∼85 ph s^{-1}m^{-2}μm^{-1}arcsec^{-2} or 21.8 mag arcsec^{-2} for the darkest part of the year but undergoes large variation depending on the Solar elongation angle. Ground-based astronomical observatories are located at some of the darkest sites around the globe, with typical broadband sky brightness ranging in the visual (VIS) V ∼ 22 mag arcsec^{-2}, but rapidly increasing toward longer wavelengths, reaching I ∼ 20 mag arcsec^{-2} in NIR, and J ∼ 16 mag arcsec^{-2}, H ∼ 14 mag arcsec^{-2} in SWIR. The reason for the increase is the radiance from the increasing number density and brightness of rotation-vibrational transitions of hydroxyl

⋆ Corresponding author: joonas.viuho@nbi.ku.dk

[1] We define the spectral ranges referred to often in the following way: visible 4000–7000 Å (VIS), near-infrared (NIR) 7000–11 000 Å, and short-wave infrared (SWIR) 1.1–3 μm. All magnitudes in our work refer to those in the AB system.

(OH) molecules, and to a lesser extent molecular oxygen O_2. The behavior of atmospheric line emission is understood to a level where sophisticated models have been developed (e.g., ESO SkyCalc, Noll et al. 2012; Jones et al. 2013). However, the interline airglow continuum emission, especially in NIR–SWIR wavelengths, remains much less well known due to its faintness and the challenges of its measurement. Instrumental effects, such as grating-scattered light and thermal stray light, complicate the airglow continuum measurement if the experiment is not carefully designed.

Published, dedicated airglow continuum radiance measurements at VIS and NIR wavelengths are mainly from the 1960s and 1970s (Krassovsky et al. 1962; Broadfoot & Kendall 1968; Sternberg & Ingham 1972; Gadsden & Marovich 1973; Noxon 1978; Sobolev 1978). Since then, the VIS and NIR continuum radiance has been studied at Cerro Paranal, Chile (Hanuschik 2003; Patat 2008; Noll et al. 2024). After the introduction of SWIR mercury-cadmium-telluride detectors, the interest in airglow continuum radiance shifted mostly to SWIR (Maihara et al. 1993b; Cuby et al. 2000; Ellis et al. 2012; Sullivan & Simcoe 2012; Trinh et al. 2013; Oliva et al. 2015; Nguyen et al. 2016), where the ZL foreground is significantly lower than in NIR (Leinert et al. 1998; Windhorst et al. 2022). Special attention has been given to a relatively narrow spectral region in the H band located around 16 650 Å, originally selected by Maihara et al. (1993b), despite later studies finding few emission lines in this region (Oliva et al. 2015). We summarize previous airglow continuum measurements found in the literature in Table B.1.

Both spectroscopic and narrow-band imaging measurements have been done to determine the airglow continuum radiance in the NIR and SWIR range. Both methods have their advantages and disadvantages: it is difficult to find a clean spectral bandpass without airglow emission lines for narrow-band imaging, and grating spectrographs are susceptible to suffering from grating-scattered light, which can appear as dislocated copies of a parent line and broad diffuse line wings (Woods et al. 1994; Koch et al. 2021). In NIR and SWIR wavelengths, the scattered light combined from all airglow emission lines can result in an artificial continuum (Ellis & Bland-Hawthorn 2008; Sullivan & Simcoe 2012; Oliva et al. 2015). Sullivan & Simcoe (2012) concluded that their continuum measurement in the H band could be explained by the spectrograph's line spread function (LSF) wings, while shorter wavelength bands remain unaffected. Thermal blackbody radiation from the instrument may additionally affect the measurement (Ellis et al. 2020). To minimize the effect of grating-scattered light, a number of spectroscopic measurements in the 1–2 µm range have been accompanied by OH line emission suppression units (e.g., Maihara et al. 1993a; Ellis et al. 2012).

A further complication is that airglow exhibits significant temporal variation, with timescales ranging from minutes (due to mesospheric buoyancy waves) (Smith et al. 2006; Moreels et al. 2008), to years (Solar cycle) (Leinert et al. 1995; Mattila et al. 1996; Krisciunas 1997; Patat 2008; Noll et al. 2017). Additionally, semiannual (Grygalashvyly et al. 2021) and diurnal variability (Smith 2012) of the line emission is present. The airglow continuum has been observed to exhibit diurnal variability (Trinh et al. 2013). The NIR and SWIR OH and O_2 line emissions are known to originate from the mesopause region (e.g., Baker & Stair 1988). There is a strong density change in the mesopause, and waves can travel at the boundary layer. Typically, these gravity or buoyancy waves can be observed with a ∼15% brightness variation on timescales from a few up to tens of minutes (Moreels et al. 2008). However, mesospheric bore events can drive solitons, which may cause sudden, localized, large-amplitude changes (e.g., Smith et al. 2006).

Despite the challenges in measurement, a number of chemiluminescent processes are known to contribute to the atmospheric continuum radiance. Several nitrogen monoxide (NO) reactions are known to contribute to the total VIS–NIR continuum (see Bates 1993; Khomich et al. 2008; Noll et al. 2024, and references therein for extended discussion). However, none of the reactions have a rate that is sufficiently high to explain the total continuum radiance that has been observed. Recently, it has been shown that iron monoxide (FeO) has an extended pseudo-continuum emission spectrum extending from VIS to SWIR, with the potential to explain a significant fraction of the VIS–NIR continuum emission (Noll et al. 2024). FeO still leaves a significant SWIR component unattributed, which is possibly due to hydroperoxyl HO_2 (preprint, Noll et al. 2025).

The objective of this study is to measure the airglow continuum with a method that strongly reduces the effect of grating-scattered light. Our study is limited to the spectral range observable with a Charge-Coupled Device (CCD), i.e., below about 11 000 Å. The airglow spectra were observed through narrow band (NB) filters, which is not a full-fledged OH suppression scheme but allows for the selection of bandpasses such that the number and brightness of unwanted OH line emissions are kept to a minimum. Data recording is described in detail in Sect. 2. Due to the faint signal level, additional efforts were spent on reducing the data, which is discussed in Sect. 3. We compensated for the low sensitivity close to the detector sensitivity limit by observing thicker air columns, i.e., fields at very large zenith distances. The assumptions underlying our final results are discussed in the analysis Sect. 4. Lastly, the implications of our results are discussed in Sect. 5 and 6. Observed apparent airglow spectra are included in Appendix A. References to previous similar studies found in the literature are gathered in Appendix B, and their results are converted to the units used in this work to allow for comparison.

2. Observations and data

2.1. Site

We recorded airglow continuum spectra with the ALFOSC instrument mounted on the 2.56-meter Nordic Optical Telescope (NOT). The NOT is located at the Observatorio del Roque de los Muchachos on La Palma, Canary Islands, Spain, with the geographical coordinates +28 °45′26.2″ N and 17°53′06.3″ W, and an altitude of 2382 meters. The NOT has a lower pointing limit of 6° above the horizon, and its location is such that the horizon is unobstructed when observing toward the north. The northern direction has the least amount of light pollution at the site, since the line of sight travels entirely above the Atlantic, with the only source of artificial illumination being the town of Roque del Faro, located 5 km north of the Observatorio del Roque de los Muchachos. Light pollution, which is mostly caused by low-pressure sodium lamps with characteristic wavelengths of 5890 and 5896 Å, falls outside the bandpasses in our study. The next source of artificial illumination on the line of sight is the island of Madeira, which is 450 km north of La Palma.

2.2. Field selection

The observed fields on the sky were chosen to be as dark as possible outside the atmosphere, away from both the ecliptic and galactic planes, and yet close to the horizon to be able to observe

Table 1. Optical configurations used for the NB observations.

Band	$\lambda/\Delta\lambda$	Slit width	Slit length	NB filter name	FWHM	Order-sorting filter	Grism
6720 Å	9400	0.51″	5.3′	S[II] 672_5	60 Å	r Gunn 680_102	Grism #17
6720 Å	3500	1.29″	5.3′	S[II] 672_5	60 Å	r Gunn 680_10 2	Grism #17
7700 Å	4300	0.45″	2.4′	FB770-10	80 Å	i′ SDSS 771_171	Grism #9
8700 Å	4300	0.45″	2.4′	FB870-10	120 Å	z′ SDSS 832_LP	Grism #9
10 500 Å	4300	0.45″	2.4′	FB1050-10	100 Å	z′ SDSS 832_LP	Grism #9

Notes. Component names refer to NOT's optical component database names. The pixel scale is ~0.2138 arcsec px^{-1}.

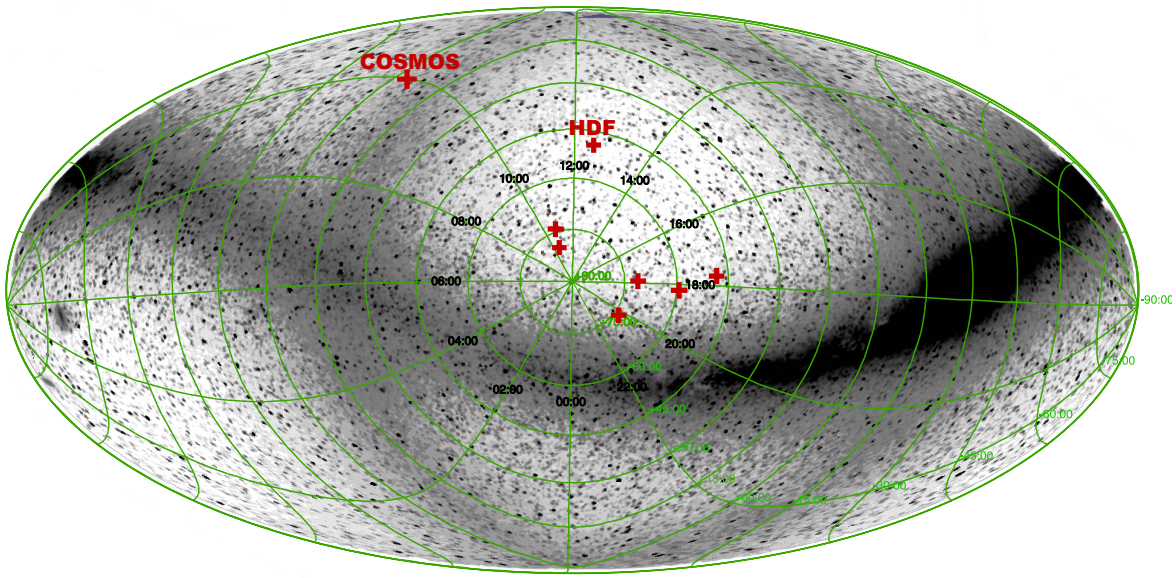

Fig. 1. Projection of the COBE/DIRBE band 1 map with a central wavelength at 1.25 µm toward the ecliptic north pole. The red markers indicate the coordinates for our pointings, the HDF, and the COSMOS field. The Milky Way crosses the map horizontally, while ZL in the ecliptic plane appears as a ring between declinations $\delta = [-30, 30]$.

it with a thick air column. The COBE Diffuse Infrared Background Experiment (DIRBE) (Hauser et al. 1998; Arendt et al. 1998; Kelsall et al. 1998; Dwek et al. 1998) band 1 maps, with a central wavelength of 1.25 µm, were first used to locate fields with low surface brightness (Fig. 1). PanSTARRS DR1 z-band images (Flewelling et al. 2020) were then used to fine-tune the location to areas with the fewest visible sources and to assist in orienting the slit on the sky. To summarize, the coordinates for the pointings were chosen with the following selection criteria:

- Ecliptic latitude $\beta_{\rm ec} > 50°$;
- DIRBE band 1 radiance < 85 ph s^{-1}m^{-2}µm^{-1}arcsec^{-2};
- No bright, $m < 12$ mag, stars in the 6.5′×6.5′ALFOSC field of view;
- No sources visible in the slit area in the PanSTARRS z-band image;
- Observable with a zenith distance $z > 75°$ toward the north; and
- Only a few degrees variation in zenith distance during the measurement.

Additionally, the following time restrictions were adopted:

- Moon altitude <−30°,
- Moon separation >60°,

to ensure no scattered moonlight was observed (Krisciunas & Schaefer 1991; Jones et al. 2013). Typically, the Moon illumination fraction during our observations was <2%. Additionally, the first observing run was purposefully scheduled to coincide with the December solstice to provide the longest possible night. Observations typically occurred several hours after sunset, and in most cases past the local midnight.

2.3. Optical setup

The optical setups that were used are summarized in Table 1, with optical component names referring to the NOT's optical element database. Four NB filters were purchased for the experiment, with spectral bandpasses chosen such that they would mostly be free from bright (OH) lines and atmospheric molecular absorption. The chosen bands were centered at 6720, 7700, 8700, and 10 500 Å (see Fig. 2). The bandpasses were generally clean of strong absorption, apart from the 7700 Å band, which has significant O_2 absorption on the blue side of the bandpass. The bandpasses were 60–120 Å in width, limiting the total OH line flux reaching the grism to its minimum. All bright OH lines within the bandpasses were located in the wings of the NB filter transmission profiles. The NB filters were positioned in the beam before the grisms in the optical path; thus the stray light introduced by the OH lines were kept to a minimum.

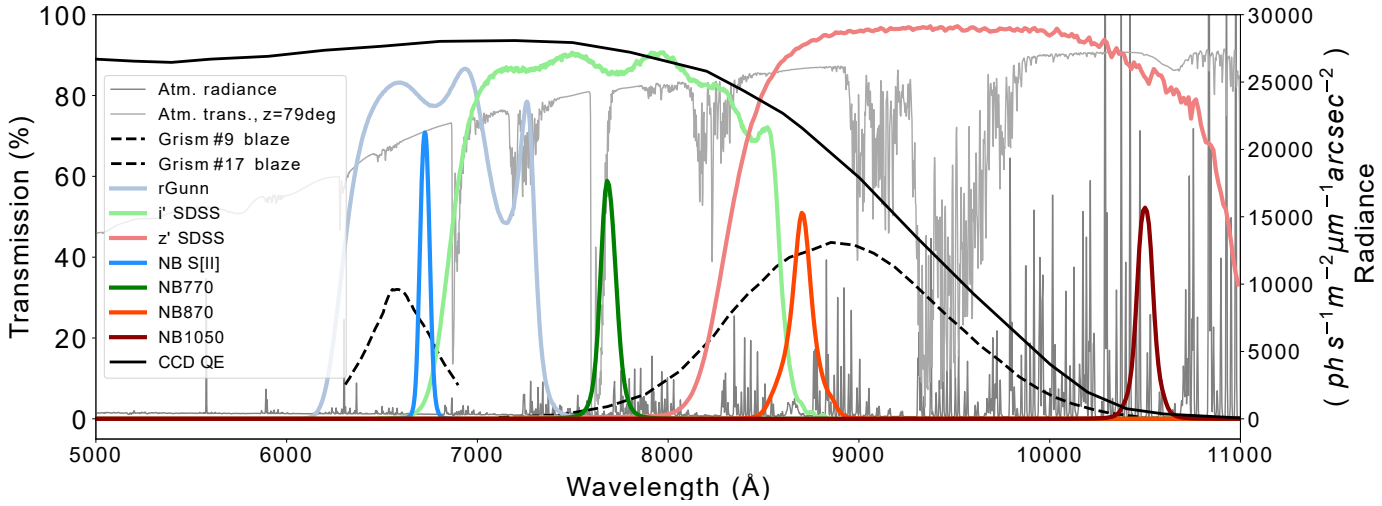

Fig. 2. Transmission curves of the NB filters, order-sorting broad-band filters, grism blaze functions, detector efficiency, and atmospheric transmission at the observed zenith distance. The blue half of the 7700 Å band is strongly absorbed by atmospheric O_2. In the 10 500 Å band, the total system efficiency is very low, as the wavelength falls within the wing of the grism blaze function.

The three redder NB filters had a diameter of 25.4 mm, which would significantly vignette the ALFOSC beam if placed in standard filter mounting slots, and were consequently mounted on the slit wheel instead. This reduced the effective slit length to 2.4′, allowing a sampling of 675 px on the detector with the reduced slit length. The vertical slits for the 6720 Å band were 5.3′in length, allowing a sampling of 1500 px. In the three reddest bands, the echelle grism #9 was used as the dispersive element, since it had the highest resolution of the available grisms, $\lambda/\Delta\lambda \approx 4300$, with a spectral coverage up to the CCD sensitivity cutoff at 11 000 Å. The broadband SDSS i′ and z′ -filters were used for order sorting with grism #9. The 6720 Å band was observed with grism #17 using the Gunn r-band filter for order sorting. Using the order sorter was probably unnecessary with grism #17, but was done as a precaution.

The 2D spectrum was binned along the slit dimension before the readout and later during the analysis, and the entire remaining slit length was median-collapsed into 1D. This process has the potential to cause smearing and additional line broadening. To counter this, both the slits and the grisms were carefully aligned before the observation such that the slit and dispersion direction matched the detector pixel row and column axes to minimize smearing. Both were aligned to within less than one pixel RMS difference relative to the detector axes. Potential spread was negligible, and any possible resulting broadening was captured by the LSF model.

We checked the instrument pixel scale on a few denser standard star fields and find it to be constant over the field of view with a value of $0.21377 \pm 5 \times 10^{-5}$ arcsec px^{-1} by plate solving. Slit widths were measured by illuminating the slit with a standard calibration arc lamp, and by imaging them with the ALFOSC camera.

2.4. Line spread function

The diffraction theory predicts a Lorentzian-like envelope for the grating distribution function, which is modulated by the spectrograph camera point spread function. For a good camera optic, the point spread function is approximately Gaussian. In addition to the Lorentzian and Gaussian components, the micro-roughness of the grating surface contributes a diffuse component (Woods et al. 1994; Koch et al. 2021). To estimate the wing contribution to the measured continua, a crude estimate of the LSF was made based on Thorium-Argon arc lamp exposures, since no monochromatic light source operating within the bandpasses was available. The approach was far from optimal, due to unresolved and too faint lamp lines, but was sufficient to derive an upper limit on the grating-scattered light. A combination of Lorentzian and Gaussian functions was fit on prominent arc lines visible in the bandpasses. Grism #17 was best fit with a function that was almost completely Lorentzian, whereas grism #9 appeared mainly Gaussian, which might indicate that the acquired arc exposures of grism #9 were not deep enough to expose the Lorentzian wings. However, this would lead to fitting the wings to the readout-noise floor, thereby further overestimating the scattering-wing contribution.

Based on the fits, 95% of the line flux is within ±0.5 Å, ±1.7 Å, and ±2.1 Å from the line center in the 6720, 7700, and 8700 Å bands, respectively. Similarly, 99% of the flux is within ±0.9 Å, ±6.7 Å, and ±6.6 Å. To give a gross overestimate of the LSF wing contribution, the remaining 1% of the light further from the core can be taken as the diffuse LSF component. Dividing the 1% of the total line flux in each band and distributing it equally within the full width at half maximum (FWHM) of the NB filter, one reaches an upper limit of 4×10^{-4}, 0.2, and 0.1 e$^-$ px^{-1} in the 6720, 7700, and 8700 Å bands, respectively, which are well below the systematic uncertainty of 0.6 e$^-$ px^{-1} from bias subtraction (see Sect. 3). Consequently, we expect the OH-line wing contribution originating from the OH lines within the bandpass to the measured continuum to be negligible. Our measurement in the 10 500 Å band is detector-noise limited, and no continuum detection was achieved. Consequently, we did not study the effect of the LSF wings in this band.

2.5. Detector setup

The ALFOSC is equipped with a deep-depleted e2v CCD231-42 backside-illuminated CCD with active pixel dimensions of 2048 × 2064 px. Outside the image area, there is an additional 38 px of vertical and 2×50 px of horizontal overscan. The CCD controller has four readout amplifiers, with amplifiers B and D

Table 2. Table of observations.

ID	Band	Time	Date	Start time	t_{exp}	Time after sunset	RA	Dec	Field rotation	Mean altitude	Pressure
№	Å	MJD		UT	s	h	J2000	J2000	°	°	hPa
1	7700	59579.05704	31 Dec. 2021	01:22	900	6.80	17:52:10.6	+70:57:17.0	–12.31	10.38	772
2	8700	59579.01002	31 Dec. 2021	00:14	900	5.67	17:52:10.6	+70:57:17.0	3.58	9.71	773
3	6720	59580.04950	1 Jan. 2022	01:11	900	6.62	17:52:10.6	+70:57:17.0	–2.21	10.24	774
4	10 500	59580.02506	1 Jan. 2022	00:36	1800	6.03	17:52:10.6	+70:57:17.0	–2.22	9.86	774
5	6720	59581.05177	2 Jan. 2022	01:14	1200	6.67	17:51:51.0	+70:55:59.2	–7.46	10.42	775
6	8700	59581.03999	2 Jan. 2022	00:57	900	6.38	17:52:10.6	+70:57:17.0	–7.46	10.08	775
7	8700	59582.08453	3 Jan. 2022	02:02	900	7.45	17:52:10.6	+70:57:17.0	–23.70	11.82	775
8	10 500	60023.96559	20 Mar. 2023	23:10	1800	3.68	18:12:34.2	+59:28:00.2	90.00	10.47	773
9	10 500	60023.93552	20 Mar. 2023	22:27	1800	2.97	20:20:50.8	+73:31:06.3	90.00	12.90	773
10	7700	60024.98045	21 Mar. 2023	23:32	1800	4.03	18:12:29.9	+59:26:41.8	45.00	13.01	772
11	8700	60024.93303	21 Mar. 2023	22:24	1200	2.90	20:20:04.6	+73:31:27.3	90.01	12.68	772
12	6720	60554.95556	1 Sep. 2024	22:56	1000	3.28	10:42:41.9	+74:01:59.3	–51.10	15.04	772
13	6720	60555.03125	2 Sep. 2024	00:45	500	5.10	10:42:41.9	+74:01:59.3	–77.70	12.72	772
14	6720	60555.11736	2 Sep. 2024	02:49	500	7.17	10:42:41.9	+74:01:59.3	–107.50	14.11	771
15	8700	60554.93403	1 Sep. 2024	22:25	1000	2.77	10:42:41.9	+74:01:59.3	38.90	15.90	772
16	8700	60555.01528	2 Sep. 2024	00:22	1000	4.72	10:42:41.9	+74:01:59.3	1.60	12.87	772
17	8700	60555.07361	2 Sep. 2024	01:46	1000	6.12	10:42:41.9	+74:01:59.3	1.00	12.94	772
18	8700	60555.08819	2 Sep. 2024	02:07	1200	6.46	10:30:10.4	+79:41:05.6	0.90	18.90	771
19	8700	60555.10347	2 Sep. 2024	02:29	1000	6.83	10:42:41.9	+74:01:59.3	0.40	13.72	771

Notes. Each pointing is given an ID number to allow easier comparison between Tables 2, 3, as well as the figures in Appendix A.

showing very similar performance. For an unknown reason, the binning for amplifier D limited the usable detector area, leading us to use amplifier B for the measurement. Additionally, amplifier B was located further away from the region of interest for the three reddest bands, giving the controller more time to stabilize during a readout. Based on NOT's long-term quality control monitoring, the readout noise of amplifier B was $4.40 \pm 3 \times 10^{-2}\,e^-$ for the slowest available readout speed of 100 kHz. According to the same quality control data, the gain was $0.169 \pm 2 \times 10^{-3}\,e^-\,ADU^{-1}$. These values are adopted in our analysis. Different binning factors were studied before beginning the observations, and a binning of 5 was adopted in the slit dimension.

2.6. Atmospheric conditions

All observations were carried out under photometric conditions. The appearance of high clouds along the line of sight was monitored with all-sky cameras to ensure that a cloud layer would not interrupt our observations. Low dust particle counts, such as those caused by Calima from the Sahara (Murdin 1986), were measured at the level of the observatory during all nights. Tenerife, 130 km away, was clearly visible on all nights of observation, providing a VIS reference for atmospheric turbidity and indicating good atmospheric transparency.

The first set of observations was carried out on the nights of December 30, 2021, through January 2, 2022, and a second set of observations was performed in March 2023 (see the list of observations in Table 2). The main run took place one week after the winter December solstice, during dark-sky conditions with no Moon illumination. Observations were made between 00:00 UT and 02:00 UT at an altitude of 10° above the horizon to guarantee a thick air column and only a small amount of non-atmospheric emission. The horizon was clear during all four December nights, and observing conditions were generally excellent. Additional observations were carried out in September 2024, again under clear-sky conditions with no Moon illumination. These additional observations were carried out at smaller zenith distances to avoid the Milky Way.

2.7. Solar conditions

The data on solar and space weather conditions are presented in Table B.2 and shown in scatter plot Fig. 5. The solar 10.7 cm radio flux, or $F_{10.7}$ (Tapping 2013), data are from the automated solar radio flux monitors of the Dominion Radio Astrophysical Observatory (DRAO) in Penticton, Canada. The DRAO reports $F_{10.7}$ three times per day, and Table B.2 refers to the DRAO observed flux recorded closest to the time of our observation. The last observation of the day was recorded either at 22:00 UT (November – February) or 23:00 UT (March – October). The solar X-ray data are from the Geostationary Operational Environmental Satellite (GOES), and the solar wind data are from the Deep Space Climate Observatory (DSCOVR). Solar and space weather communities typically refer to X-ray fluxes in units of X-ray flare class. These flare classes – A, B, C, M, and X – denote 10^{-8}, 10^{-7}, 10^{-6}, 10^{-5}, and $10^{-4}\,W\,m^{-2}$ in the wavelength range of 1–8 Å, respectively. For example, B2.5 indicates $2.5 \times 10^{-7}\,W\,m^{-2}$. We use these units in this work to report solar X-ray background and solar flare strengths.

From December 31, 2021, to January 3, 2022, solar activity was generally low with an X-ray background level ranging from B2.5 at the beginning of the run to B1.5 at the end. On December 31, five C-class flares took place, and on January 1, one C-class and one M-class flare were observed. $F_{10.7}$ decreased from about 103 to 90 sfu. The solar wind speed and density varied during

the run, with both generally increasing toward the end of the run. On January 2, 2023, just after UT midnight, the solar wind speed and density showed a sudden increase, coinciding with the highest measured continuum level at 8700 Å (obs. ID 6, see Fig. A.3), and an elevated OH line emission in the 6720 Å band (obs. ID 5, see Fig. A.1). In March 2023, the $F_{10.7}$ flux was at a similar level of 90 sfu, as in the first run. However, the X-ray background was an order of magnitude higher, averaging C1. On March 20, 2023, three C-class and one M-class flare were observed. Five C-class flares were recorded on the following day, March 21, 2023. The solar wind was stable, with comparable values to the first run. The final September 2024 run coincided with higher solar activity, with $F_{10.7}$ consistently around 230 sfu and a strong X-ray background ranging between C3 and C4. On January 1, 2024, seven C-class and four M-class flares were observed – with the strongest being M5.57 –lasting for an extended period of time. The solar wind speed and density were low compared to the earlier runs.

2.8. Stellar contamination

Due to the large zenith distances of the observations and the very barren fields, it was difficult to find guide stars to correct telescope tracking. Most of the observations relied on telescope blind tracking, apart from the night of September 1, 2024, when the telescope guided on all pointings. Blind tracking accuracy for NOT is reported to be 0.17 arcsec min^{-1} at $z = 14°$ and 0.6 arcsec min^{-1} at $z = 70°$. The blind tracking error was not measured at the zenith distances of our observations, but one can assume it to be larger than the measured error at $z = 70°$. Assuming a drift of 1 arcsec min^{-1} at $z = 80°$, it would take 30 s for a star to cross the slit. This corresponds to less than 5% of the total exposure time. In the data reduction, the entire slit length was median-collapsed into 1D. In our analysis, we assume that stars potentially crossing the slit due to tracking errors do not contaminate the measured sky radiance.

2.9. Standard stars

One flux standard star observation was taken for per filter per run. Standard stars were observed at a low zenith distance with a 10″-slit, or on some occasions without a slit, to determine the system sensitivity function. During the first run over New Year's 2021–2022, the white dwarf LAWD 23 was observed in the 8700 Å band, and HD 84937 was observed in the remaining bands. During the 2023 run, HD 93521 was observed in the 7700, 8700, and 10 500 Å bands, and on September 1, 2024, HD 19445 was observed in the 6720 and 8700 Å bands. The LAWD 23 reference fluxes were taken from Oke (1974) and corrected by a zero-point offset of 0.04 mag, as suggested by Colina & Bohlin (1994). The reference fluxes for HD 84937 and HD 93521 were taken from Rubin et al. (2022). No reference fluxes were found for any of the three observed standard stars at 10 500 Å. Consequently, a spectral template of an O9 V star (Pickles 1998) was used, and its Wien tail beyond 9700 Å was scaled to match the HD 93521 flux from Rubin et al. (2022). HD 93521 has a spectral type of O9 III, and it is somewhat cooler than the spectral template used. The flux calibration in the 10 500 Å band should only be taken as indicative. The reference flux for HD 19445 was obtained from the X-shooter Spectral Library Data Release 3 (Verro et al. 2022).

3. Data reduction

The detected signal level of the continuum flux was very low, in the range of 1–3 e$^-$ px^{-1} in all three bands, where a signal was detected. For this reason, very careful bias subtraction, precise to a few tenths of e$^-$ px^{-1}, was required. Before beginning the observing campaign, we found that in a series of bias frames, the bias level exhibited random frame-to-frame mean-level fluctuations of 1–2 e$^-$. In addition to drifts, the bias level exhibited a complex structure with both low- and high-frequency random modulation, as well as a saddle-shaped settling pattern. Consequently, we could not rely on stacked master bias frames, since the systematic uncertainty would have surpassed the signal we tried to measure. Instead, the bias level was modeled based on the horizontal and vertical overscan regions. To correct for the low-frequency random modulation, a nonparametric local linear regression model was fit both row-wise and column-wise. The cross-product of the row and column models was scaled to match the mean bias level. The high-frequency random modulation was still left intact, and an additional static sinusoidal pattern was revealed. Both of these components were removed together with dark current by sampling the unilluminated areas on the detector. The adopted bias subtraction leaves a detector background that is very flat. The method was tested on a series of 120 biases. These were processed using the adopted procedure, producing a mean level of 0.0 ± 0.6 e$^-$ over the entire image area. This leaves the bias subtraction itself as the main source of uncertainty in the measurement before zenith scaling, since sampling the entire slit length brings the effective readout noise to 0.3 e$^-$ in the 6720 Å band, and 0.4 e$^-$ in the remaining bands.

Cosmic rays were then removed with a Python implementation of the L.A.Cosmic algorithm (van Dokkum 2001). The dark current was sampled from the detector area, which was unexposed to light. No flat fielding was done, as the entire slit length was collapsed into 1D and pixel-to-pixel variations averaged out. The 2D wavelength solution and rectification were performed using packages in Image Reduction and Analysis Facility (IRAF) (Tody 1986, 1993), either by using Thorium-Argon arc lamp lines (6720, 7700, and 8700 Å) or by using sky lines, if a sufficient number of arc lines was not visible in the band (10 500 Å). The sky lines were identified based on Osterbrock et al. (1996) and Rousselot et al. (2000) night-sky emission line atlases containing the brightest atmospheric emission lines. In the case of the 6720 Å band, no spectral lines were listed in the observatory lamp line maps, and the arc lamp was first observed without the NB filter to identify spectral lines within the bandpass. The newly identified lines were used to fit the 2D wavelength solution. The spectra were 2D rectified and then median-collapsed to 1D. The sensitivity functions for each band were derived from the 10″-slit, or the slitless standard star observations, and the spectra were calibrated. The sensitivity functions for each run were derived.

4. Analysis and results

4.1. Apparent continuum radiance

The apparent airglow continuum radiance was measured from regions of the spectra close to the peak transmission of the NB filter, where no sky lines were reported in the line lists of Hanuschik (2003) for the 6720, 7700, and 8700 Å bands,

Table 3. Apparent observed and inferred zenith equivalent airglow continuum radiance.

Band	ID	Total continuum *apparent observed*		Zodiacal light *Kelsall et al. (1998)*		Airglow continuum *zenith, emitted*		Airglow continuum *zenith, emitted + scattered*	
Å	№	ph s^{-1}m^{-2}µm^{-1} arcsec^{-2}	mag arcsec^{-2}	ph s^{-1}m^{-2}µm^{-1} arcsec^{-2}	mag arcsec^{-2}	ph s^{-1}m^{-2}µm^{-1} arcsec^{-2}	mag arcsec^{-2}	ph s^{-1}m^{-2}µm^{-1} arcsec^{-2}	mag arcsec^{-2}
6720	3	271 ±99	$21.20^{+0.49}_{-0.34}$	59	22.85	53 ±19	$22.97^{+0.48}_{-0.33}$	73 ±27	$22.62^{+0.50}_{-0.34}$
6720	5	255 ±75	$21.26^{+0.38}_{-0.28}$	59	22.85	48 ±14	$23.08^{+0.37}_{-0.28}$	67 ±20	$22.71^{+0.38}_{-0.28}$
6720	12	525 ±32	$20.48^{+0.07}_{-0.06}$	64	22.76	78 ±5	$22.55^{+0.07}_{-0.07}$	107 ±7	$22.20^{+0.07}_{-0.07}$
6720	13	440 ±64	$20.67^{+0.17}_{-0.15}$	64	22.76	74 ±11	$22.61^{+0.17}_{-0.15}$	102 ±15	$22.26^{+0.17}_{-0.15}$
6720	14	316 ±64	$21.03^{+0.25}_{-0.20}$	64	22.76	46 ±9	$23.12^{+0.24}_{-0.19}$	63 ±13	$22.78^{+0.25}_{-0.20}$
7700	1	≲560	≲20.26	49	22.91	≲92	≲22.22	≲126	≲21.88
7700	10	≲560	≲20.26	50	22.88	≲79	≲22.39	≲109	≲ 22.04
8700	2	536 ±216	$20.18^{+0.56}_{-0.37}$	41	22.97	80 ±32	$22.24^{+0.55}_{-0.37}$	110 ±44	$21.89^{+0.55}_{-0.37}$
8700	6	914 ±233	$19.60^{+0.32}_{-0.25}$	41	22.97	139 ±35	$21.64^{+0.31}_{-0.24}$	191 ±49	$21.30^{+0.32}_{-0.25}$
8700	7	434 ±242	$20.40^{+0.89}_{-0.48}$	41	22.97	58 ±43	$22.59^{+1.47}_{-0.60}$	79 ±59	$22.25^{+1.49}_{-0.61}$
8700	11	510 ±199	$20.23^{+0.54}_{-0.36}$	43	22.91	64 ±25	$22.48^{+0.54}_{-0.36}$	88 ±34	$22.14^{+0.53}_{-0.35}$
8700	15	710 ±196	$19.87^{+0.35}_{-0.26}$	45	22.87	88 ±24	$22.14^{+0.35}_{-0.26}$	120 ±33	$21.80^{+0.35}_{-0.26}$
8700	16	887 ±222	$19.63^{+0.31}_{-0.24}$	45	22.87	120 ±30	$21.80^{+0.31}_{-0.24}$	165 ±41	$21.45^{+0.31}_{-0.24}$
8700	17	751 ±248	$19.81^{+0.44}_{-0.31}$	45	22.87	100 ±33	$22.00^{+0.43}_{-0.31}$	138 ±46	$21.65^{+0.44}_{-0.31}$
8700	18	563 ±194	$20.12^{+0.46}_{-0.32}$	42	22.94	66 ±23	$22.45^{+0.47}_{-0.32}$	90 ±31	$22.11^{+0.46}_{-0.32}$
8700	19	618 ±255	$20.02^{+0.58}_{-0.38}$	45	22.87	79 ±33	$22.25^{+0.59}_{-0.38}$	109 ±45	$21.90^{+0.58}_{-0.38}$
10 500†	4	≲3153	≲18.05	31	23.07	≲402	≲20.28	≲553	≲19.94
10 500†	8	≲1922	≲18.58	32	23.03	≲240	≲20.84	≲330	≲20.50
10 500†	9	≲1508	≲18.85	32	23.03	≲181	≲21.15	≲249	≲20.80

Notes. Apparent airglow continuum radiance at high air masses reported without any corrections. *zenith, emitted + scattered* corresponds directly to Eq. (13). ID can be compared against the table of observations, Table 2. $^{(\dagger)}$No detection, upper limit.

or in the line lists of (Rousselot et al. 2000) for the 10 500 Å band. These line lists are not complete. However, they do contain the brightest atmospheric emission lines. We indicate the van der Loo & Groenenboom (2007, 2008) computed OH lines as a reference in our figures, but since we cannot identify the lines in our spectra, we do not reject these regions from our analysis. Einstein coefficients for the transitions are generally low, and the lines may be faint. However, we cannot rule out the possibility that they affect our measurements. We rejected a region corresponding to 95% of the LSF (see Sect. 2.4) around each skyline found in the Hanuschik (2003) or Rousselot et al. (2000) line lists. Weighted means were calculated from the accepted wavelength bins and are considered the apparent continuum radiance for the bandpass. Additionally, the selected regions were visually inspected to ensure they did not contain spectral lines. We observe the apparent uncorrected airglow continuum radiance at large zenith distances to be on average 350, 560, and 660 ph s^{-1}m^{-2}µm^{-1}arcsec^{-2}, or 20.92, 20.26, and 19.95 mag arcsec^{-2} in the 6720, 7700, and 8700 Å bands, respectively. Moreover, we derive an upper limit of 1500 ph s^{-1}m^{-2}µm^{-1}arcsec^{-2}or 20.8 mag arcsec^{-2} on the 10 500 Å band. The apparent observed flux-calibrated spectra are presented in Figs. A.1, A.2, A.3, A.4, A.5, A.6, and A.7 for all four bandpasses. We present the apparent continuum radiance in Table 3 alongside the zenith-scaled values.

4.2. Zenith equivalent radiance

In order to make comparisons with studies in the literature, the zenith-normalized continuum radiance is calculated and reported in Table 3. Due to the ZL and airglow being large angular area radiance sources, their effective air mass and optical depth scale differently than that of a point source (see Sect. 4.3). For the most part, we follow Noll et al. (2012) for zenith scaling, adapting their model to our case. For scaling purposes, we assume the airglow continuum to originate from the same atmospheric layer as the OH line emission. We take the OH layer altitude and thickness from rocket-borne experiments (Lopez-Moreno et al. 1987; Baker & Stair 1988) and assume that the airglow continuum emission originates from a mean altitude of 87 km with a layer FWHMof 9 km. The following steps were taken in the zenith normalization process:

1. The sky spectra were reduced and flux-calibrated, and the apparent interline continuum was measured at the observed zenith distance, z.
2. The contribution of extra-atmospheric emission was computed for the time and pointing.
3. The effective optical depths for airglow and ZL were calculated.
4. The extra-atmospheric emission was attenuated and subtracted from the total observed intensity.

5. A scaling factor for the thickness of the airglow emitting layer was calculated, and the line-of-sight emitted airglow was scaled to the zenith equivalent.
6. The airglow emission scattered to the line of sight at zenith was added to give the apparent zenithal airglow radiance.

The assumption of atmospheric attenuation being due to scattering only is generally true for the 6720, 8700 and 10 500 Å bands, but the blue half of the 7700 Å band is affected by O_2 absorption.

4.3. Airmass scaling

The altitude and thickness of the emitting airglow continuum layer were assumed to be similar to that of OH line emission (Baker & Stair 1988). Due to the large zenith distance z observed, and the finite thickness of the emitting airglow layer, the typical plane-parallel atmosphere airmass scaling, $X = \sec(z)$, could not be used for the airglow emission, $I_{\rm ag}$. The thickness of the emitting airglow layer increases significantly less steeply, and the typical relation to describe the scaling, $s_{\rm ag}$, is the so-called van Rhijn function, as follows:

$$s_{\rm ag} = \frac{I_{\rm ag}(z)}{I_{\rm ag}(0)} = \left(1 - \left(\frac{R\sin(z)}{R+h}\right)^2\right)^{-1/2}, \quad (1)$$

where $I_{\rm ag}(z)$ is the airglow intensity at zenith distance z, $I_{\rm ag}(0)$ is the airglow intensity at zenith, R is the radius of Earth, and h is the height of the emitting layer above Earth's surface. Eq. (1) assumes that the thickness of the emitting layer can be neglected. This is generally valid for lower values of z but breaks down when the observer is either close to the emitting layer or points close to the horizon. We used an earlier step from van Rhijn's derivation, taking the airglow layer thickness as a side length difference of two scalene obtuse triangles, which is the same as Eq. (19) in van Rhijn (1921). Using positive quadratic solutions for both triangles, the OH emission scaling $s_{\rm ag}$ factor becomes

$$s_{\rm ag} = \frac{I_{\rm ag}(z)}{I_{ag}(0)} = \sqrt{R^2 cos^2(z) + 2Rh_2 + h_2^2} - \sqrt{R^2 cos^2(z) + 2Rh_1 + h_1^2}, \quad (2)$$

where z is the zenith distance, R is Earth's radius, h_1 is the altitude of the emitting layer, and h_2 is the altitude of the observer. Our observations cover zenith distances of 77–81°, and the observer's altitude begins to make small differences when $z \gtrsim 79°$.

Due to scattering in the line of sight, the air mass of a large solid angle source scales differently than that of a point source. For diffuse emission outside the atmosphere, we used

$$X_{\rm zl}(z) = (1 - 0.96\sin^2(z))^{-1/2}, \quad (3)$$

(Krisciunas & Schaefer 1991; Noll et al. 2012) to calculate the ZL air mass. Light from the airglow layer travels a shorter distance in the atmosphere. Therefore, we used

$$X_{\rm ag}(z) = (1 - 0.972\sin^2(z))^{-1/2}, \quad (4)$$

as the airglow air mass (Noll et al. 2012). Additionally, in order to scale the airglow emission to zenith, the reduction in optical depth due to line-of-sight scattering was considered. We followed the treatise of Noll et al. (2012) and applied their methodology to our site, extending their parametrization to our case.

Optical depths for large solid angle sources were reduced due to line-of-sight scattering. The reduction can be represented as an effective optical depth (Noll et al. 2012),

$$\tau_{\rm eff} = f_{\rm ext}\tau_0, \quad (5)$$

where $f_{\rm ext}$ is the extinction reduction factor, and τ_0 is the zenithal optical depth. We adopted the reduction factors $f_{\rm ext}$ for ZL Rayleigh and Mie scattering from Noll et al. (2012) as follows:

$$f_{\rm ext,\,zl,\,R} = 1.407\log I_{\rm zl} - 2.692, \quad (6)$$
$$f_{\rm ext,\,zl,\,M} = 1.309\log I_{\rm zl} - 2.598 \quad (7)$$

where I_{zl} is the ZL outside atmosphere, in units of $\mathrm{W^{-8}\,m^{-2}\,\mu m^{-1}\,sr^{-1}}$. Eqs. (6) and (7) require that $\log I_{\rm zl} \leq 2.44$, which was met in all our observations. Similarly, we adopted the following reduction factors for the airglow emission Rayleigh and Mie components:

$$f_{\rm ext,\,ag,\,R} = 1.669\log X_{\rm ag} - 0.146, \quad (8)$$
$$f_{\rm ext,\,ag,\,M} = 1.732\log X_{\rm ag} - 0.318. \quad (9)$$

Components contributing to the optical depth include Rayleigh scattering, Mie scattering, and molecular absorption. The zenithal optical depth is

$$\tau_0(\lambda) = \tau_R(\lambda) + \tau_M(\lambda) + \tau_A(\lambda), \quad (10)$$

where τ_R, τ_M, and τ_A stand for the Rayleigh, Mie, and absorption components, respectively. The values, τ_M and τ_A, are estimated based on the ESO Sky Calc model for La Silla. Liou (2002) provides the following formula for Rayleigh scattering optical depth with wavelengths in μm:

$$\tau_R(\lambda, h, p) = \frac{p}{p_s}(a + bh)\,\lambda^{-(c+d\lambda+e/\lambda)}, \quad (11)$$

where h is the altitude in kilometers, p is the pressure, $p_S = 1013.25$ hPa, and the constants are $a = 0.00864$, $b = 6.5\times10^{-6}$, $c = 3.916$, $d = 0.074$, and $e = 5\times10^{-2}$. Eq. (11) provides comparable, though slightly lower, τ_R values than the nonpressure-dependent King (1985) model for Observatorio del Roque de los Muchachos.

Atmospheric transmission as a function of wavelength is expressed as

$$t(\lambda, z) = e^{-\tau_0(\lambda)X(z)}, \quad (12)$$

where τ_0 is the optical depth in zenith, and X is the air mass. We calculated the effective transmissions $t_{\rm ag}$ and $t_{\rm zl}$ for airglow and ZL, respectively.

Lastly, considering the different air masses and the optical depth reduction factors for ZL and airglow, the zenith equivalent airglow intensity can was calculated as

$$I_{\rm ag}(0) = \frac{I_{\rm ag}(z) - I_\star - (I_{\rm zl} + I_{GBL} + I_{EBL})\,t_{\rm eff,\,zl}(\lambda, z)}{t_{\rm eff,\,ag}(\lambda, z)\,s_{\rm ag}}\,t_{\rm eff,ag}(\lambda, 0), \quad (13)$$

where $I_{ag}(z)$ denotes the observed airglow intensity at zenith distance z, $I_\star$ represents scattered star light, I_{GBL} represents galactic background light, and I_{EBL} denotes extra-galactic background light intensity. $t_{eff,ag}$ and $t_{eff,zl}$ denote the effective transmission for airglow and ZL, respectively, and s_{ag} is the scaling factor, which compensates for the difference in apparent emitting layer thickness. Notice that $t_{eff,ag}(\lambda, 0)$ is greater than one due to line-of-sight scattering. We calculated the mean air mass for each observation from the telescope altitude and pointing trajectory during the observation.

4.4. Uncertainty due to extinction

Observing at a zenith distance of $z \sim 80°$, the line of sight extends several hundreds of kilometers in the lower atmosphere before reaching the altitude of the mesopause. The short wavelength half of the 7700 Å bandpass contains significant O_2 absorption. Instead of correcting for absorption, we ignored the affected range. None of our bands are affected by water vapor absorption. The largest airmass data point for the Noll et al. (2012) $f_{ext\,ag}$ fit is $X = 2.75$. We extrapolate their fit to $X > 4$. Overestimating $f_{ext,\,ag}$ leads to overestimating $I_{ag}(0)$.

4.5. Zodiacal light

The ZL spectrum is a reflected solar spectrum from interplanetary dust, and the ZL surface brightness depends on the solar elongation angle and the longitude of Earth's ascending node. State-of-the-art ZL models are based on COBE/DIRBE SWIR data (Kelsall et al. 1998; Wright 1998). The bluest observed COBE/DIRBE band is centered at 1.25 µm, and the DIRBE ZL models are extrapolated to VIS–NIR wavelengths. Extrapolation assumes an albedo for interplanetary dust that is not well known, leaving non-negligible uncertainty on the modeled ZL radiance at VIS and NIR ranges. The Wright (1998) model enforces the so-called "strong no-zodi principle," requiring the ZL at high Galactic latitude at 25 µm to be isotropic and constant in time. Due to this condition, the Wright (1998) model provides systematically higher ZL radiance than the Kelsall et al. (1998) model. It has been suggested that the Kelsall et al. (1998) ZL model underestimates the ZL for wavelengths shorter than <3.5 µm Tsumura et al. (2013), and that the model may miss a diffuse ZL component (Kawara et al. 2017). The literature does not clearly indicate which model to adopt for VIS and NIR wavelengths, and because the zenith scaling in this work is ZL model dependent, we computed the results based on both models. Additionally, we compared our results against ESO SkyCalc v.2.0.9[2] (Noll et al. 2012; Jones et al. 2013), a ZL model based on visual wavelength observations by Levasseur-Regourd & Dumont (1980) on Tenerife in the late 1960s and early 1970s, which uses the reddening relations of Leinert et al. (1998).

We find a difference of a few percent in the scaled zenithal airglow radiance when using either the DIRBE (Kelsall et al. 1998) ZL model or the ESO SkyCalc (Noll et al. 2012) ZL model, which is below the uncertainty of our measurement. Using the Wright (1998) DIRBE ZL model with Gorjian et al. (2000) parameters, our results are ∼10% lower compared to the Kelsall et al. (1998) DIRBE model. We report and show I_{zl} values based on the Kelsall et al. (1998) model only. We calculated the DIRBE ZL radiance for the date and pointing using the InfraRed Science Archive (IRSA), Infrared Processing & Analysis Center (IPAC) Euclid background model calculator, Versions 1 and 4[3]. Version 1 is based on the Kelsall et al. (1998) model, while Version 4 is based on the Wright (1998); Gorjian et al. (2000) model.

4.6. Other diffuse radiation

As noted in Sect. 2.2, we assumed that the Moon does not contribute to the total observed sky radiance. In addition to the ZL, we considered contributions from scattered starlight as well as galactic- (I_{GBL}) and extra-galactic background light (I_{EBL}), which are very low compared to the ZL. For the scattered starlight surface brightness $I_\star$, we used values of 7, 4.4, 3.1, and 2.3 ph s^{-1}m^{-2}µm^{-1}arcsec^{-2} for 6720, 7700, 8700, and 10 500 Å bands, respectively (Noll et al. 2012). We adopted I_{GBL} and I_{EBL} components from the same IRSA/IPAC calculator, which is based on Arendt et al. (1998). Apart from a few pointings, both I_{GBL} and I_{EBL} contribute negligibly ∼1 ph s^{-1}m^{-2}µm^{-1}arcsec^{-2} in the bandpasses.

5. Discussion

5.1. Airglow or instrumental

This work originally set out to investigate whether previously observed airglow continuum values could be explained by grating-scattered light contribution. At the observed wavelengths, the detected continuum signal is clear despite being faint, and its presence cannot be attributed to the grating-scattered light originating from the brighter OH lines within our bandwidths (see Sect. 2.4). We estimate conservatively that the spectrograph LSF wing contribution is <1 ph s^{-1}m^{-2}µm^{-1}arcsec^{-2} in the 6720 Å band and <10 ph s^{-1}m^{-2}µm^{-1}arcsec^{-2} in the 7700 and 8700 Å bands. The total grating-scattered light contribution is below the systematic uncertainty limits: the observed continuum is not introduced by the grating-scattered light in our optical system. The observed continuum or pseudo-continuum is real and of atmospheric or extra-atmospheric origin. With our R∼4000 spectra, we are not be able to distinguish between true continuum and densely spaced, weaker atmospheric spectral lines. Although unidentifiable, our chosen line-free regions within our bandpasses may contain OH lines. We indicate positions computed by van der Loo & Groenenboom (2007, 2008) in our figures.

5.2. Unknown and unidentified lines

The spectral ranges that are considered to be devoid of atmospheric spectral lines are based on the observational line list of Hanuschik (2003) and Rousselot et al. (2000). The selected regions contain additional known OH transitions (van der Loo & Groenenboom 2007, 2008), which we do not detect in our spectrum. In the 8700 Å band, we see a correlation between the continuum and OH and O_2 line emission. One explanation for this is that we are affected by the fainter OH lines, which we were unable to identify. Several of these OH transitions have long lifetimes, and the lines may be faint. We indicate the lines with tick marks scaled by the line's Einstein coefficient in our figures. Additionally, a faint line is detected in all spectra observed during the New Year 2022 run in the range 8731–8732 Å, which

[2] https://www.eso.org/observing/etc/bin/gen/form?INS.MODE=swspectr+INS.NAME=SKYCALC

[3] https://irsa.ipac.caltech.edu/applications/BackgroundModel/

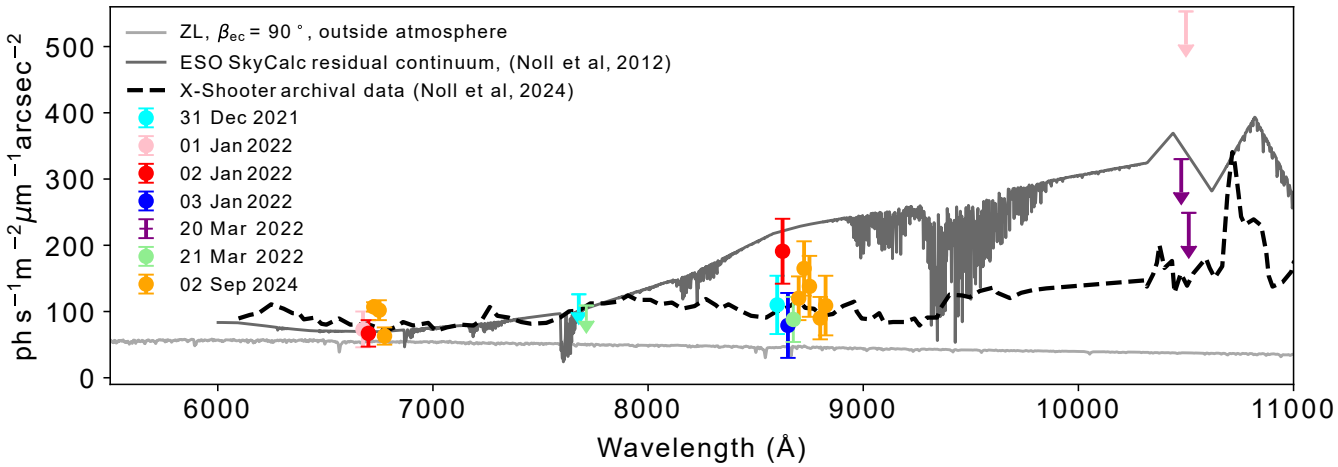

Fig. 3. Zenith equivalent airglow continuum radiance in the observed bandpasses according to Eq. (13). Data points are shifted by 25 Å steps to prevent them from being plotted over each other. The ESO SkyCalc yearly average residual airglow continuum (Noll et al. 2012; Jones et al. 2013), the X-shooter 2009–2019 mean airglow continuum (Noll et al. 2024), and the ZL spectrum above the atmosphere toward the ecliptic north pole (Meftah et al. (2018) solar spectrum scaled to Kelsall et al. (1998) model) are shown. Upper limits are derived in the 10 500 Å band and are indicated by arrows.

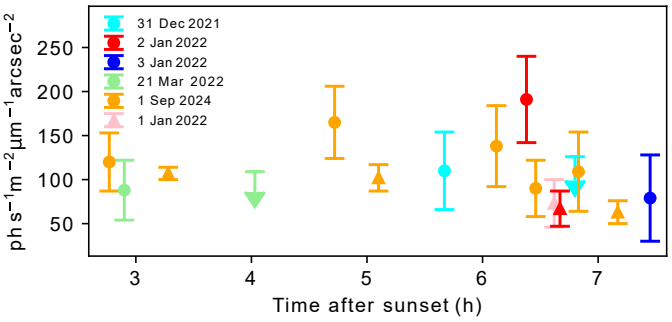

Fig. 4. Zenith equivalent continuum radiance as a function of time after sunset in the 6720 Å (triangles), 7700 Å (upper limits, arrows down), and 8700 Å (circles) bands.

disappears from the rest of the spectra. The following ions can be found in the NIST line database: Ti III, W I, Fe VII, Mn II, and V II (NIST, Kramida et al. 2023), all of which are unusual appearances in the night sky spectrum. The line could potentially originate from either fireworks or a deposition of micrometeorites (Plane et al. 2015). These observations were carried out two weeks after the peak of the Geminids meteor shower. Due to the lack of certainty on its origin and its faintness, we do not reject the spectral range in our analysis.

5.3. Temporal variability and color

In a typical case, we observed several hours after sunset. However, based on the few measurements at the beginning of the night, the airglow continuum radiance does not seem to change much over the course of the night (Fig. 4). By and large, the measured continuum seems stable and is almost flat in color, with a potential slight increase toward the red. Typically when measuring two bands during the same night, the bands measured comparable levels, with the exception being January 1, 2022, which shows a significant difference in emission between the 6720 and 8700 Å bands (see Sect. 5.4 for further discussion). The 7700 and 8700 Å bands were observed with a one-hour time difference on December 30, 2021 and March, 21 2022. On both occasions, the 7700 Å band measured equal radiance to the 8700 Å band. The 6720 and 8700 Å bands were observed with a somewhat shorter time difference on January 2, 2022, and several times on September 1, 2024. On September 1, 2024, the 8700 Å radiance remained constant within our measurement errors, with a weighted average of 126 ph s^{-1}m^{-2}μm^{-1}arcsec^{-2}, or 21.74 mag arcsec^{-2} and a slight tendency for the radiance to decrease toward the end of the night. The 6720 Å band has lower measurement errors and shows a statistically significant decrease over the night, with a ∼40% drop in radiance between the first and last measurement. The color of the resulting continuum spectrum is flat with a marginal increase toward the red, see Fig. 3. Our data points overlap with the mean airglow spectrum of Noll et al. (2024) for Cerro Paranal, Chile.

5.4. Relation to solar activity

On January 2, 2022, the airglow continuum and OH line radiance in the 8700 Å bandpass (ID 6) measured elevated values relative to the other nights, prompting us to look for an explanation. We sought a relation to various solar activity parameters (Fig. 5). Unfortunately, the dataset is small and biased with respect to space weather: strong solar radiation activity coincided with slow solar wind conditions. No clear conclusion can be drawn, given the high temporal variability of the airglow radiance. On January 2, 2022, the 8700 Å (ID 6) measured the highest level in our data and stands out as a possible outlier in the solar activity plots (hollow marker in Fig. 5). Potentially, the increase in radiance could be due to a coronal mass ejection hitting Earth's magnetosphere during the observation. A C1.06-class flare occurred 45 min before the beginning of the observation, and another B8.42 flare 30 min before the observation. At the beginning of the exposure, DSCOVR registered an increase in solar wind speed from an average of 525 km s^{-1} up to 600 km s^{-1}, and the solar proton density increased from an average of 11 p$^+$ cm^{-1} to momentarily >16 p$^+$ cm^{-1}, which suggests the passage of a coronal mass ejection past DSCOVR. It would have taken about 40–45 min for the particles to reach Earth's magnetosphere, which would match the coronal mass ejection hitting right at the beginning of the observation. The

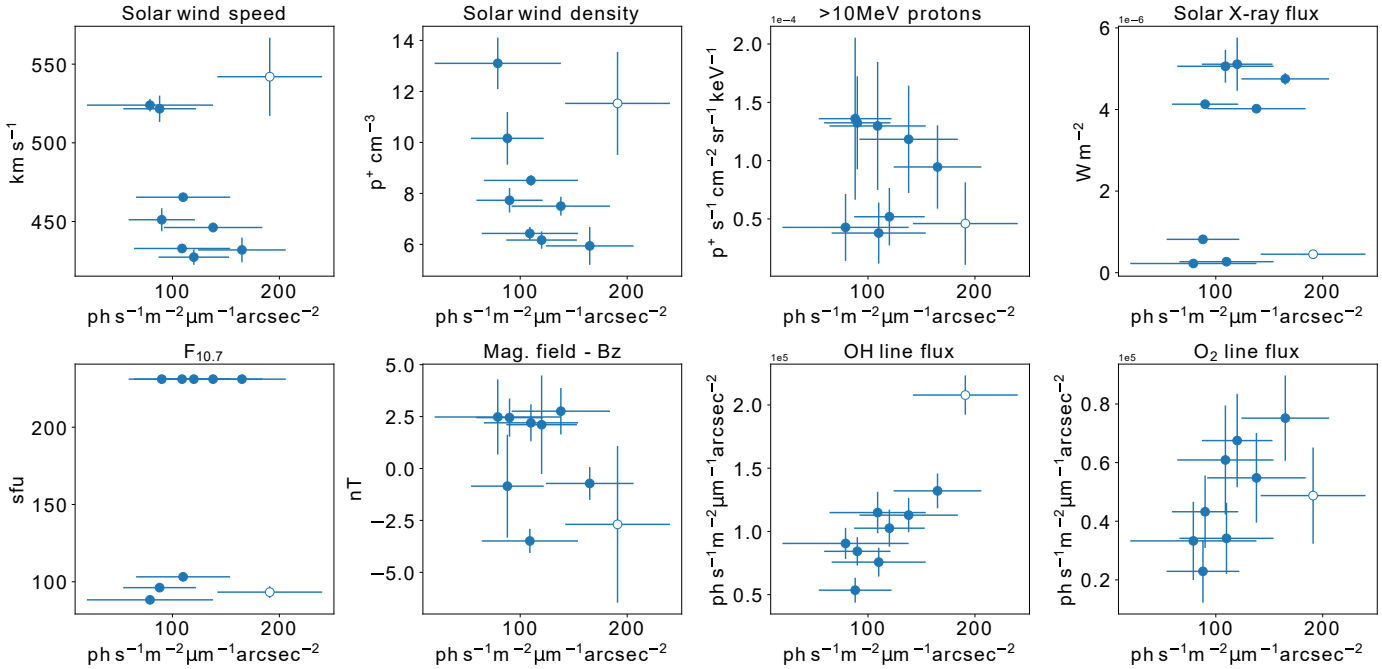

Fig. 5. Airglow continuum dependence in the 8700 Å bandpass on solar activity parameters, and on the OH and O_2 line emissions. High solar activity coincides with slow solar wind in our dataset. Observation Nº 6 from January 2, 2022, with the highest measured 8700 Å radiance, is a potential outlier, as discussed in Sect. 5.4, and is indicated with a hollow symbol. The OH flux is a sum of blended 7-3 R OH lines (~8761, 8768, 8778, and 8791 Å in our spectra), while the O_2 flux is a sum of blended O_2 P and Q -branch lines in the range 8645–8696 Å.

6720 Å band (ID 5) observed right after the 8700 Å measures a low continuum level but shows elevated OH 6-1 $P2_{e,f}(6.5)$ and 6-1 $P1_{e,f}(7.5)$ line emission, considering that the observation was performed more than 6.5 h after sunset.

5.5. Comparison to the literature

We attempted an exhaustive literature search as part of this study to compare measurements over previous solar cycles. However, direct comparison was difficult due to differences in reporting. Few publications report the total observed continuum radiance (Broadfoot & Kendall 1968; Maihara et al. 1993b; Cuby et al. 2000; Hanuschik 2003; Sullivan & Simcoe 2012; Ellis et al. 2012; Trinh et al. 2013; Oliva et al. 2015; Nguyen et al. 2016), while others report zenith-scaled equivalents or a breakdown by components (Sternberg & Ingham 1972; Gadsden & Marovich 1973; Noxon 1978), which are ZL model- and atmospheric scattering-dependent. In some cases, exact pointing and time of observation were not reported. Allowing for these differences, the airglow continuum levels measured previously can be viewed as comparable to what we find in this work. A collections of previous airglow continuum measurements are presented in Table B.1, and units from each study were converted to those used in our work.

While the OH line emission has been studied at Observatorio del Roque de los Muchachos (Oliva et al. 2013; Franzen et al. 2018, 2019), only a single report on NIR or SWIR airglow continuum can be found in the literature (Oliva et al. 2015). Oliva et al. (2015) found comparable continuum radiance in the H band comparable to values reported for Las Campanas, Chile (Sullivan & Simcoe 2012), Cerro Paranal, Chile (Noll et al. 2024), Mauna Kea, Hawaii (Maihara et al. 1993b), and Siding Spring, Australia (Trinh et al. 2013). All VIS–NIR continuum radiance measurements were done elsewhere, most notably at Cerro Paranal, Chile Hanuschik (2003); Noll et al. (2024). We compare our results to measurements made at other sites below.

Hanuschik (2003) observed apparent continuum radiance of 300–350 ph $s^{-1}m^{-2}\mu m^{-1}arcsec^{-2}$ in the wavelength range observed in this work. Exact dates of observations are not reported, but the reported Moon illumination fraction restricts the dates to 20–21 June 2001. Hanuschik (2003) observed at a mean air mass of $z = 1.11$, forcing the pointings quite close to the ecliptic equator, with a maximum distance of approximately $\beta ec \sim -33°$. The Kelsall et al. (1998) model gives an ~100 ph $s^{-1}m^{-2}\mu m^{-1}arcsec^{-2}$ ZL contribution to the total apparent continuum. The Hanuschik (2003) spectra appear bluer than that which we find in this work, but the level is comparable after accounting for ZL on the nights associated with stronger solar activity in our study. On 20–21 June 2001, DRAO $F_{10.7}$ ranged between 199–204 sfu, indicating moderately high solar activity.

Sternberg & Ingham (1972) reported a time series of ZL corrected observations at 8200 Å toward the North Celestial Pole from the Haute-Provence observatory, during nights of August 18 to 19, 1969 with a nightly decrease from 300 to 190 ph $s^{-1}m^{-2}\mu m^{-1}arcsec^{-2}$. Kelsall et al. (1998) reported a ZL radiance for their pointing of ~40 ph $s^{-1}m^{-2}\mu m^{-1}arcsec^{-2}$. The level is similar to that found by Hanuschik (2003). The decay resembles behavior observed in this work on 1 September 2024. Sternberg & Ingham (1972) observed bad weather, potentially affecting the observations, without elaborating further. Sternberg & Ingham (1972) found a close to constant continuum emission of 75 ph $s^{-1}m^{-2}\mu m^{-1}arcsec^{-2}$ at 6750 Å on 2 June 1970.

The ESO Sky Calc (Noll et al. 2012; Jones et al. 2013; Noll et al. 2013) residual airglow continuum offers another point of comparison. The residual airglow continuum model is based on 26 averaged early X-shooter spectra. The Noll et al. (2012) residual continuum showed a significant increase toward

red between 7000 and 9000 Å, which resembles the behavior reported by Broadfoot & Kendall (1968). Similar reddening was also reported by Gadsden & Marovich (1973). Noxon (1978) did not observe an increase in radiance and suggested that the reddening reported by Gadsden & Marovich (1973) and Broadfoot & Kendall (1968) may have been instrumental. More recently, Noll et al. (2024) attributes the increase toward longer wavelengths in the Noll et al. (2012) study to the low resolution of the FOcal Reducer and low dispersion Spectrograph 1 (FORS 1) used in that study. Nonetheless, we may have witnessed similar reddening associated with stronger solar activity on the night of September 1, 2024. Noll et al. (2024) finds a much flatter airglow continuum spectrum based on a larger X-shooter dataset covering late 2009 to 2019. The flat continuum spectrum is similar to what we observed at Roque de los Muchachos.

5.6. Implications

Our observations indicate a dark interline NIR sky. To take full advantage of it for faint object spectroscopy, its properties should be investigated further. Our work may also encourage the introduction of OH line suppressors and grating-stray-light-reducing spectrograph designs to workhorse NIR and SWIR spectrographs. Successful OH line suppressors based on line masks (e.g., Maihara et al. 1993a; Iwamuro et al. 2001; Parry et al. 2004) and Fiber Bragg Gratings (e.g., Ellis et al. 2012) have been demonstrated in the literature. The grating-scattering-wing-reducing spectrograph designs use the grating in a double-pass configuration combined with a secondary slit between the dispersions. The double-pass spectrograph can be implemented either as a scanning monochromator (Enard 1982) (compatible with long slits, but records only a single spectral element at a time), or as a white-pupil spectrograph with a beam rotation between the two dispersions (Andersen & Andersen 1992; Viuho et al. 2022) (confined to use with round apertures, i.e., fibers, with the advantage of recording the full spectral range at once).

We observed variations of up to a factor of two in the VIS-NIR airglow continuum on timescales from tens of minutes to hours. Our observations do not temporally resolve the shorter timescale variations associated with mesospheric buoyancy waves, and it is possible that the airglow continuum exhibits variation similar to those of the airglow line emission on minute timescales. We do not have data to study the seasonal variability reported by Patat (2008) and Noll et al. (2024), and it is difficult to secure observing time for a nonstandard optical configuration for a long-term monitoring program. Temporal variability of the continuum radiance needs to be taken into account when designing faint object spectrographs for ground-based observations, even when OH suppressing or double-pass techniques are being used.

6. Conclusion

We measured the NIR airglow continuum radiance at the Observatorio del Roque de los Muchachos with control over the instrumental line wing contribution. We find the continuum radiance to range between 60–170 ph $s^{-1} m^{-2} \mu m^{-1} arcsec^{-2}$, or 21.4–22.8 mag $arcsec^{-2}$, depending on the bandpass and the time of observation. The zenith-scaled airglow continuum radiance is two to four times brighter than the ZL toward the ecliptic poles: the darkest foreground available for ground- and current space-based observatories. The observations carried out under photometric observing conditions establish a solid measurement for the darkest sky conditions. We observe the continuum to be stable with a modest decay toward the end of the night. The observations presented here were sporadically spread across the year, and we are unable to study the seasonal variability reported in the literature. We promote a long-term observing campaign for its analysis. Our work demonstrates that the VIS-NIR sky continuum can be very dark under photometric conditions, offering close to ZL-limited foreground from the ground in the NIR sensitivity range of silicon photodetectors, encouraging the design of astronomical spectrographs taking advantage of the dark interline sky.

Data availability

Raw data are available on the NOT's fits archive, or upon request from the corresponding author. Scripts used as part of the work are available upon reasonable request from the corresponding author.

Acknowledgements. The Cosmic Dawn Center (DAWN) is funded by the Danish National Research Foundation under grant DNRF140. The data presented here were obtained in part with ALFOSC, which is provided by the Instituto de Astrofisica de Andalucia (IAA) under a joint agreement with the University of Copenhagen and NOT. The COBE datasets were developed by NASA's Goddard Space Flight Center under the guidance of the COBE Science Working Group and were provided by the NSSDC. DSCOVR and GOES data courtesy to National Oceanic (NOAO) and Atmospheric Administration Space Weather Prediction Center (SWPC). $F_{10.7}$ data courtesy to the DRAO. We thank J. Munday, V. Pinter, A. E. T. Viitanen, and A. N. Sørensen for discussion and their valuable feedback on the manuscript.

References

Andersen, M. I., & Andersen, J. 1992, in ESO Workshop on High Resolution Spectroscopy with the VLT, 40 (European Southern Observatory), 235
Arendt, R. G., Odegard, N., Weiland, J. L., et al. 1998, ApJ, 508, 74
Baker, D. J., & Stair, A. T. 1988, Phys. Scr., 37, 611
Bates, D. R. 1993, Proc. Roy. Soc. Lond. Ser. A: Math. Phys. Sci., 443, 227
Broadfoot, A. L., & Kendall, K. R. 1968, J. Geophys. Res., 73, 426
Colina, L., & Bohlin, R. C. 1994, AJ, 108, 1931
Cuby, J. G., Lidman, C., & Moutou, C. 2000, The Messenger, 101, 2
Dwek, E., Arendt, R. G., Hauser, M. G., et al. 1998, ApJ, 508, 106
Ellis, S. C., & Bland-Hawthorn, J. 2008, MNRAS, 386, 47
Ellis, S. C., Bland-Hawthorn, J., Lawrence, J., et al. 2012, MNRAS, 425, 1682
Ellis, S. C., Bland-Hawthorn, J., Lawrence, J. S., et al. 2020, MNRAS, 492, 2796
Enard, D. 1982, SPIE Conf. Ser., 331, 232
Flewelling, H. A., Magnier, E. A., Chambers, K. C., et al. 2020, ApJS, 251, 7
Franzen, C., Espy, P. J., Hibbins, R. E., & Djupvik, A. A. 2018, J. Geophys. Res.: Atmos., 123, 10935
Franzen, C., Espy, P. J., Hofmann, N., Hibbins, R. E., & Djupvik, A. A. 2019, Atmosphere, 10, 637
Gadsden, M., & Marovich, E. 1973, J. Atmos. Terrestr. Phys., 35, 1601
Giavalisco, M., Ferguson, H. C., Koekemoer, A. M., et al. 2004, ApJ, 600, L93
Gorjian, V., Wright, E. L., & Chary, R. R. 2000, ApJ, 536, 550
Grygalashvyly, M., Pogoreltsev, A. I., Andreyev, A. B., Smyshlyaev, S. P., & Sonnemann, G. R. 2021, Ann. Geophys., 39, 255
Hanuschik, R. W. 2003, A&A, 407, 1157
Hauser, M. G., Arendt, R. G., Kelsall, T., et al. 1998, ApJ, 508, 25
Iwamuro, F., Motohara, K., Maihara, T., Hata, R., & Harashima, T. 2001, PASJ, 53, 355
Jones, A., Noll, S., Kausch, W., Szyszka, C., & Kimeswenger, S. 2013, A&A, 560, A91
Kawara, K., Matsuoka, Y., Sano, K., et al. 2017, PASJ, 69, 31
Kelsall, T., Weiland, J. L., Franz, B. A., et al. 1998, ApJ, 508, 44
Khomich, V. Y., Semenov, A. I., & Shefov, N. N. 2008, Airglow as an Indicator of Upper Atmospheric Structure and Dynamics, 1st edn. (Berlin, Heidelberg: Springer-Verlag)
King, D. L. 1985, Atmospheric Extinction at the Roque de los Muchachos Observatory, La Palma, RGO/La Palma technical note no 31
Koch, F., Zilk, M., & Glaser, T. 2021, Proc. SPIE, 11783, 1178304
Kramida, A., Yu. Ralchenko, Reader, J., & NIST ASD Team 2023, NIST Atomic Spectra Database (ver. 5.11), [Online]. Available: https://physics.nist.gov/asd [2024, October 15]. National Institute of Standards and Technology, Gaithersburg, MD

Krassovsky, V. I., Shefov, N. N., & Yarin, V. I. 1962, Planet. Space Sci., 9, 883
Krisciunas, K. 1997, PASP, 109, 1181
Krisciunas, K., & Schaefer, B. E. 1991, PASP, 103, 1033
Leinert, C., Väisänen, P., Mattila, K., & Lehtinen, K. 1995, A&AS, 112, 99
Leinert, C., Bowyer, S., Haikala, L. K., et al. 1998, A&AS, 127, 1
Levasseur-Regourd, A. C., & Dumont, R. 1980, A&A, 84, 277
Liou, K.-N. 2002, An Introduction to Atmospheric Radiation, 2nd edn., International Geophysics Series, 84 (San Diego, Calif.: Academic Press)
Lopez-Moreno, J. J., Rodrigo, R., Moreno, F., Lopez-Puetas, M., & Molina, A. 1987, Planet. Space Sci., 35, 1029
Maihara, T., Iwamuro, F., Hall, D. N. B., et al. 1993a, in Infrared Detectors and Instrumentation, 1946 (International Society for Optics and Photonics), 581
Maihara, T., Iwamuro, F., Yamashita, T., et al. 1993b, PASP, 105, 940
Mattila, K., Väisänen, P., & Appen-Schnur, G. F. O. V. 1996, A&AS, 119, 153
Meftah, M., Damé, L., Bolsée, D., et al. 2018, A&A, 611, A1
Moreels, G., Clairemidi, J., Faivre, M., et al. 2008, Exp. Astron., 22, 87
Murdin, P. 1986, Geology and meteorology of Saharan dust, RGO/La Palma technical note no. 41
Nguyen, H. T., Zemcov, M., Battle, J., et al. 2016, PASP, 128, 094504
Noll, S., Kausch, W., Barden, M., et al. 2012, A&A, 543, A92
Noll, S., Kausch, W., Barden, M., et al. 2013, The Cerro Paranal Advanced Sky Model, VLT-MAN-ESO-19550-5339
Noll, S., Kimeswenger, S., Proxauf, B., et al. 2017, J. Atmos. Sol. Terrestr. Phys., 163, 54
Noll, S., Plane, J. M. C., Feng, W., et al. 2024, Atmos. Chem. Phys., 24, 1143
Noll, S., Schmidt, C., Hannawald, P., Kausch, W., & Kimeswenger, S. 2025, EGUsphere, 2025, 1
Noxon, J. F. 1978, Planet. Space Sci., 26, 191
Oke, J. B. 1974, ApJS, 27, 21
Oliva, E., Origlia, L., Maiolino, R., et al. 2013, A&A, 555, A78
Oliva, E., Origlia, L., Scuderi, S., et al. 2015, A&A, 581, A47
Osterbrock, D. E., Fulbright, J. P., Martel, A. R., et al. 1996, PASP, 108, 277
Parry, I., Bunker, A., Dean, A., et al. 2004, in Ground-based Instrumentation for Astronomy, 5492, eds. A. F. M. Moorwood, & M. Iye
Patat, F. 2008, A&A, 481, 575
Pickles, A. J. 1998, PASP, 110, 863
Plane, J. M., Feng, W., & Dawkins, E. C. 2015, Chem. Rev., 115, 4497
Rousselot, P., Lidman, C., Cuby, J.-G., liu, G., & Monnet, G. 2000, A&A, 354, 1134
Rubin, D., Aldering, G., Antilogus, P., et al. 2022, ApJS, 263, 1
Scoville, N., Abraham, R., Aussel, H., et al. 2007, ApJS, 172, 38
Smith, A. K. 2012, Surv. Geophys., 33, 1177
Smith, S. M., Scheer, J., Reisin, E. R., Baumgardner, J., & Mendillo, M. 2006, J. Geophys. Res.: Space Phys., 111, A09309
Sobolev, V. G. 1978, Planet. Space Sci., 26, 703
Sternberg, J. R., & Ingham, M. F. 1972, MNRAS, 159, 1
Sullivan, P. W., & Simcoe, R. A. 2012, PASP, 124, 1336
Tapping, K. F. 2013, Space Weather, 11, 394
Tilvi, V., Rhoads, J. E., Hibon, P., et al. 2010, ApJ, 721, 1853
Tody, D. 1986, SPIE Conf. Ser., 627, 733
Tody, D. 1993, in Astronomical Society of the Pacific Conference Series, 52, Astronomical Data Analysis Software and Systems II, eds. R. J. Hanisch, R. J. V. Brissenden, & J. Barnes, 173
Trinh, C. Q., Ellis, S. C., Bland-Hawthorn, J., et al. 2013, MNRAS, 432, 3262
Tsumura, K., Matsumoto, T., Matsuura, S., et al. 2013, PASJ, 65, 119
van der Loo, M. P. J., & Groenenboom, G. C. 2007, J. Chem. Phys., 126, 114314
van der Loo, M. P. J., & Groenenboom, G. C. 2008, J. Chem. Phys., 128, 159902
van Dokkum, P. G. 2001, PASP, 113, 1420
van Rhijn, P. J. 1921, Publications of the Astronomical Laboratory at Groningen, 31, 1
Venemans, B. P., McMahon, R. G., Parry, I. R., et al. 2009, in Astrophysics and Space Science Proceedings, 9, Science with the VLT in the ELT Era, 187
Verro, K., Trager, S. C., Peletier, R. F., et al. 2022, A&A, 660, A34
Viuho, J. K. M., Andersen, M. I., & U., F. J. P. 2022, in Ground-based and Airborne Instrumentation for Astronomy IX, 12184, eds. C. J. Evans, J. J. Bryant, & K. Motohara, International Society for Optics and Photonics (SPIE), 1218456
Weaver, J. R., Kauffmann, O. B., Ilbert, O., et al. 2022, ApJS, 258, 11
Williams, R. E., Blacker, B., Dickinson, M., et al. 1996, AJ, 112, 1335
Windhorst, R. A., Carleton, T., O'Brien, R., et al. 2022, AJ, 164, 141
Woods, T. N., Wrigley, R. T., Rottman, G. J., & Haring, R. E. 1994, Appl. Opt., 33, 4273
Wright, E. L. 1998, ApJ, 496, 1

Appendix A: Observed apparent continuum spectra

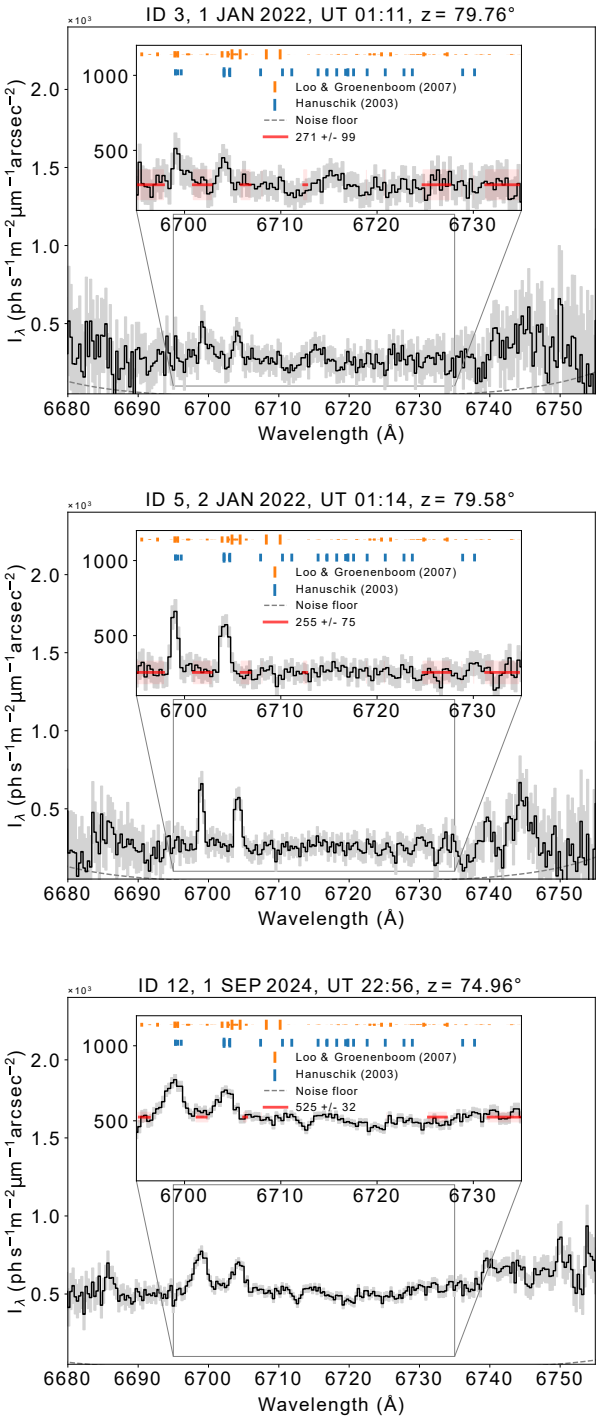

Fig. A.1. Apparent airglow spectra observed in 6720 Å band. The 2022 spectra were recorded with a 0.5″slit whereas, the 2024 spectra are recorded with a 1.3″slit. Spectral lines found in Hanuschik (2003) are indicated with blue ticks, with the tick length indicating relative intensity. Locations of computed OH lines by van der Loo & Groenenboom (2007, 2008) are shown with orange ticks, with the tick length indicating the line's Einstein coefficient. The noise floor is shown as a dashed gray line, and the spectral regions used for sampling the continuum are indicated in red.

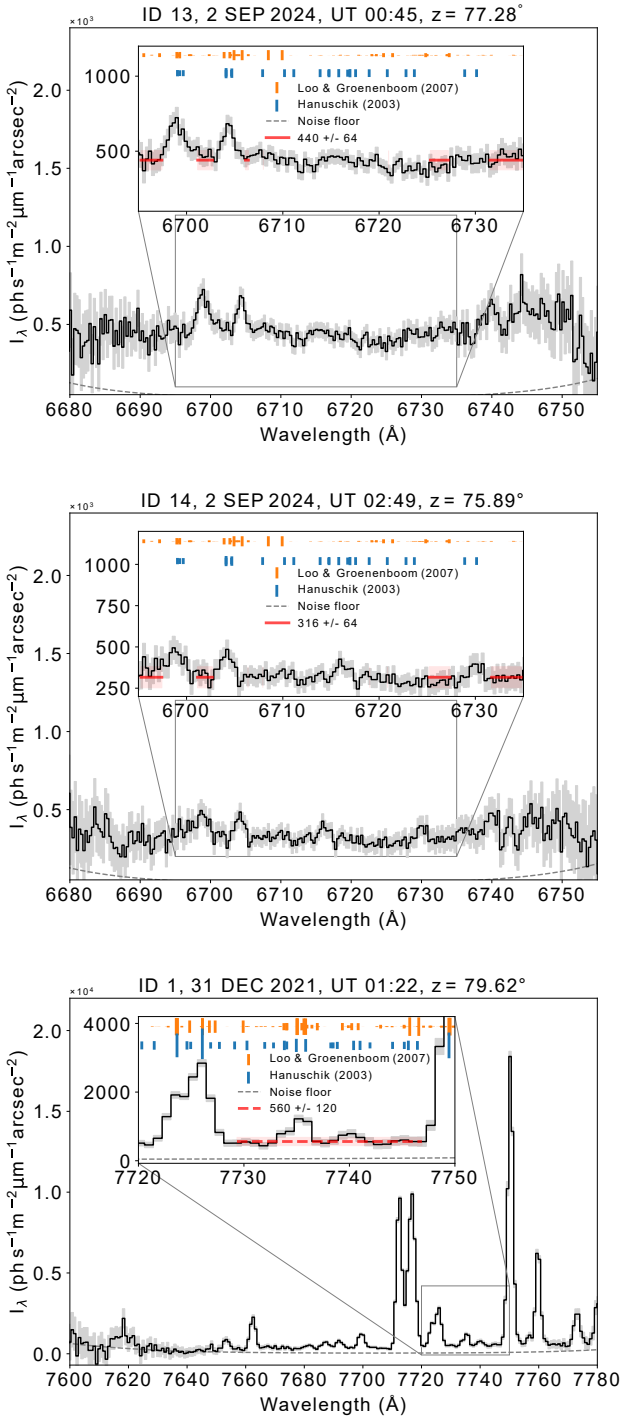

Fig. A.2. 6720 Å band spectra continued, along with apparent airglow radiance in the 7700 Å band. No clean spectral region is found without known lines or atmospheric absorption features. An upper limit on the continuum radiance is derived from regions free from O_2 absorption, which nonetheless contain unresolved spectral lines.

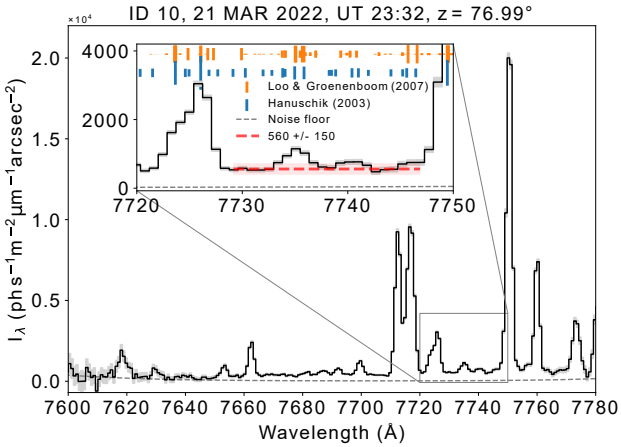

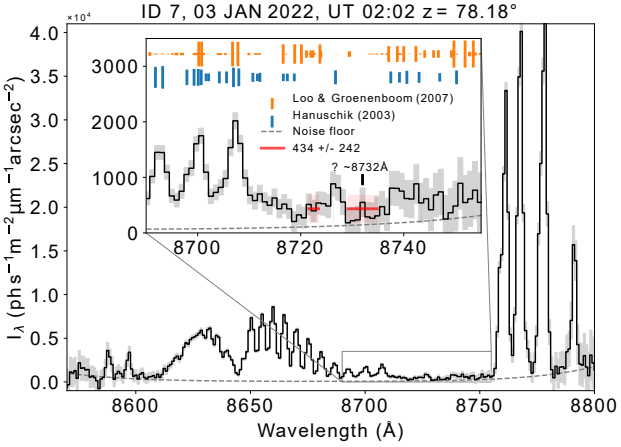

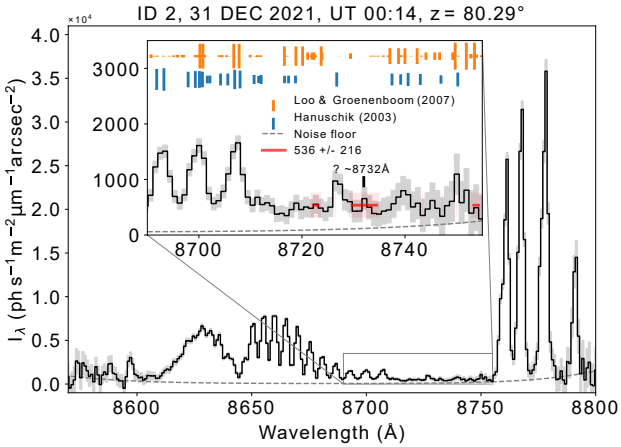

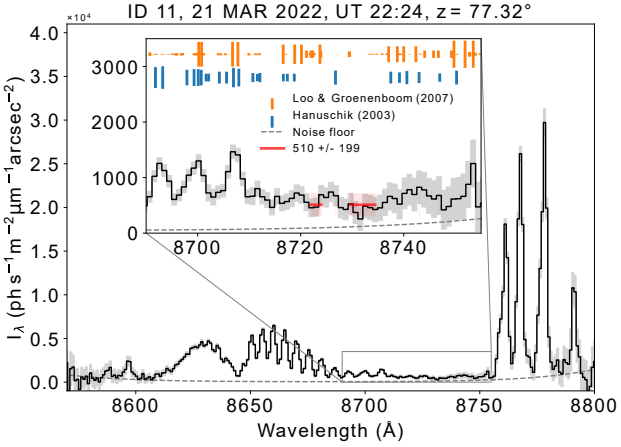

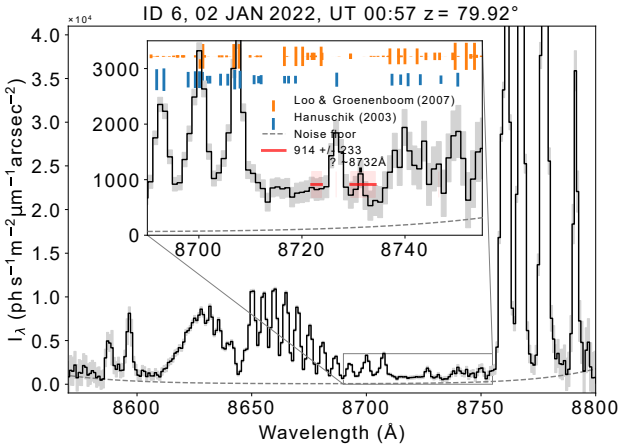

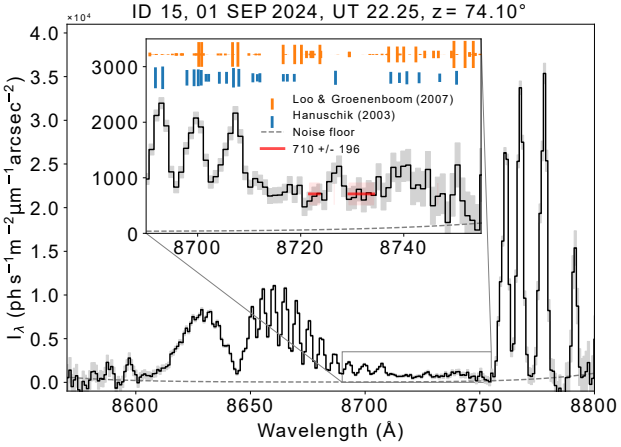

Fig. A.3. 7700 Å band airglow spectra continued. Apparent airglow spectra are shown in the 8700Å band.

Fig. A.4. Apparent airglow spectra in 8700Å band continued.

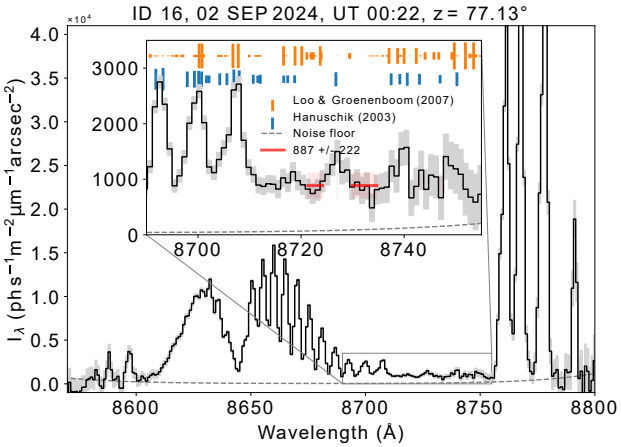

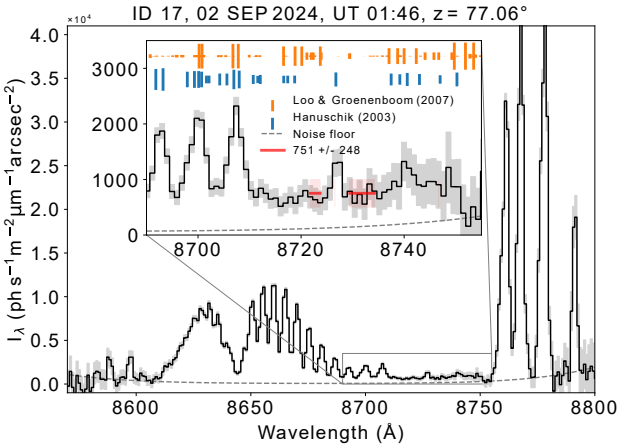

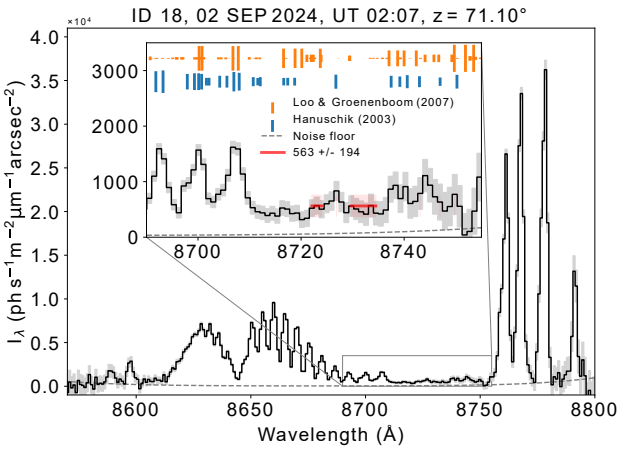

Fig. A.5. Apparent airglow spectra in the 8700Å band continued.

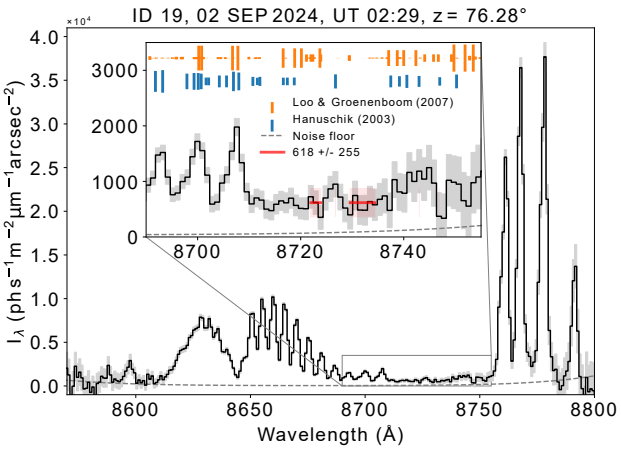

Fig. A.6. Apparent airglow spectra in the 8700Å band continued.

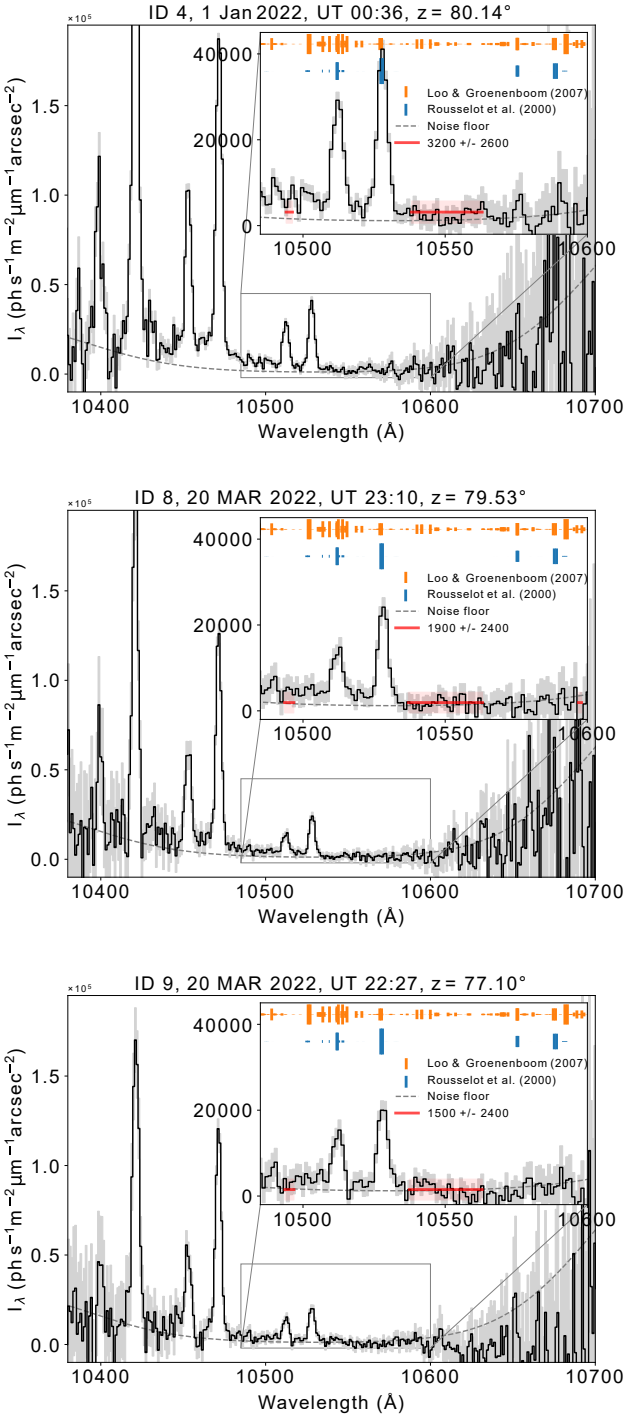

Fig. A.7. Apparent airglow spectra in the 10 500 Å band. Due to low system efficiency, the continuum in 10 500 Å is indistinguishable from the detector noise in all our spectra.

Appendix B: Previous studies and solar data

Table B.1. Compilation of NIR and SWIR airglow continuum measurements in the literature.

Publication	Continuum radiance		Wavelength / Band	R	OH Suppression	Date
	ph s^{-1}m^{-2}μm^{-1} arcsec^{-2}		Å / filter	$\lambda/\Delta\lambda$		
Noll et al. (2024)[4†]	375		16 550	4000 – 17 000	None	2009 – 2019
	140		10 500	— " —	— " —	— " —
	116		8700	— " —	— " —	— " —
	105		7700	— " —	— " —	— " —
	80		6700	— " —	— " —	— " —
Nguyen et al. (2016)[3]	751	± 4	11 913	320	NB filter	15 Feb 2013
Oliva et al. (2015)[1]	380		16 650	32 000	None	3 Sep 2014
	300		H	— " —	— " —	— " —
Trinh et al. (2013)[1]	560	± 120	15 200	2400	FBG	1–5 Sep 2011
Ellis et al. (2012)[1]	860	± 210	H	2400	FBG	1–5 Sep 2011
Sullivan & Simcoe (2012)[1]	670	± 200	16 650	6000	None	Mar 2010
	1017	± 19	H	— " —	— " —	— " —
	663	± 19	J	— " —	— " —	— " —
	508	± 19	Y	— " —	— " —	— " —
Tilvi et al. (2010)	162		10 630	1300	NB filter	1–6 Oct 2008
Venemans et al. (2009)	750		10 600	1000	NB filter	2–10 Nov 2006
Hanuschik (2003)[1]	335		8600-10 430	45 000	None	20–22 June 2001
	307		6720-8560	— " —	— " —	— " —
Cuby et al. (2000)[1]	2300		11 700	3000	None	Jan 2000
	1200		11 900	3000	None	— " —
Maihara et al. (1993b)[1]	590	± 140	16 650	1900	Mirror mask	Feb 1992
Sobolev (1978)[2]	296	± 64	10 612	12Å-mm, 9deg fov	— " —	late 1976
	144	± 57	9268	— " —	— " —	— " —
	280	± 94	8210	— " —	— " —	— " —
Noxon (1978)[2]	131	± 94/19	8570	N/A	None	15 Sep 1977
Gadsden & Marovich (1973)[4†]	56		7154	160	NB filter	— " —
	34		6754	240	— " —	— " —
Sternberg & Ingham (1972)[4†]	280	± 94	8200	N/A	None	18 Aug 1969
Broadfoot & Kendall (1968)[1†]	990	± 230	8700	~5000?	None	N/A
	200	± 70	7700	— " —	— " —	— " —
	103	± 15	6700	— " —	— " —	— " —
Krassovsky et al. (1962)	374		4000-7000	N/A	None	N/A

Notes. Additional studies exist at bluer wavelengths. Results are reported in various units in the original studies and are converted to match the units used in this work. Some of the values are obtained from figures, of which only a few are photocopied. [(†)]The authors report broader wavelength coverage, and the table are chosen to match the wavelengths studied in this work.[(1)]Apparent, [(2)]scaled to zenith, [(3)]ZL subtracted but not zenith scaled, [(4)]ZL subtracted and zenith scaled.

Table B.2. Space weather conditions at the time of observation.

Id	Solar wind speed	Solar wind density	Mag. field Bz	Solar X-ray flux	>10MeV protons	DRAO $F_{10.7}$
	km s^{-1}	cm^{-3}	nT	W m^{-2}	p$^+$ s^{-1} cm^{-2} sr^{-1} keV^{-1}	sfu
2	465±2	8.5±0.2	2.2±0.9	$2.69\pm0.02\times10^{-7}$	$3.8\pm2.6\times10^{-5}$	103.2
6	542±25	11.5±2.0	-2.7±3.8	$4.53\pm0.46\times10^{-7}$	$4.6\pm3.5\times10^{-5}$	93.3
7	524±4	13.1±1.0	2.5±1.8	$2.25\pm0.32\times10^{-7}$	$4.3\pm2.9\times10^{-5}$	88.3
11	522±8	10.2±1.0	-0.9±2.5	$8.17\pm0.41\times10^{-7}$	$13.6\pm6.9\times10^{-5}$	96.2
15	427±5	6.2±0.3	2.1±2.4	$5.11\pm0.65\times10^{-6}$	$5.2\pm2.5\times10^{-5}$	231.1
16	432±8	5.9±0.7	-0.7±0.8	$4.75\pm0.14\times10^{-6}$	$9.5\pm3.6\times10^{-5}$	231.1
17	446±3	7.5±0.4	2.8±1.1	$4.02\pm0.05\times10^{-6}$	$11.8\pm4.6\times10^{-5}$	231.1
18	451±7	7.7±0.5	2.5±0.9	$4.13\pm0.09\times10^{-6}$	$13.2\pm4.0\times10^{-5}$	231.1
19	433±3	6.4±0.3	-3.5±0.6	$5.06\pm0.40\times10^{-6}$	$13.0\pm5.5\times10^{-5}$	231.1

Notes. Bz in geocentric solar magnetic coordinates. DSCOVR and GOES data courtesy to National Oceanic (NOAO) and Atmospheric Administration Space Weather Prediction Center (SWPC). $F_{10.7}$ data courtesy of the DRAO.

Article III

KDP as a thermal blocking filter –
Deep infrared observations with warm narrow band filter

J. K. M. Viuho, A. A. Djupvik, A. N. Sørensen, D. Kumar, P. Steiner, J. P. U. Fynbo, S. Armas, and M. I. Andersen

Submitted to Publications of the Astronomical Society of the Pacific

arXiv preprint 2511.11806 [astro-ph.IM]

https://doi.org/10.48550/arXiv.2511.11806

Draft version November 18, 2025
Typeset using LaTeX **twocolumn** style in AASTeX7.0.1

KDP as a thermal blocking filter
Deep near IR observations with a warm narrow band filter

Joonas K. M. Viuho [1,2,3,4] Amanda A. Djupvik [3,4] Anton N. Sørensen [1,2] Daniel Kumar [5]
Peder Steiner [5] Johan P. U. Fynbo [1,2] Sergio Armas [3,4] and Michael I. Andersen [1,2]

[1] *Cosmic Dawn Center (DAWN)*
[2] *Niels Bohr Institute, University of Copenhagen, Jagtvej 155A, 2. floor, 2200 Copenhagen N., Denmark*
[3] *Nordic Optical Telescope, Rambla José Ana Fernández Pérez 7, ES-38711 Breña Baja, Spain*
[4] *Department of Physics and Astronomy, Aarhus University, Munkegade 120, DK-8000 Aarhus C, Denmark*
[5] *Ferroperm Optics A/S, Stubbeled 7, Trørød, DK-2950 Vedbæk, Denmark*

ABSTRACT

Ground-based astronomy suffers from strong atmospheric line- and thermal continuum emission, at the near infrared (NIR, 0.7–1.1 μm), and short-wave infrared (SWIR, 1.1–2.5 μm) wavelengths. The thermal continuum emission increases exponentially towards the red sensitivity cutoff of the state-of-the-art 2.5 μm cutoff SWIR detectors. Given availability of an optical quality shortpass filter material with strong blocking density in the SWIR, lower cost instrumentation, and higher performance filters could be designed. We demonstrate monopotassium dihydrogen phosphate (KDP, chemical formula KH_2PO_4) as a strong candidate for this purpose. KDP is fully transparent at wavelengths from ultraviolet to 1.3 μm, but becomes highly opaque at wavelengths >2 μm. We demonstrate on-sky use of KDP by improving performance of a cryogenic broadband filter with known off-band thermal leak, and using a non-cryogenic narrow band filter for deep observation. KDP reduces the sky background by 4.5 magnitudes in the leaky Z-band filter we use. Our 4 nm wide, central wavelength 1.191 μm narrowband filter in combination with KDP reduces the sky surface brightness by three magnitudes compared to a J broadband. We find a sky surface brightness of 18.5 mag arcsec^{-2} at 1.191 μm, and interpret it as the airglow continuum. KDP is an excellent thermal blocker, when its temperature is maintained above its Curie point at 123 K. Below Curie point, KDP transforms its crystal structure, degrading its otherwise good imaging properties.

Keywords: Near infrared astronomy (1093) — Astronomical instrumentation (799) — Astronomical optics (88) — Optical filters (2331) — Diffuse radiation (383)

1. INTRODUCTION

The near infrared (NIR) to short-wave infrared (SWIR) wavelength range is ideal for studying the early universe, for example, at redshifts above ~ 6, the Lyman break falls in this region. Designing highly efficient ground-based instrumentation in this wavelength range is a challenge due to atmospheric and instrumental thermal radiation, and lack of an ideal photodetector. Silicon has a band gap at 1.14 eV limiting the use of silicon based detectors to wavelengths shorter than 1.1 μm. While Germanium detectors with a cutoff at 1.8 μm exist, they typically exhibit high dark current, making them unusable for faint object photometry and spectroscopy. Mercury-Cadmium-Telluride (HgCdTe) SWIR detectors exist with multiple cutoff wavelengths, but the state-of-art version have the cutoff at 2.5 μm, and are consequently sensitive to ambient thermal emission. The use of these 2.5 μm cutoff detectors mandates a fully cryogenic instrument design, leading to increased design complexity and cost, making them viable only for the largest observational facilities.

The use of Potassium Dihydrogen Phosphate (KDP, KH_2PO_4) for blocking thermal radiation has been suggested in the literature: to let the 2.5 μm cutoff detectors be used without a cryogenic optical train (P. J. Amado et al. 2012). We have not seen a study applying KDP as a thermal radiation blocking filter in the context of astronomical observations. In this work, we will do exactly that and report on our findings. KDP and its deutered variant Potassium Dideuterium Phosphate

Corresponding author: Joonas K. M. Viuho
Email: joonas.viuho@nbi.ku.dk

(D-KDP, $K_2D_2PO_4$) are commonly used non-linear optical crystals in laser frequency modulation. Historically, KDP and D-KDP have been studied extensively in the context of high-power lasers for fusion power (D. Eimerl 1987; J. J. De Yoreo et al. 2002). In addition to the D-KDP, KDP has a few other isomorphic crystals, which share similar physical properties.

One of the unique physical properties of KDP is its high absorbance in the SWIR wavelength regime, and very high transmission from UV to 1.3 μm (Fig. 1), making it an excellent thermal radiation blocking filter. This is notable since only a few optical materials exist that absorb in the thermal infrared, while transmitting in VIR–NIR range (D. Eimerl 1987; M. J. Weber 2020). Available thermal radiation absorbing glasses do not offer nearly as high optical density (OD) in the SWIR and they also absorb at shorter wavelengths, making them less ideal as short-pass filters. KDP's isomorphic crystals (Table 1) show similar properties of being practically fully transparent at wavelengths shorter than their shortpass cutoff wavelength, and very high optical density at wavelengths longer than their cutoff wavelength. Several immediately interesting use cases can be realized, including:

- NIR and SWIR instrumentation where a 2.5 μm cutoff detector is placed in a cryostat, while the entire optical train is maintained in ambient temperature (similar to current instrumentation with silicon photo-detectors).
- Enhanced broad-, and especially, narrowband filter designs for the NIR and SWIR wavelengths as the dielectric coating is not required to block wavelengths >2 μm.
- Immediate performance improvement on existing systems suffering from thermal light leaks.
- Heat blocking from on-the-line-of-sight warm optical components, such as optical fibers, or silicon waveguide optics.

In this work, we demonstrate the thermal blocking capabilities by improving photometric performance of existing thermally leaking optical system, and we design a custom warm (ambient temperature) narrow-band (NB) filter to operate in conjunction with the KDP window.

2. EXPERIMENTAL SETUP

We used the Nordic Optical Telescope's (NOT) NOTCam instrument (T. M. Abbott et al. 2000) as a test bed. NOTCam is an imager-spectrograph designed to operate in the SWIR wavelength region including the K band. It has a hemispherical entrance baffle, and a cold Lyot stop limiting off-axis thermal background. The instrument temperature is at 73 K. NOTCam has an aperture wheel, two filter wheels, a stop wheel, and a grism wheel (Fig. A1). We use the filter wheels for mounting the broadband filters, and the aperture wheel for mounting the KDP window. Additionally, the warm narrowband filter was installed in front of NOTCam's cryostat window in the telescope converging beam, i.e. in fully ambient, non-cryogenic conditions.

2.1. *KDP*

KDP and its deutered variant, D-KDP, are commonly used for frequency modulation in NIR lasers. Possibly, most well known, KDP and D-KDP have been used in the high power lasers of the National Ignition Facility at Lawrence Livermore National Laboratory (J. J. De Yoreo et al. 2002). KDP can be grown to large size, growing it is relatively quick, and it can be polished to optical quality, making it a low cost and easy to work with optical material. KDP crystals can be doped with different impurities, and research on KDP continues today in the field of solid state dye lasers.

Isomorphic crystals of KDP include Ammonium- (ADP), Rubidium- (RDP) and Cesium- (CDP) Dihydrogen Phosphates, and similarly, Potassium (KDA), Arsenic- (ADA), Rubidium (RDA) and Cesium (CDA) arsenates, and their deutered counterparts (e.g. Ammonium Dideuterium Phosphate, D-ADP). KDP and its isomorphisms are polymorphic crystals which exhibit interesting dielectric and non-linear optical properties. We will focus on two of their physical properties: the spectral transmission, and the Curie temperature T_C.

KDP and its isomorphisms are nearly completely opaque in the thermal infrared, while being fully transparent at wavelengths shorter than 1.3 μm (D. Eimerl 1987), making them ideal short-pass 'filter glasses', thermal blockers, for NIR filter design. Being polymorphic crystals, KDP and its isomorphisms change from paramagnetic to ferromagnetic state when cooled below their T_C. Cooling them below T_C also changes the crystal structure, which in turn introduces unwanted optical qualities: at temperatures below the T_C, we see position-dependent transmission non-uniformity and possible polarization-induced point spread function distortions with our z-cut KDPs (Fig. 2). We have observed similar phase-transition effects in both KDP and D-DKP.

Because of the phase transition, KDP and its isomorphs have to be operated above their T_C to maintain the desired optical qualities. In return, this poses a trade-off between the external thermal flux absorbed by

the crystal, and the thermal flux emitted by the crystal itself. The T_C is a key property to balance the trade-off. This generally favors materials with lower T_C for SWIR astronomy applications, suggesting the most promising materials to be KDP, KDA and RDA. We summarize the KDP isomorphisms and their Curie temperatures, and approximate short-pass cutoff wavelengths (λ_{SP}) in Table 1. We refer to the optical and mechanical properties of KDP reported by C. C. Stephenson & J. G. Hooley (1944); F. Zernike (1964); D. Eimerl (1987); W. M. Haynes et al. (2016); M. J. Weber (2020).

We purchased three z-cut KDP and one D-KDP crystal from United Crystals Inc. for this study. Two Ø25 mm diameter and 4 mm thick KDPs, and one Ø25 mm diameter and 4 mm thick D-KDP were already purchased in 2016. The first observations followed soon after. The phase transition at T_C was not immediately understood, and the project fell dormant for a while for that reason. When it became clear that the change in optical properties was due to the phase transition, calculations were done on the reachable equilibrium temperature inside NOTCam (Sec. 4.2). A third Ø10 mm diameter and 0.5 mm thick KDP window was purchased and used for the observations reported in this work.

The KDPs and the D-KDP were installed in NOTCam's aperture wheel (Fig. A1). The 4 mm thick KDPs and the D-KDP were installed in thermal contact with the instrument, while 0.5 mm thick KDP was prepared with a thermally insulating glass fiber holder. The KDPs in the aperture wheel are placed in the focal plane of the telescope, allowing us to warm the thermally insulated KDP above the T_C by the thermal radiation from the vacuum window (Sec. 4.2).

2.2. *The warm narrow-band filter*

Manufacturing high performance interference filters is challenging and expensive, and a trade-offs between peak efficiency, in-band transmission, and off-band blocking must be made. In the SWIR, a large spectral range is covered, leaving observations vulnerable to off-band, usually thermal, leaks. The off-band contribution can be significant, especially in narrow-band photometry, where the flux in the band-pass is weak, degrading the photometric performance. Due to the ability of KDP to absorb thermal radiation, filters with band-passes shorter than 1.3 μm may be placed in ambient (warm) conditions. A KDP thickness of 1 mm is sufficient to absorb thermal emission from the 'warm' filter, to a level that has no impact on the observations.

We designed a custom warm NB filter, to demonstrate this. The filter is designed to be used in combination with the NOTCam the J-band filter and a 0.5 mm KDP. The NB filter is only blocking off-band light through the J-band (Fig. 3). The NB filter has a central wavelength of 1.191 μm, and full-width-at-half-maximum of ∼4 nm (R∼300), being located in the largest gap between atmospheric hydroxyl (OH) emission lines within the J band. The filter was designed and manufactured by Ferroperm Optics A/S. We will refer it as BP1191-4.

The BP1191-4 filter is based on a Fabry-Pérot type design with four cavities having a theoretical bandwidth of 4.2 nm on the front surface of a Borofloat 33-substrate. A stress compensating anti-reflection coating was added on the rear surface to increase the transmission. The filter was manufactured in a Generation III Helios 800-chamber, employing the Plasma Assisted Reactive Magnetron Sputtering (PARMS) coating technology. Niobium pentoxide, Nb_2O_5, was used as a high refractive index and silicon dioxide, SiO_2, as a low refractive index material. The monitoring strategy of the bandpass filter was direct monitoring at the center wavelength on a Borofloat 33-substrate utilizing the self-compensating turning point method (P. W. Baumeister 2004). The result of the production coating runs was a 1191 nm filter with a bandwidth of 3.9 nm and a peak transmission of 94% measured on a Perkin Elmer L1050 -spectrophotometer (Fig. 3).

2.3. *Broad-band filters*

The NOTCam broadband J, H, K filters were ordered as a part of the Mauna Kea Observatories near-infrared (MKO-NIR) set and have well defined bandpasses (D. A. Simons & A. Tokunaga 2002; A. T. Tokunaga et al. 2002; A. T. Tokunaga & W. D. Vacca 2005). Two copies of the filters exist at the NOT: one installed inside NOTCam, and another stored in a clean-room outside of the instrument. For this study, we scanned the spare J-band filter, using a Perkin-Elmer L1050 -spectrophotometer at Ferroperm Optics A/S in Vedbæk, Denmark. The spectral range 0.3 μm to 2.7 μm was covered, with the motivation of understanding the off-band blocking characteristics of the filter.

NOTCam's Z- and Y-band filters were intended to have the corresponding UKIDSS bandpasses (P. C. Hewett et al. 2006). The filters were not manufactured accordingly however, and especially the Z-band filter has pour off-band blocking. The Z and Y band filters were scanned at the Instituto Astrofisica de Canarias (IAC) in range 0.3 μm to 2.6 μm. The Z-band filter was confirmed to have a significant thermal leak (Fig. 4), making it an ideal optical component for demonstrating the performance of KDP as a thermal blocker.

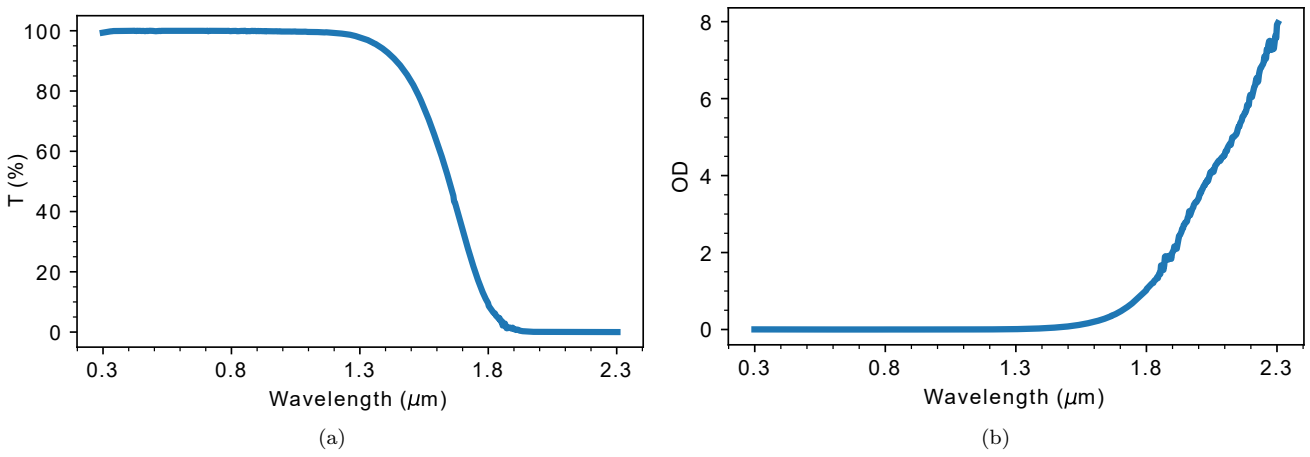

(a) (b)

Figure 1. Internal transmission (a) and optical density (b) for unpolarized light through 1 mm crystal.

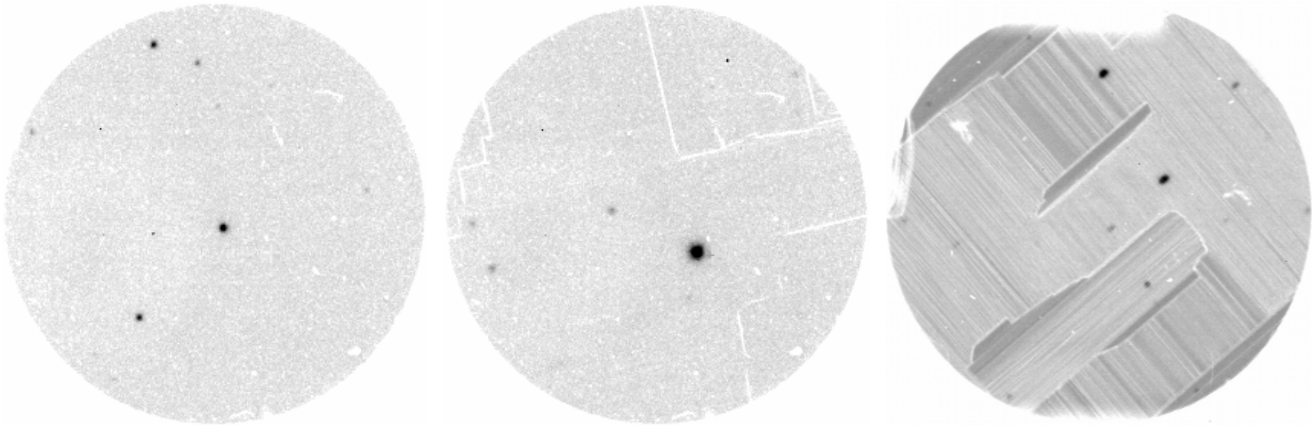

(a) (b) (c)

Figure 2. The effect of T_C on the KDP photometric performance. (a) $T_{KDP} > T_C$ no structure present, (b) $T_{KDP} \sim T_C$ partial transmission effects, and (c) $T_{KDP} < T_C$ strong variation in transmission and PSF distortions. The panels (a) and (b) show a 0.5 mm thick KDP, while the (c) shows a 4 mm thick KDP.

2.4. *Detector*

NOTCam is equipped with a 1024 × 1024 × 18.5 μm pixel HgCdTe/Al_2O_3 HAWAII PACE I -detector with a cutoff at 2.5 μm (L. J. Kozlowski et al. 1994), which is controlled by a Brorfelde Image Acquisition System (BIAS) -controller (J. Klougart 1995). With the NOTCam wide-field camera, the detector covers a $4' \times 4'$ area on sky. The BIAS controller offers two read modes, 1.) reset-read-read (correlated double sampling), and 2.) ramp-sample (non-destructive readout with specified time interval). Due to controller-related specifics not known to us, images from the NOTCam detector show more complex DC structure than other similar detectors. The phenomena is related to the first few reads, and in case of ramp-sampling data can be circumvented by re-fitting the ramps in postprocessing: instead of using the controller provided ramp-sample fits, we have re-fit all data used in this work, ignoring the first read in a sequence.

All four quadrants share the same DC structure, but have slightly differing noise and gain characteristics. Readout noise in a correlated double sampling is 3-4 ADU, depending on the quadrant. Furthermore, NOTCam shows varying quasiperiodic pickup noise with peak-to-peak amplitude up to ∼20 ADU depending on the exposure. NOTCam dark frames have two distinct components: *i.)* amplifier and shift register glow dependent on number of reads, and *ii.)* an integration time dependent uniform diffuse dark current with rate of ∼0.01 ADU s^{-1} px^{-1} over the image area. The regis-

Table 1. Curie temperatures T_C and cut-off wavelengths λ_{SP} of KDP and its isomorphisms

	KDP	D-KDP	KDA	D-KDA	ADP	D-ADP	ADA	RDP	D-RDP	RDA	D-RDA	CDA	D-CDA
T_C (K)	123	223	95	159	147	241	216	147	218	110	173	143	241
$\lambda_{SP,o}$ (μm)	1.4	1.7	1.6[a]	1.9[a]	1.2[a]	1.5	1.2	1.4	1.6	1.4	1.7	1.4	1.6
$\lambda_{SP,e}$ (μm)	1.6	>2				1.5	1.2	1.6	1.6	1.6	1.9	1.7	1.7

[a]Unpolarized light.

References—(D. Eimerl 1987)

NOTE—Curie temperatures T_C and cutoff wavelengths for ordinary $\lambda_{SP,o}$, and extraordinary $\lambda_{SP,e}$ beam have been collected from D. Eimerl (1987), and are measured for 11 mm thick samples. We define the λ_{SP} as a 50% falling edge on the transmission curve. D-* indicates the deutered variants of Potassium (K), Arsenic (A), Rubidium (R), and Cesium (C) phosphates (P), and arsenates (A).

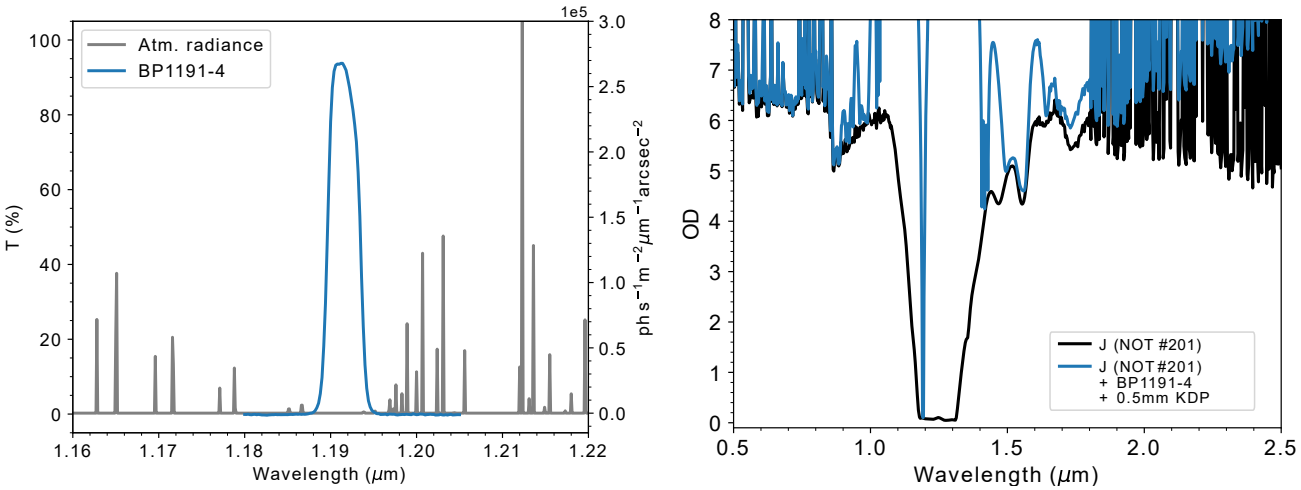

Figure 3. BP1191-4 filter characteristics. Transmission and sky radiance (a), and off-band optical density (b). The bandpass has a 4 nm full-width-at-half-maximum, and it is centered at 1.191 μm.

ter and amplifier glow is shown in Fig. A2, and it mainly affects areas at the detector edges.

Unlike typical SWIR observations, we are detector noise limited in the shorter integrations in the BP1191-4 bandpass. With the BP1191-4 filter, we readout the detector in ramp-sampling mode with 14 samples per integration, and in all broadbands, with as many 4 s sub-reads as it is possible while keeping the total integration within the 1% linearity limit of the detector. We do not have a measure of the inter-pixel capacitance (A. C. Moore et al. 2006), and to avoid uncertainty in the gain conversion by determining, and applying, all zeropoints in terms of Analog-to-Digital-Units (ADUs). NOTCam gain measured with the photon transfer tech (J. R. Janesick et al. 1987) is $\sim$2.6 e$^-$ ADU^{-1}. We use this gain value when estimating the thermal flux from KDP.

3. OBSERVATIONS

We summarize our observations in Tables 2 and 3. Initial observations with the 4 mm thick KDPs were already carried out early in 2016. Results from the observing run were only published on the NOT's website since the data were not clearly understood[1]. There was a confusion regarding the cause of the changed crystal

[1] https://www.not.iac.es/instruments/notcam/staff/kdp-tests.html

Table 2. Observing conditions

Night of	Seeing	Dust	Temp.	Rel. humidity	Moon conditions
	$''$	μg m^{-3}	°C	%	
2025 Jan 14	1.2	0.1	9	7	Bright
2025 Jan 15	1.0	0.1	5	<1	Bright
2025 Jun 30	0.5	0.1	16	<1	Dark
2025 Aug 8	0.6	45	17	38	Bright
2025 Aug 23	0.9	15	17	75	Dark

structure, which had severely affected photometry. At first it was thought that the KDP had fractured during cool down; we only later found out that the structure was due to the phase transition, when the instrument was warm cycled for service. In 2016, the KDP was found to significantly suppress the sky background in the leaky Z-band, prompting further study.

A second observing campaign was started in 2025, after the thermally insulated 0.5 mm KDP window was installed in NOTCam. Sky conditions on 2025 January 14 and 15 were excellent. New observations were done when the BP1191-4 filter became available in 2025 June. The BP1191-4 bandpass is bue enough that scattered Moon light would affect observations, thus they have to be obtained under dark sky conditions. The observations on 2025 June 30 were made under excellent conditions. The fields observed in BP1191-4 were re-observed in J band on 2025 August 8, but these observations suffered from large amounts of Saharan dust, so called "Calima". Since the 2025 June 30 observations were detector systematics limited (Sec. 2.4), one more set of BP1191-4 observations was made on 2025 August 23, unfortunately also suffering from Saharan dust.

4. ANALYSIS AND RESULTS

4.1. *KDP transmission and optical density*

When considering filter transmission curves, transmission is the relevant term in-band, while optical density (OD) is the relevant term off-band. Thus we show graphs of both transmission and optical density. Optical density is related to transmission T via

$$\mathrm{OD} = -\log_{10}(T) \tag{1}$$

The optical density of KDP was measured at Ferroperm Optics with the PerkinElmer-L1050 spectrophotometer, at ambient temperature within the wavelength range of 0.300 μm to 2.315 μm using unpolarized light. Data from scans of a 4 mm (<1.86 μm) and a 0.5 mm (>1.86 μm) thick samples were combined to yield the equivalent optical density of 1 mm KDP and is presented in Fig. 1 and Tables B1, and B2. The KDP samples were removed from their vacuum bags just before the scan in order not to expose them to humidity. The instrument was null calibrated prior to the measurements. Additionally, the KDP internal transmission was calculated from relative photometry, and is in agreement with the spectrophotometer scans (Table 4).

4.2. *KDP equilibrium temperature and operating point*

For KDP, T_C=123 K. Consequently, when placed inside NOTCam at T_{inst}=73 K, KDP undergoes the Curie transition from paramagnetic to ferromagnetic, which also changes its crystal structure. At least, in the case of our z-cut KDPs, the imaging characteristics of the KDP become worse in the ferromagnetic state. Strong position dependent variability in transmission and point spread function distortion (possibly due to polarization effects) appear below T_C, making KDP unusable for high quality photometry, unless it is heated to a temperature above T_C.

In order to warm up KDP above its T_C, we move it into the telescope beam where it is exposed to ambient thermal radiance. We find the equilibrium temperature of our thermally insulated 0.5 mm KDP using Stefan-Boltzmann's law, assuming that all energy transfer is radiative. The radiance L of a blackbody given by Stefan-Boltzmann's law is

$$L = A\epsilon\sigma T^4 \int \Omega \tag{2}$$

where A is the surface area, ϵ the emissivity, σ the Stefan-Boltzmann constant, T the temperature of the blackbody, and Ω the solid angle. On the front side of the KDP, we take typical summer night time ambient temperature T_{amb}=288 K which arrives from a solid

Table 3. Table of observations

Standard		Band	Ref.	Date	Start	Integration	Airmass	Aerosols	zp	Sky surface
			mag.		time	time		total	ADU s^{-1}	brightness
Name	FS		m		UT	s	X	μg m^{-3}	m	mag arcsec^{-2}
RL 149	14	K	11.459	2025 Jan 15	03:00	5×(8×4s)	1.33	0.12	22.34±0.00	12.48
		H	11.438	2025 Jan 15	03:06	5×(8×4s)	1.35	0.12	22.92±0.00	13.57
		J	11.444	2025 Jan 15	02:44	5×(8×4s)	1.28	0.12	22.97±0.00	15.59
		Y	11.402	2025 Jan 15	02:49	5×(8×4s)	1.30	0.12	22.77±0.00	16.63
		Z	11.317	2025 Jan 15	02:54	5×(8×4s)	1.31	0.12	22.37±0.00	12.91
		K+KDP	11.459	2025 Jan 15	03:17	5×(8×4s)	1.33	0.05	15.10±0.17	12.32
		H+KDP	11.438	2025 Jan 15	03:12	5×(8×4s)	1.37	0.05	22.39±0.00	13.63
		J+KDP	11.444	2025 Jan 15	02:16	5×(8×4s)	1.22	0.06	22.83±0.00	16.77
		Y+KDP	11.402	2025 Jan 15	02:10	5×(8×4s)	1.21	0.06	22.51±0.00	16.82
		Z+KDP	11.317	2025 Jan 15	02:04	5×(8×4s)	1.20	0.06	22.25±0.00	17.42
GD 71	12	H	13.805	2025 Jan 16	02:06	5×(5×4s)	1.30	0.08	22.87±0.01	13.87
		J	13.710	2025 Jan 16	02:02	5×(5×4s)	1.28	0.08	22.90±0.01	15.66
		Y	13.657	2025 Jan 16	01:58	5×(5×4s)	1.27	0.08	22.65±0.01	17.04
		Z	13.398	2025 Jan 16	01:53	5×(5×4s)	1.25	0.08	22.32±0.01	13.08
		H+KDP	13.805	2025 Jan 16	01:35	5×(5×4s)	1.19	0.08	22.42±0.01	14.22
		J+KDP	13.710	2025 Jan 16	01:40	5×(5×4s)	1.21	0.08	22.81±0.01	15.88
		Y+KDP	13.657	2025 Jan 16	01:45	5×(5×4s)	1.22	0.08	22.62±0.01	17.43
		Z+KDP	13.398	2025 Jan 16	01:49	5×(5×4s)	1.24	0.08	22.27±0.01	18.19
GSPC	–	H	11.585	2025 Jan 16	00:22	5×(4×4s)	1.13	0.05	22.92±0.00	14.02
P545-C		J	11.841	2025 Jan 16	00:26	5×(4×4s)	1.14	0.05	22.97±0.00	15.68
		Y	12.031	2025 Jan 16	00:30	5×(4×4s)	1.15	0.05	22.63±0.01	16.68
		Z	12.049	2025 Jan 16	00:34	5×(4×4s)	1.15	0.05	22.26±0.01	13.80
		H+KDP	11.585	2025 Jan 16	00:50	5×(4×4s)	1.18	0.05	22.51±0.00	14.21
		J+KDP	11.841	2025 Jan 16	00:46	5×(4×4s)	1.18	0.05	22.85±0.00	15.82
		Y+KDP	12.031	2025 Jan 16	00:42	5×(4×4s)	1.17	0.05	22.52±0.01	16.91
		Z+KDP	12.049	2025 Jan 16	00:38	5×(4×4s)	1.16	0.05	22.26±0.01	17.52
GSPC	121	H	11.436	2025 Jan 16	00:54	5×(5×4s)	1.21	0.05	22.97±0.00	14.08
S772-G		J	11.984	2025 Jan 16	00:59	5×(5×4s)	1.21	0.05	22.96±0.00	15.81
		Y	12.464	2025 Jan 16	01:20	5×(5×4s)	1.21	0.05	22.71±0.01	17.21
		Z	12.735	2025 Jan 16	01:06	5×(5×4s)	1.22	0.05	22.44±0.01	13.24
		H+KDP	11.436	2025 Jan 16	01:24	5×(5×4s)	1.21	0.05	22.45±0.00	14.21
		J+KDP	11.984	2025 Jan 16	01:20	5×(5×4s)	1.21	0.05	22.85±0.00	15.89
		Y+KDP	12.464	2025 Jan 16	01:16	5×(5×4s)	1.21	0.05	22.61±0.01	17.41
		Z+KDP	12.735	2025 Jan 16	01:11	5×(5×4s)	1.22	0.05	22.28±0.01	18.25
GSPC	151	J	12.211	2025 Aug 9	00:31	5×(4×4s)	1.01	40	22.64±0.01[a]	15.66[b]
P340-H		J+BP1191-4	12.211	2025 Jul 1	03:01	9×(14×5s)	1.01	0.1	18.65±0.04	18.52
		J+BP1191-4+KDP	12.211	2025 Jul 1	02:48	9×(14×5s)	1.02	0.1	18.57±0.05	18.73
		J+BP1191-4	12.211	2025 Aug 23	22:14	4×(14×50s)	1.11	21	18.79±0.04[a]	18.18[b]
		J+BP1191-4+KDP	12.211	2025 Aug 23	21:24	4×(14×50s)	1.24	18	18.45±0.05[a]	18.10[b]
GSPC	141	J	11.152	2025 Aug 8	22:19	5×(4×4s)	1.01	23	22.58±0.00[a]	15.69[b]
P389-D		J+BP1191-4	11.152	2025 Jul 1	02:25	9×(14×5s)	1.13	0.08	18.76±0.02	18.54
		J+BP1191-4+KDP	11.152	2025 Jul 1	02:08	9×(14×5s)	1.09	0.08	18.67±0.02	18.63

[a] Dusty observing conditions.

[b] Dusty observing conditions, zeropoint applied from another night.

References—Gemini UKIRT MKO photometric standard stars catalogue, S. K. Leggett et al. (2006).

Note—Magnitudes given in the Vega system. The second column indicated the Faint standard (FS) -catalogue number.

angle visible through NOTCam's entrance baffle, projected through the collimator optics $\Omega_{f,1}$ defined by a cone with semi-angle θ as

$$\Omega_{f,1} = 2\pi\,(1 - \cos(\theta)) \tag{3}$$

where the semi-angle θ is derived from the baffle opening angle, with a diameter of Ø53 mm and a distance of 68 mm to the KDP. The remaining half hemisphere $\Omega_{f,2} = 2\pi - \Omega_{f,1}$ sees the cold instrument with the cryostat temperature T_{inst}=73 K. On the rear side, the KDP is exposed to a half hemisphere Ω_r with temperature T_{inst} (Fig. A1). We get the radiant power $P = L/A$, or

$$P = \epsilon\sigma \left(T_{amb}^4 \int_{\Omega_{f,1}} d\Omega + T_{inst}^4 \int_{\Omega_{f,2}} d\Omega + T_{inst}^4 \int_{\Omega_r} d\Omega \right), \tag{4}$$

and solve for the equilibrium temperature KDP T_{KDP} getting,

$$T_{KDP} = T_{inst} + \frac{mP}{c_m(T)\rho V M}\Delta t, \tag{5}$$

where P is the total radiant power (Eq. 4), M=136.086 molecular weight of KDP, ρ=2.338 g cm^{-}3 the density of KDP (W. M. Haynes et al. 2016), and c_m the molar heat capacity as tabulated by C. C. Stephenson & J. G. Hooley (1944). Assuming the emissivity to be unity, we find that it takes about 20–35 min to warm the 0.5 mm thermally insulated KDP above its T_C, and make the unwanted structure to disappear (Fig. A4). Given T_{amb}=288 K we find the KDP to reach an equilibrium temperature of ∼150 K when left in the beam.

4.3. *Data reduction*

Observations consisted of either 5-point or 9-point skewed dither-patterns with 10–15″ offsets between two consecutive integrations. All data were recorded as ramp-sampling integrations (Sec. 2.4). The broadband standard star fields were recorded with a sample time of 4 s with a number of samples yielding a total integrated flux within the 1% linearity range of the detector. The NB integrations had very low flux levels and were readout with the maximum 14 ramp-samples available. All sub-reads are stored, and we re-fit to the sub-reads ignoring the first read in a ramp-sample sequence. In the NOTCam data, the first line and row of each detector quadrant reads out as value 0. These together with hot and cold pixels were removed by bilinear interpolation based on the surrounding pixel values.

The images were then sky subtracted, aligned, and coadded with 'notcam.cl' reduction package (priv. comm. A. A. Djupvik, T. Reynolds)[2] written for Image Reduction and Analysis Facility (IRAF) (D. Tody 1986, 1993). The first image recorded for each dither-pattern was rejected from the co-addition. For the sky level being very low in the narrowband images, the NB images were additionally co-added without sky subtraction for estimating the sky level, and the instrumental background in case of KDP observations. Isophotal fluxes of the standards stars were extracted, and extinction corrected using the standard extinction coefficients adopted in the NOT's signal-to-noise calculator extinction coefficients ($\kappa_Z = 0.05$, $\kappa_Y = 0.07$, $\kappa_J = 0.09$, $\kappa_H = 0.07$, $\kappa_K = 0.08$ mag arcsec^{-2}). We derive the zeropoints in units of ADU s^{-1} from the photometric nights (January 14, January 15, and June 30), and apply them to the sky surface brightness measurement of all nights. We have not derived color terms for the BP1191-4 filter, and use the J-band magnitudes for relative photometry in the BP1191-4 bandpass.

4.4. *Instrumental background*

The Ø10mm diameter KDP vignettes the NOTCam wide-field camera's 4′×4′ field-of-view to a Ø1.1′ image circle allowing us to sample detector area that is not exposed to the sky (Fig. A2). We do not see a difference between the non-illuminated areas in the on-sky KDP exposures shutter open, and the dark exposures shutter closed in the Y- and J-band images. However, with the filters which pass thermal IR Z (thermal leak), H (transmits partially), and K (transmits fully), a light leak from the adjacent open aperture wheel position can be seen in the KDP exposures (Fig. A2). We conclude that the black surface treatment is absorbing at the bluer wavelengths, but becomes reflective in the thermal infrared. The fiberglass holder is slightly transparent in the K band (Fig. A2). The transmission can be seen in the Z- and H-band observations if inspected carefully. Apart from the leak in the aperture wheel, the fiberglass holder, and detector dark current, we do not observe any other instrumental contribution in our KDP integrations, and do not expect any thermal emission from within the instrument to reach the detector.

4.5. *Thermal emission from the KDP*

The KDP itself is a thermal emission source. It is placed in the aperture wheel which is re-imaged on the detector plane. We estimate the KDP to reach a temperature of ∼150 K when placed in the beam. According to our calculations this results to a flux of ∼2×10^{-4} ADU s^{-1} px^{-1} on the detector when viewed

[2] www.not.iac.es/instruments/notcam

through the F/5.8 wide-field camera. The resulting flux is negligible compared to the sky flux we measure. In order for the KDP to emit a comparable amount to the sky flux, the KDP window would need to reach a temperature of 177 K, or higher, which we do not consider possible.

4.6. *The effect of persistence and reciprocity failure*

We do not have a sophisticated model available for correcting persistence and reciprocity failure (S. Tulloch et al. 2019). We do see a power law decay of the background level, in the non-illuminated detector areas in our KDP integrations. We attribute the exponential decay to persistence, and subtract it out as a parasitic signal. Additionally, in case of the long BP1191-4 integrations we see spatial correlation in our sky images with the location of the brightest stars. The full field-of-view in the observations without KDP allows us to find a sky area which has not been visited by a star in the last few frames. However, in the integrations with the KDP, the usable image area is significantly smaller (Fig. A2), restricting the sky are to be measured in the proximity of the field stars. If the effect in the BP1191-4 observations with and without KDP is similar, this could lead us to over estimate the sky surface brightness by ∼15% in the narrowband KDP observations.

4.7. *Airglow continuum at 1.191 μm*

Depending on the night, we measure a sky surface brightness of 18.1–18.7 mag arcsec^{-2}, or 640–1100 ph s^{-1}m^{-2}μm^{-1}arcsec^{-2} in the BP1191-4. All of the BP1191-4 observations have been made under dark Moon conditions. On 2025 June 30, the Moon had set 1.5 h before the beginning of observations, and on 2025 August 23 was new Moon.

To isolate the atmospheric continuum emission background, we calculate the zodiacal light brightness for our pointings with the InfraRed Science Archive (IRSA), Infrared Processing & Analysis Center (IPAC) Euclid background model calculator Version 1[3]. The calculator is based on the zodiacal light model of T. Kelsall et al. (1998). Both of the standard star fields observed in the BP1191-4 bandpass are located approximately at ecliptic latitude of b_{ec}=45°, and the zodiacal light contributes only 35–40 ph s^{-1}m^{-2}μm^{-1}arcsec^{-2}, or ∼21.8 mag arcsec^{-2}, which is much less than the sky surface brightness we measure.

In order to estimate the off-band sky light not rejected by our filter setup, and the potential contribution from emission lines in the wings of the BP1191-4 bandpass, we take the sky radiance model of ESO SkyCalc (S. Noll et al. 2012; A. Jones et al. 2013) for La Silla. We do not know the exact quantum efficiency figure for our detector but assume it to be 65% in the range of 0.5–2.6 μm. Assuming 95% reflectivity on the telescope mirrors, 99% transmission on all lenses, and 7.2% Fresnel losses on the KDP window, we estimate the sky lines in the wings of the BP1191-4 filter bandpass to contribute ∼9×10^{-4}ADU s^{-1} px^{-1} to the measured sky surface brightness. Likewise, the integrated sky emission outside of the BP1191-4 bandpass would contribute ∼1×10^{-3}ADU s^{-1} px^{-1}. The transmission and reflectivity figures are optimistic and should give an upper limit on the excess sky contribution. We conclude that we do not see significant amount of unwanted light in our measurement.

H. T. Nguyen et al. (2016) has measured 18.8 mag arcsec^{-2} in a bandpass similar to ours at the Table Mountain Observatory, Big Pines, California. Other narrowband measurements in a similar bandpass, have measured a brighter sky surface brightness of ∼17.5 mag arcsec^{-2} (see B. Milvang-Jensen et al. 2013, for a compilation). Spectroscopic observations of P. W. Sullivan & R. A. Simcoe (2012) at Las Campanas, Chile indicate similar values, with a median dark time sky continuum brightness of 18.6 mag arcsec^{-2}. S. Noll et al. (2024) gives a yearly average continuum background of 230 ph s^{-1}m^{-2}μm^{-1}arcsec^{-2}, or 19.8 mag arcsec^{-2} at 1.191 μm for Cerro Paranal, Chile. The differences might be explainable by the climatological variability of the hydroperoxyl continuum emission (S. Noll et al. 2025).

5. DISCUSSION

5.1. *KDP as a thermal blocking filter*

We have demonstrated that KDP can be deployed effectively to reduce unwanted thermal leaks. We achieve a reduction of 4.5 magnitudes in the NOTCam Z band sky surface brightness comparing observation with and without the 0.5 mm thick KDP (Table 3, Fig. A3). The reduction is significant and illustrates the potential of KDP for thermal blocking, or heat absorbing, purposes in astronomical instrumentation. We do not see thermal emission contribution from our warm NB filter. This opens a possibility to place NB filters outside of the cryostat, allowing exchanging them without breaking the cryo-vacuum.

5.2. *Possibilities in filter design*

KDP and its isomorphisms open up new possibilities for NIR filter design since they can be used as a short-pass filter 'glass'. We have designed and demonstrated

[3] https://irsa.ipac.caltech.edu/applications/BackgroundModel/

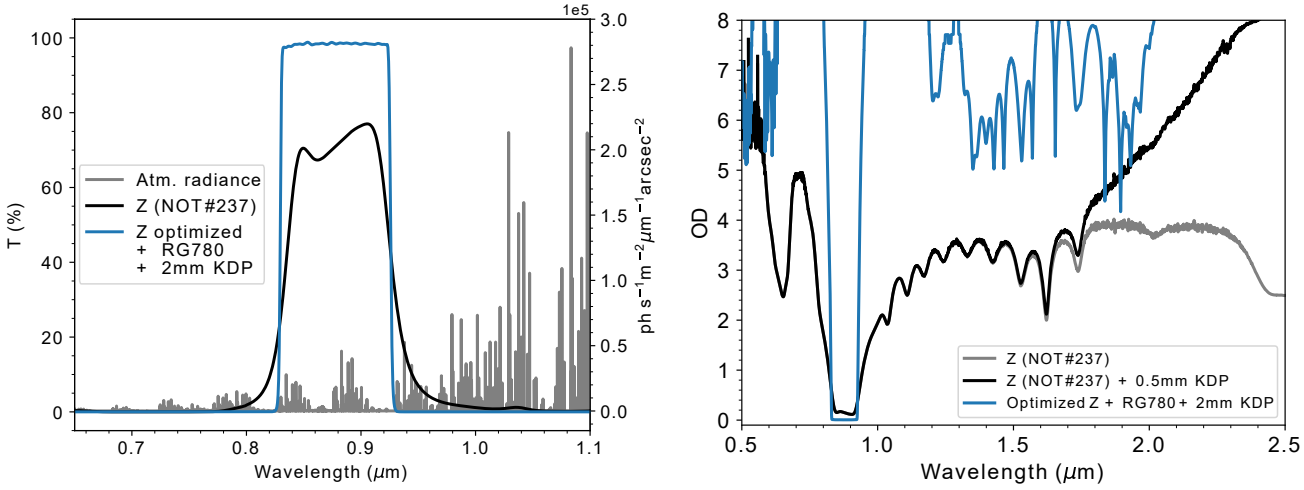

(a) (b)

Figure 4. Transmission and off-band blocking of the NOTCam Z band and the NOTCam Z band in combination with KDP used in this study (a). An optimized Z band coating design utilizing KDP as a short pass filter 'glass' is illustrated (b) Optical density of the NOT #237 Z band without KDP (grey), with KDP (black), and an optimized Z band coating (blue).

Table 4. Average sky surface brightness in our observations, and the KDP window transmission in the bandpasses

	Z	Y	J	H	K	J+BP1191-4
	#237	#236	#201	#203	#207	
Sky with KDP	17.8	17.1	16.1	14.1	12.3	18.5
Sky without KDP	13.3	16.9	15.6	13.9	12.5	18.4
Transmission	92%	89%	91%	64%	<0.2%	92%

NOTE—Surface brightnesses given in mag arcsec^{-2} (Vega). The KDP windows have not been anti-reflection coated, and the reported transmission includes reflection losses totaling 7.4 % on the two surfaces. The large difference in the Z band sky brightness is expected due to the large amount of red leak in the NOT #237 filter which is blocked by the KDP.

use of a highly efficient narrowband filter operating outside the instrument cryostat (Fig. 3). Furthermore, we show a design for a highly optimized 'blue' NIR filter to be used with a 2.5 μm cutoff HgCdTe detector. The implementation of the Z band (UKIDSS Z[4], P. C. Hewett et al. (2006)) allows high peak transmission, and well defined bandpass edges due to the relaxed blocking requirements of the dielectric coating at wavelengths >1.9 μm, and high off-band blocking density due to KDP (Fig. 4).

[4] http://www.ukidss.org/technical/instrument/filters.html

5.3. *Alternative materials*

We are not aware any other materials than the KDP and its isomorphisms that absorb thermal IR photons as effectively while, being transparent in the NIR and bluer wavelengths. The heat absorbing glasses offered by several major glass manufacturers have high optical density only at wavelengths >2.7 μm, and significantly lower transmission in the NIR range. Compared to a typical heat absorbing glass, KDP offers a longer cutoff wavelength, and orders of magnitude higher optical density at wavelengths longer than 1.8 μm. Based on Table 1, we identify KDA and RDA as potential mate-

rials candidates for NIR shortpass filter, due to their lower than KDP Curie temperature, and suitable cutoff wavelength. We have not tested these materials, and they are not as easily available as KDP.

5.4. *Possible caveats*

KDP contains Potassium which has radioactive isotopes. The radioactive decay leads to particle events observable by the photo-detectors if not shielded by a cover glass. KDP is a birefringent material, and the cutoff wavelength λ_{SP} has a polarization dependence, which may affect some use cases. KDP is also water soluble (M. J. Weber 1994), and a certain amount of care should be taken handling it.

6. CONCLUSION

We have shown that the KDP is an excellent thermal blocking filter and practical to use in an astronomical context, with limitation on its operating temperature, and birefringence. KDP offers good optical characteristics, and can strongly reduce atmospheric or instrumental thermal background. We have demonstrated the use of a warm narrow band filter in conjunction with a 2.5 μm cutoff detector, which has been enabled by the high thermal IR absorbance of the KDP. While we cannot demonstrate a photometric gain in the warm narrowband over the J band, we have measured the airglow continuum brightness within the bandpass, and find it to be 18.5 mag arcsec^{-2}. KDP has the potential to become a mainstay in the SWIR astronomy as a heat absorbing, thermal emission blocking, shortpass filter material. It offers a way to improve the SWIR broad- and especially narrowband filter efficiency, and off-band blocking characteristics, can be used for enhancing performance of existing instrumentation suffering from thermal leaks, and has potential for realizing new instrument concepts.

DATA AVAILABILITY

Data are available upon reasonable request from the corresponding author and the Nordic Optical Telescope's FITS-file archive. Software is available from the corresponding author upon reasonable request.

ACKNOWLEDGMENTS

Cosmic Dawn Center (DAWN) is funded by the Danish National Research Foundation under grant DNRF140. We thank C. Pérez, T. Pursimo, G. Cox, P. Brandt, A. Kasikov, P. Galindo-Guil, M. Keniger, J. Saario, A. M. Kadela, and A. Henderson de la Fuente for their assistance at the NOT, Instituto de Astrofísica de Canarias (IAC) IACTEC optical laboratory for the Z and Y-band filter scans, and V. Pinter and A. E. T. Viitanen for their feedback on the manuscript.

AUTHOR CONTRIBUTIONS

MIA conceptualized the project. JPUF acquired hardware funding for the project. JKMV managed the project. JKMV, AAD, and SA recorded the observatory site data. JKMV and AAD processed and analyzed the data. ANS and MIA carried out the thermal analysis. DK and PS recorded the optical density data, and designed and manufactured the NB filter. JKMV wrote the original draft. All authors contributed equally to the review and editing.

Facilities: NOT (NOTCam)

Software: Astropy (Astropy Collaboration et al. 2013, 2018, 2022), Astroquery (A. Ginsburg et al. 2019), Matplotlib (J. D. Hunter 2007), Numpy (C. R. Harris et al. 2020), Reproject[5]

[5] https://github.com/astropy/reproject

APPENDIX

A. INSTRUMENT SETUP

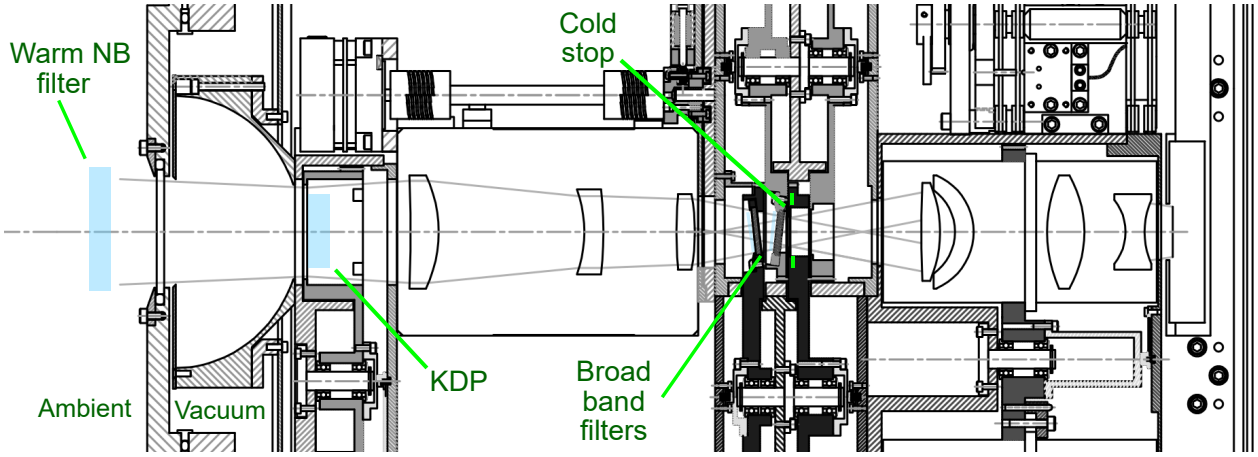

Figure A1. Schematic layout of the NOTCam optics, and the additional optical components used in this study. The warm NB filter was installed in the telescope converging beam, outside of the instruments' cryostat window. The telescope focus is placed right after NOTCam's entrance baffle. The KDPs were installed in the aperture wheel placing them in the telescope focus. Broadband filters were installed in their standard location in the NOTCam parallel beam with a 5° tilt respective to the optical axis.

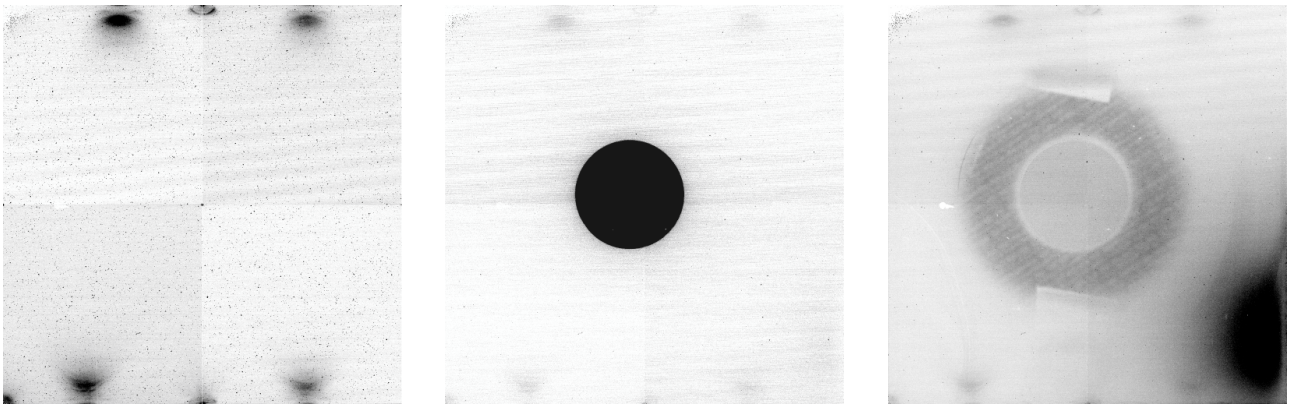

(a) (b) (c)

Figure A2. Inverted grayscale illustration of detector illumination. (a) dark frame, (b) J-band sky image showing the restricted image circle when the fiberglass insulated KDP is placed in the beam, and (c) K band integration showing a light leak from adjacent aperture, and partially transparent fiberglass holder. Integration times and color scales are not equal in the three panels.

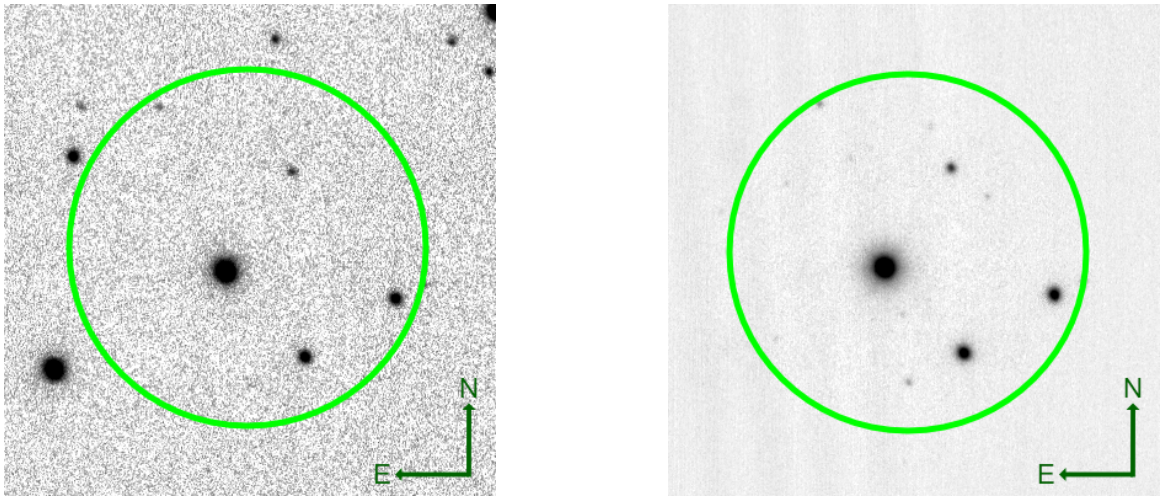

(a) (b)

Figure A3. RL 149 field observed without (a), and with (b) KDP in the NOTCam Z band. SNR increase is clear in the images with equal equal integration times, and equal logarithmic color scale. Size of KDP image circle is indicated by a green circle.

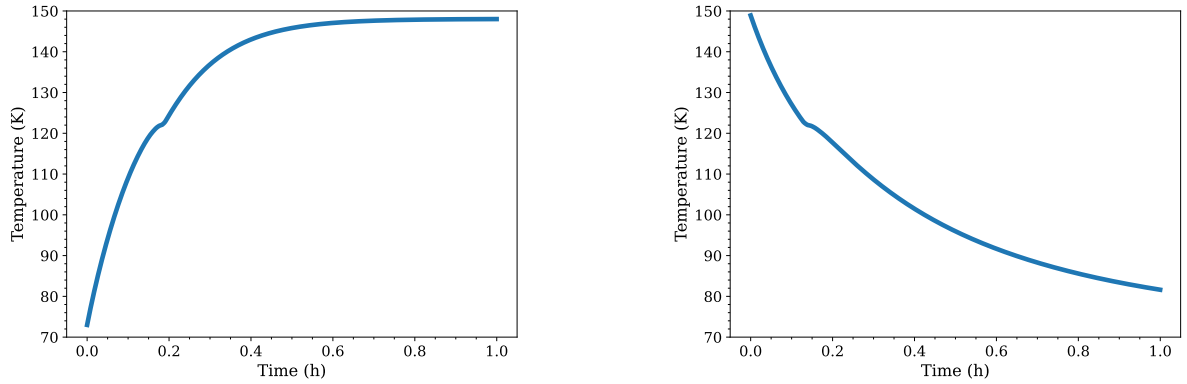

(a) (b)

Figure A4. Calculated temperature of the 0.5 mm KDP thick fiber glass insulated in the NOTCam aperture wheel, radiatively warming up when moved in the telescope beam (a), and cooling cool down when moving out of telescope beam (b). The heat capacity of KDP has an anomaly close to its T_C (C. C. Stephenson & J. G. Hooley 1944), causing a small kink in the temperature.

B. KDP OPTICAL DENSITY DATA

REFERENCES

Abbott, T. M., Aspin, C., Sorensen, A. N., et al. 2000, in Society of Photo-Optical Instrumentation Engineers (SPIE) Conference Series, Vol. 4008, Optical and IR Telescope Instrumentation and Detectors, ed. M. Iye & A. F. Moorwood, 714–719, doi: 10.1117/12.395528

Amado, P. J., Lenzen, R., Cardenas, M. C., et al. 2012, in Modern Technologies in Space- and Ground-based Telescopes and Instrumentation II, ed. R. Navarro, C. R. Cunningham, & E. Prieto, Vol. 8450, International Society for Optics and Photonics (SPIE), 84501U, doi: 10.1117/12.928619

Table B1. Optical density of a 1 mm thick KDP measured with unpolarized light, *continues* in Table B2

λ (μm)	OD	λ (μm)	OD	λ (μm)	OD	λ (μm)	OD	λ (μm)	OD	λ (μm)	OD
0.299	0.0028	0.467	0.0003	0.635	0.0001	0.803	0.0002	0.971	0.0008	1.139	0.0020
0.302	0.0027	0.470	0.0001	0.638	0.0001	0.806	0.0003	0.974	0.0008	1.142	0.0021
0.305	0.0025	0.473	0.0004	0.641	0.0003	0.809	0.0006	0.977	0.0007	1.145	0.0021
0.308	0.0022	0.476	0.0004	0.644	0.0001	0.812	0.0005	0.980	0.0010	1.148	0.0019
0.311	0.0021	0.479	0.0002	0.647	0.0001	0.815	0.0003	0.983	0.0009	1.151	0.0021
0.314	0.0017	0.482	0.0001	0.650	0.0001	0.818	0.0002	0.986	0.0008	1.154	0.0022
0.317	0.0017	0.485	0.0002	0.653	0.0003	0.821	0.0006	0.989	0.0007	1.157	0.0023
0.320	0.0015	0.488	0.0001	0.656	0.0001	0.824	0.0007	0.992	0.0011	1.160	0.0022
0.323	0.0011	0.491	0.0001	0.659	0.0001	0.827	0.0006	0.995	0.0009	1.163	0.0024
0.326	0.0011	0.494	0.0002	0.662	0.0001	0.830	0.0002	0.998	0.0009	1.166	0.0024
0.329	0.0009	0.497	0.0004	0.665	0.0003	0.833	0.0003	1.001	0.0009	1.169	0.0022
0.332	0.0007	0.500	0.0005	0.668	0.0002	0.836	0.0003	1.004	0.0010	1.172	0.0022
0.335	0.0007	0.503	0.0005	0.671	0.0002	0.839	0.0004	1.007	0.0010	1.175	0.0022
0.338	0.0007	0.506	0.0007	0.674	0.0001	0.842	0.0002	1.010	0.0010	1.178	0.0025
0.341	0.0004	0.509	0.0007	0.677	0.0002	0.845	0.0002	1.013	0.0011	1.181	0.0026
0.344	0.0002	0.512	0.0004	0.680	0.0001	0.848	0.0004	1.016	0.0012	1.184	0.0026
0.347	0.0001	0.515	0.0005	0.683	0.0001	0.851	0.0001	1.019	0.0013	1.187	0.0026
0.350	0.0003	0.518	0.0001	0.686	0.0001	0.854	0.0001	1.022	0.0010	1.190	0.0027
0.353	0.0004	0.521	0.0002	0.689	0.0001	0.857	0.0008	1.025	0.0011	1.193	0.0029
0.356	0.0002	0.524	0.0005	0.692	0.0001	0.860	0.0006	1.028	0.0011	1.196	0.0030
0.359	0.0001	0.527	0.0001	0.695	0.0001	0.863	0.0005	1.031	0.0010	1.199	0.0029
0.362	0.0001	0.530	0.0001	0.698	0.0001	0.866	0.0005	1.034	0.0012	1.202	0.0031
0.365	0.0002	0.533	0.0004	0.701	0.0002	0.869	0.0004	1.037	0.0011	1.205	0.0033
0.368	0.0001	0.536	0.0004	0.704	0.0002	0.872	0.0006	1.040	0.0011	1.208	0.0035
0.371	0.0001	0.539	0.0001	0.707	0.0001	0.875	0.0002	1.043	0.0011	1.211	0.0033
0.374	0.0002	0.542	0.0001	0.710	0.0008	0.878	0.0003	1.046	0.0011	1.214	0.0035
0.377	0.0001	0.545	0.0002	0.713	0.0001	0.881	0.0001	1.049	0.0010	1.217	0.0035
0.380	0.0003	0.548	0.0003	0.716	0.0001	0.884	0.0004	1.052	0.0013	1.220	0.0036
0.383	0.0004	0.551	0.0001	0.719	0.0001	0.887	0.0002	1.055	0.0012	1.223	0.0038
0.386	0.0001	0.554	0.0001	0.722	0.0002	0.890	0.0003	1.058	0.0014	1.226	0.0040
0.389	0.0001	0.557	0.0001	0.725	0.0001	0.893	0.0002	1.061	0.0011	1.229	0.0041
0.392	0.0002	0.560	0.0001	0.728	0.0001	0.896	0.0006	1.064	0.0013	1.232	0.0042
0.395	0.0001	0.563	0.0001	0.731	0.0001	0.899	0.0004	1.067	0.0014	1.235	0.0045
0.398	0.0002	0.566	0.0004	0.734	0.0001	0.902	0.0004	1.070	0.0012	1.238	0.0046
0.401	0.0001	0.569	0.0002	0.737	0.0002	0.905	0.0003	1.073	0.0014	1.241	0.0047
0.404	0.0002	0.572	0.0001	0.740	0.0001	0.908	0.0006	1.076	0.0014	1.244	0.0048
0.407	0.0001	0.575	0.0001	0.743	0.0001	0.911	0.0004	1.079	0.0014	1.247	0.0050
0.410	0.0001	0.578	0.0001	0.746	0.0001	0.914	0.0004	1.082	0.0015	1.250	0.0051
0.413	0.0001	0.581	0.0004	0.749	0.0004	0.917	0.0005	1.085	0.0014	1.253	0.0054
0.416	0.0002	0.584	0.0003	0.752	0.0001	0.920	0.0007	1.088	0.0013	1.256	0.0057
0.419	0.0001	0.587	0.0001	0.755	0.0001	0.923	0.0006	1.091	0.0016	1.259	0.0057
0.422	0.0002	0.590	0.0001	0.758	0.0001	0.926	0.0007	1.094	0.0015	1.262	0.0058
0.425	0.0001	0.593	0.0001	0.761	0.0001	0.929	0.0005	1.097	0.0017	1.265	0.0059
0.428	0.0005	0.596	0.0001	0.764	0.0001	0.932	0.0009	1.100	0.0017	1.268	0.0063
0.431	0.0003	0.599	0.0001	0.767	0.0001	0.935	0.0004	1.103	0.0017	1.271	0.0066
0.434	0.0001	0.602	0.0002	0.770	0.0002	0.938	0.0006	1.106	0.0016	1.274	0.0069
0.437	0.0002	0.605	0.0001	0.773	0.0001	0.941	0.0005	1.109	0.0017	1.277	0.0072
0.440	0.0002	0.608	0.0001	0.776	0.0001	0.944	0.0008	1.112	0.0018	1.280	0.0074
0.443	0.0001	0.611	0.0001	0.779	0.0002	0.947	0.0007	1.115	0.0017	1.283	0.0077
0.446	0.0001	0.614	0.0004	0.782	0.0002	0.950	0.0008	1.118	0.0019	1.286	0.0079
0.449	0.0003	0.617	0.0004	0.785	0.0003	0.953	0.0006	1.121	0.0019	1.289	0.0082
0.452	0.0006	0.620	0.0002	0.788	0.0001	0.956	0.0008	1.124	0.0019	1.292	0.0084
0.455	0.0003	0.623	0.0002	0.791	0.0001	0.959	0.0006	1.127	0.0018	1.295	0.0089
0.458	0.0002	0.626	0.0001	0.794	0.0004	0.962	0.0008	1.130	0.0018	1.298	0.0093
0.461	0.0003	0.629	0.0001	0.797	0.0006	0.965	0.0008	1.133	0.0019	1.301	0.0095
0.464	0.0006	0.632	0.0001	0.800	0.0004	0.968	0.0009	1.136	0.0019	1.304	0.0100

NOTE—Fresnel losses corrected. Scans of 4 mm (<1.86 μm) and 0.5 mm (>1.86 μm) thick samples have been combined into a 1 mm equivalent optical density.

Astropy Collaboration, Robitaille, T. P., Tollerud, E. J., et al. 2013, A&A, 558, A33, doi: 10.1051/0004-6361/201322068

Astropy Collaboration, Price-Whelan, A. M., Sipőcz, B. M., et al. 2018, AJ, 156, 123, doi: 10.3847/1538-3881/aabc4f

Astropy Collaboration, Price-Whelan, A. M., Lim, P. L., et al. 2022, ApJ, 935, 167, doi: 10.3847/1538-4357/ac7c74

Baumeister, P. W. 2004, Optical Coating Technology (SPIE), 9–65, doi: 10.1117/3.548071

De Yoreo, J. J., Burnham, A. K., & Whitman, P. K. 2002, International Materials Reviews, 47, 113, doi: 10.1179/095066001225001085

Eimerl, D. 1987, Ferroelectrics, 72, 95, doi: 10.1080/00150198708017942

Ginsburg, A., Sipőcz, B. M., Brasseur, C. E., et al. 2019, AJ, 157, 98, doi: 10.3847/1538-3881/aafc33

Harris, C. R., Millman, K. J., van der Walt, S. J., et al. 2020, Nature, 585, 357, doi: 10.1038/s41586-020-2649-2

Haynes, W. M., Lide, D. R., Bruno, T. J., & Haynes, W. M. 2016, CRC Handbook of Chemistry and Physics, 97th edn. (Milton: CRC Press), doi: 10.1201/9781315380476

Hewett, P. C., Warren, S. J., Leggett, S. K., & Hodgkin, S. T. 2006, Monthly Notices of the Royal Astronomical Society, 367, 454, doi: 10.1111/j.1365-2966.2005.09969.x

Hunter, J. D. 2007, Computing In Science & Engineering, 9, 90

Janesick, J. R., Klaasen, K. P., & Elliott, T. 1987, Optical Engineering, 26, 972, doi: 10.1117/12.7974183

Jones, A., Noll, S., Kausch, W., Szyszka, C., & Kimeswenger, S. 2013, A&A, 560, doi: 10.1051/0004-6361/201322433

Kelsall, T., Weiland, J. L., Franz, B. A., et al. 1998, ApJ, 508, 44, doi: 10.1086/306380

Klougart, J. 1995, in Society of Photo-Optical Instrumentation Engineers (SPIE) Conference Series, Vol. 2416, Cameras and Systems for Electronic Photography and Scientific Imaging, ed. C. N. Anagnostopoulos & M. P. Lesser, 65–74, doi: 10.1117/12.204818

Kozlowski, L. J., Vural, K., Cabelli, S. A., et al. 1994, in Society of Photo-Optical Instrumentation Engineers (SPIE) Conference Series, Vol. 2268, Infrared Spaceborne Remote Sensing II, ed. M. S. Scholl, 353–364, doi: 10.1117/12.185846

Leggett, S. K., Currie, M. J., Varricatt, W. P., et al. 2006, MNRAS, 373, 781, doi: 10.1111/j.1365-2966.2006.11069.x

Milvang-Jensen, B., Freudling, W., Zabl, J., et al. 2013, A&A, 560, A94, doi: 10.1051/0004-6361/201321814

Moore, A. C., Ninkov, Z., & Forrest, W. J. 2006, Optical Engineering, 45, 076402, doi: 10.1117/1.2219103

Nguyen, H. T., Zemcov, M., Battle, J., et al. 2016, PASP, 128, 094504, doi: 10.1088/1538-3873/128/967/094504

Noll, S., Kausch, W., Barden, M., et al. 2012, A&A, 543, doi: 10.1051/0004-6361/201219040

Noll, S., Plane, J. M. C., Feng, W., et al. 2024, Atmospheric Chemistry and Physics, 24, 1143, doi: 10.5194/acp-24-1143-2024

Noll, S., Schmidt, C., Hannawald, P., Kausch, W., & Kimeswenger, S. 2025, Geoscientific Model Development, 18, 4353, doi: 10.5194/gmd-18-4353-2025

Simons, D. A., & Tokunaga, A. 2002, PASP, 114, 169, doi: 10.1086/338544

Stephenson, C. C., & Hooley, J. G. 1944, Journal of the American Chemical Society, 66, 1397, doi: 10.1021/ja01236a054

Sullivan, P. W., & Simcoe, R. A. 2012, PASP, 124, 1336, doi: 10.1086/668849

Tody, D. 1986, in Society of Photo-Optical Instrumentation Engineers (SPIE) Conference Series, Vol. 627, Instrumentation in astronomy VI, ed. D. L. Crawford, 733, doi: 10.1117/12.968154

Tody, D. 1993, in Astronomical Society of the Pacific Conference Series, Vol. 52, Astronomical Data Analysis Software and Systems II, ed. R. J. Hanisch, R. J. V. Brissenden, & J. Barnes, 173

Tokunaga, A. T., Simons, D. A., & Vacca, W. D. 2002, PASP, 114, 180, doi: 10.1086/338545

Tokunaga, A. T., & Vacca, W. D. 2005, PASP, 117, 421, doi: 10.1086/429382

Tulloch, S., George, E., & Systems Group, E. S. O. D. 2019, Journal of Astronomical Telescopes, Instruments, and Systems, 5, doi: 10.1117/1.Jatis.5.3.036004

Weber, M. J. 1994, Optical materials, The CRC Press laser and optical science and technology series (Boca Raton: CRC Press)

Weber, M. J. 2020, CRC Handbook of Laser Science and Technology, Vol. 8, CRC Handbook of Laser Science and Technology Supplement 2: Optical Materials, 1st edn. (United Kingdom: CRC Press)

Zernike, F. 1964, J. Opt. Soc. Am., 54, 1215, doi: 10.1364/JOSA.54.001215

Table B2. *continued* Optical density of a 1 mm thick KDP measured with unpolarized light

λ (μm)	OD	λ (μm)	OD	λ (μm)	OD	λ (μm)	OD	λ (μm)	OD	λ (μm)	OD
1.307	0.0104	1.478	0.0649	1.646	0.2952	1.814	1.1399	1.982	3.2434	2.150	5.2101
1.310	0.0108	1.481	0.0669	1.649	0.3028	1.817	1.1659	1.985	3.2774	2.153	5.2727
1.313	0.0110	1.484	0.0687	1.652	0.3107	1.820	1.1889	1.988	3.3078	2.156	5.2783
1.316	0.0116	1.487	0.0707	1.655	0.3188	1.823	1.2023	1.991	3.3062	2.159	5.3583
1.319	0.0121	1.490	0.0727	1.658	0.3273	1.826	1.2082	1.994	3.3412	2.162	5.3959
1.322	0.0125	1.493	0.0748	1.661	0.3356	1.829	1.2528	1.997	3.3750	2.165	5.4345
1.325	0.0130	1.496	0.0769	1.664	0.3444	1.832	1.2790	2.000	3.4118	2.168	5.5310
1.328	0.0133	1.499	0.0790	1.667	0.3637	1.835	1.2924	2.003	3.4846	2.171	5.5510
1.331	0.0137	1.502	0.0813	1.670	0.3657	1.838	1.3171	2.006	3.5629	2.174	5.5732
1.334	0.0142	1.505	0.0838	1.673	0.3717	1.841	1.3574	2.009	3.5559	2.177	5.6370
1.337	0.0149	1.508	0.0861	1.676	0.3809	1.844	1.3359	2.012	3.6307	2.180	5.6492
1.340	0.0155	1.511	0.0887	1.679	0.3910	1.847	1.4140	2.015	3.6527	2.183	5.7146
1.346	0.0167	1.514	0.0913	1.682	0.4009	1.850	1.4653	2.018	3.7075	2.186	5.8368
1.349	0.0172	1.517	0.0938	1.685	0.4117	1.853	1.4399	2.021	3.7453	2.189	5.8118
1.352	0.0177	1.520	0.0965	1.688	0.4221	1.856	1.6654	2.024	3.7523	2.192	5.8286
1.355	0.0185	1.523	0.0993	1.691	0.4331	1.859	1.6396	2.027	3.8201	2.195	6.0248
1.358	0.0191	1.526	0.1024	1.694	0.4442	1.862	1.5946	2.030	3.8257	2.198	6.0985
1.361	0.0195	1.529	0.1053	1.697	0.4557	1.865	1.5466	2.033	3.8843	2.201	6.0855
1.364	0.0201	1.532	0.1083	1.700	0.4674	1.868	1.6601	2.036	3.8609	2.204	6.0411
1.367	0.0210	1.535	0.1113	1.703	0.4795	1.871	1.8927	2.039	3.9120	2.207	6.1293
1.370	0.0218	1.538	0.1147	1.706	0.4922	1.874	1.9059	2.042	4.0072	2.210	6.2227
1.373	0.0223	1.541	0.1179	1.709	0.5046	1.877	1.8317	2.045	4.0850	2.213	6.3057
1.376	0.0230	1.544	0.1212	1.712	0.5174	1.880	1.8347	2.048	4.0586	2.216	6.3359
1.379	0.0239	1.547	0.1247	1.715	0.5305	1.883	1.8149	2.051	4.1152	2.219	6.4513
1.382	0.0247	1.550	0.1282	1.718	0.5438	1.886	1.8455	2.054	4.1394	2.222	6.5345
1.385	0.0255	1.553	0.1319	1.721	0.5579	1.889	1.9231	2.057	4.0972	2.225	6.4211
1.388	0.0263	1.556	0.1357	1.724	0.5716	1.892	1.8967	2.060	4.1658	2.228	6.4486
1.391	0.0271	1.559	0.1396	1.727	0.5858	1.895	1.8359	2.063	4.2442	2.231	6.6304
1.394	0.0282	1.562	0.1433	1.730	0.6002	1.898	1.9807	2.066	4.2802	2.234	6.7272
1.397	0.0293	1.565	0.1473	1.733	0.6150	1.901	2.0205	2.069	4.3018	2.237	6.7992
1.400	0.0301	1.568	0.1512	1.736	0.6302	1.904	2.0490	2.072	4.3405	2.240	6.8138
1.403	0.0309	1.571	0.1554	1.739	0.6455	1.907	2.1578	2.075	4.3691	2.243	6.8610
1.406	0.0319	1.574	0.1596	1.742	0.6613	1.910	2.1142	2.078	4.3937	2.246	6.8878
1.409	0.0329	1.577	0.1639	1.745	0.6776	1.913	2.1506	2.081	4.3751	2.249	6.9478
1.412	0.0339	1.580	0.1685	1.748	0.6940	1.916	2.0992	2.084	4.3999	2.252	7.0958
1.415	0.0350	1.583	0.1730	1.751	0.7108	1.919	2.2050	2.087	4.4605	2.255	7.0162
1.418	0.0363	1.586	0.1777	1.754	0.7280	1.922	2.3220	2.090	4.4735	2.258	7.0443
1.421	0.0373	1.589	0.1825	1.757	0.7453	1.925	2.4336	2.093	4.4799	2.261	7.2821
1.424	0.0384	1.592	0.1872	1.760	0.7632	1.928	2.4488	2.096	4.5179	2.264	7.2323
1.427	0.0397	1.595	0.1922	1.763	0.7811	1.931	2.4882	2.099	4.5217	2.267	7.4013
1.430	0.0408	1.598	0.1970	1.766	0.7995	1.934	2.5374	2.102	4.6067	2.270	7.4909
1.433	0.0420	1.601	0.2024	1.769	0.8182	1.937	2.6211	2.105	4.6508	2.273	7.5017
1.436	0.0433	1.604	0.2074	1.772	0.8378	1.940	2.6261	2.108	4.6394	2.276	7.2635
1.439	0.0446	1.607	0.2127	1.775	0.8574	1.943	2.7201	2.111	4.7220	2.279	7.2751
1.442	0.0461	1.610	0.2180	1.778	0.8777	1.946	2.7295	2.114	4.7638	2.282	7.2751
1.445	0.0474	1.613	0.2237	1.781	0.8981	1.949	2.7841	2.117	4.8012	2.285	7.4599
1.448	0.0488	1.616	0.2292	1.784	0.9183	1.952	2.7859	2.120	4.8308	2.288	7.2956
1.451	0.0504	1.619	0.2349	1.787	0.9379	1.955	2.8031	2.123	4.7988	2.291	7.4444
1.454	0.0517	1.622	0.2410	1.790	0.9578	1.958	2.9011	2.126	4.8946	2.294	7.6386
1.457	0.0530	1.625	0.2472	1.793	0.9776	1.961	2.9535	2.129	4.9920	2.297	7.5730
1.460	0.0545	1.628	0.2536	1.796	0.9969	1.964	3.0751	2.132	4.9930	2.300	7.9230
1.463	0.0563	1.631	0.26 0	1.799	1.0161	1.967	2.9675	2.135	5.0087	2.303	7.9608
1.466	0.0580	1.634	0.2667	1.802	1.0636	1.970	3.0119	2.138	5.0393	2.306	7.8872
1.469	0.0596	1.637	0.2734	1.805	1.0805	1.973	3.0760	2.141	5.0473	2.309	7.9740
1.472	0.0613	1.640	0.2805	1.808	1.1011	1.976	3.1396	2.144	5.0733	2.312	8.0710
1.475	0.0630	1.643	0.2879	1.811	1.1207	1.979	3.1690	2.147	5.1257	2.315	8.1818

NOTE—Fresnel losses corrected. Scans of 4 mm (<1.86 μm) and 0.5 mm (>1.86 μm) thick samples have been combined into a 1 mm equivalent optical density.

Article IV

On the airglow continuum –
Non-scattered light biased measurement in the range 5500–11 000Å
J. K. M. Viuho, J. P. U. Fynbo, and M. I. Andersen

In preparation

Draft version December 2, 2025
Typeset using LaTeX **twocolumn** style in AASTeX7.0.1

On the airglow continuum
Non-scattered light biased measurement in the range 5500–11 000 Å

Joonas K. M. Viuho [1,2,3,4] Michael I. Andersen [1,2] and Johan P. U. Fynbo [1,2]

[1] *Cosmic Dawn Center (DAWN)*
[2] *Niels Bohr Institute, University of Copenhagen, Jagtvej 155A, 2. floor, 2200 Copenhagen N., Denmark*
[3] *Nordic Optical Telescope, Rambla José Ana Fernández Pérez 7, ES-38711 Breña Baja, Spain*
[4] *Department of Physics and Astronomy, Aarhus University, Munkegade 120, DK-8000 Aarhus C, Denmark*

ABSTRACT

The level of near infrared (NIR, 7000 – 11 000 Å) airglow continuum has been discussed in the literature for the several decades. Due to its faintness and variability, its measure has remained a challenge to quantify. The airglow continuum emission sets the observational limits for the ground-based spectroscopy, and understanding its origins and behaviour is of fundamental interest for the planning the Extremely Large Telescope (ELT) observation. It has been suggested in the literature that the airglow continuum can be confounded with the grating scattered light, a form of stray light that all dispersion grating spectrographs produce. We aim to measure the airglow continuum within the wavelength range detecable with a silicon photo-detector in a non-grating scattered light biased way. We observe the airglow continuum with a novel spectrograph design that purpose-built for the airglow continuum measurement. The spectrograph designs re-directs the grating scattered light away from the dispersion axis. We measure the airglow continuum at the site of Observatorio del Roque de los Muchachos (ORM), La Palma, Spain. We reach a detection of the airglow continuum in the range 5500 – 9600 Å, and derive an upper limit in the range from 9600 – 11 000 Å where our system has lower sensitivity. Our experiment solves the question if the airglow continuum is an instrumental artefact or real atmospheric emission: the airglow continuum is clearly visible and separable from the grating scattered light. We report our finding in attempting to identify spectrl features of FeO, NiO, NO, and HO_2 to determine the origin of the airglow continuum at the site of ORM.

Keywords: Near infrared astronomy (1093) — Astronomical instrumentation (799) — Astronomical optics (88) — Spectroscopy (1558) — Diffuse radiation (383)

1. INTRODUCTION

The level of the VIS – NIR[1] airglow continuum has been a subject of several earlier studies (A. L. Broadfoot & K. R. Kendall 1968; J. R. Sternberg & M. F. Ingham 1972; M. Gadsden & E. Marovich 1973; P. C. Wraight 1977; J. F. Noxon 1978; V. G. Sobolev 1978; R. W. Hanuschik 2003; S. Noll et al. 2024; J. K. M. Viuho et al. 2025), while the more recent studies on the airglow continuum level have focused on the SWIR wavelengths (T. Maihara et al. 1993; P. W. Sullivan & R. A. Simcoe 2012; S. C. Ellis et al. 2012; C. Q. Trinh et al. 2013; E. Oliva et al. 2015; H. T. Nguyen et al. 2016; S. Noll et al. 2024, 2025).

The NIR airglow continuum is faint ($<$800 ph s^{-1}m^{-2}μm^{-1}arcsec^{-2}) making its level challenging to quantify. It has been argued that the expected airglow continuum value would be significantly lower than what has been measured and tentatively this is due to extended wings of several line spread profiles of atmospheric sky lines (S. C. Ellis & J. Bland-Hawthorn 2008). In the SWIR wavelenghts, it has been shown that the continuum can be consistent with the grating scattered light (P. W. Sullivan & R. A. Simcoe 2012). The origin of the grating scattered light is the atmospheric hydroxyl (OH) lines, which very bright and cover the entire NIR – SWIR range (f.e. S. Adler-Golden 1997; J. S. A. Brooke et al. 2016; S. Noll et al. 2017).

Several continuum emission processes are know to contribute to the airglow continuum radiance. At least ni-

Corresponding author: Joonas K. M. Viuho
Email: joonas.viuho@nbi.ku.dk

[1] We define the spectral ranges referred to often in the following way: visible 4000–7000 Å (VIS), near-infrared (NIR) 7000–11 000 Å, and short-wave infrared (SWIR) 1.1–3 μm.

trogen monoxide (NO) (R. L. Gattinger et al. 2010), iron monoxide (FeO) (S. Unterguggenberger et al. 2017), nickel monoxide (NiO) (W. F. J. Evans et al. 2011), and hydroperoxyl (HO_2) (S. Noll et al. 2025) emit (pseudo)continuum at the NIR wavelengths, and have been identified in the night sky spectrum. The spectral features of FeO and NiO are similar making the two difficult to distinguish from each other (W. F. J. Evans et al. 2011; S. Unterguggenberger et al. 2017). Also, there seems geographical (f.e. R. L. Gattinger et al. 2010) and temporal (S. Noll et al. 2025) dependence on the preferred emission mechanism.

While the OH line emission is not as strong in the NIR as it is at longer wavelenghts, the grating scattered light from the bright OH lines still remains as a potential confounding factor in the airglow continuum measurement. To alleviate the issue, we have designed and built a spectrograph that re-directs the scattered light away from the dispersion axis and apply it to study the airglow continuum (M. I. Andersen & J. Andersen 1992; J. Viuho et al. 2022). Similar concept can be used for a future airglow spectrograph designed to operate in the SWIR to reliable measure the continuum. We measure at the site of Observatorio del Roque de los Muchachos (ORM) where only a few similar studies have been made previosly (E. Oliva et al. 2015; J. K. M. Viuho et al. 2025).

2. EXPERIMENTAL SETUP

SKy Is The Limit Echelle Spectrograph (SKITLES) optical design has been described in an earlier paper (J. Viuho et al. 2022). The design concept is a white-pupil echelle spectrograph (A. Baranne 1972), which uses its grating in double pass. A right-angle prism is passed between the two consecutive passes on the grating, resulting into the spectrum and the grating scattered light emerging to different angles M. I. Andersen & J. Andersen (1992); J. Viuho et al. (2022). The result is a high purity spectrum that is recorded in a single exposure. We call the design *double-X-dispersed* spectrograph due to the two dispersion taking place in 90° angle respective to each other. This gives the spectrograph Point Spread Function (PSF) also its characteristic X-shaped look (Fig. 2). The design alleviates the grating scattered light problem as described by S. C. Ellis & J. Bland-Hawthorn (2008), and the resulting spectrum is almost as clean as that of a double-pass scanning spectrograph (f.e. Coude Echelle Spectrometer (CES), D. Enard 1982). The scattered light performance of the spectrograph is limited by the 2D diffuse scattering from the grating, dust, and surface roughness of the optical elements.

The spectrograph is combined with a 2" diameter doublet lens acting as a telescope. Despite the small collecting, the focal length of 750 mm combined with 20″entrance aperture on the sky offers a large etendue allowing detection of the faint airglow continuum. The large etendue also dilutes any star light entering the spectrograph.

SKITLES uses first a generation Andor iXon DU-888 with an E2V CCD201-20 as its detector. Andor feature baseline clamp was used to rectify the DC offsets of the bias level, and the detector overscan regions were used as a reference to monitor frame-to-frame bias level variation. Electron Multiplication CCDs (EMCCDs) have a readout register with very high avalanche gain, rendering readout noise negligible allowing statistical photon counting.

3. OBSERVATIONS

The observations were made at the Observatorio del Roque de los Muchachos (ORM), La Palma, Canary Islands, Spain at the premises of the Nordic Optical Telescope (NOT) located at the geographical coordinates +28°45′26.2″ N, 17°53′06.3″ W at an altitude of 2382 m. NOT and its instrument ALFOSC were used for transferring flux calibrations. SKITLES was located in the mechanical workshop at the Northern end of NOT service building. The SKITLES telescope faced directly towards North. The observations took place on 17–18 November 2022.

On 17 November 2022, the afternoon sky was observed as a common references source for transfering absolute flux calibration to SKITLES. Both ALFOSC and SKITLES monitored the same patch of sky during the sunset for a duration of 15'. Thin high clouds were present on 17 November 2022, and the SKITLES observations were repeated on 18 November 2022 under photometric condition and completely clear horizon.

4. STATISTICAL PHOTON-COUNTING

Individual exposures of 180 s were recorded continuously, and the flux λ was derived by using threholding method for statistical photon counting (K. B. W. Harpsøe et al. 2012). K. B. W. Harpsøe et al. (2012) gives best estimator $E(\hat{\lambda})$ and variance $Var(\hat{\lambda})$ for thresholding.

$$E\left(\hat{\lambda}\right) = -\sum_{Q=0}^{Q} \ln\left(\frac{N-Q}{N}\right)\binom{N}{Q} p_\lambda^Q (1-p_\lambda)^{N-Q} \quad (1)$$

$$Var\left(\hat{\lambda}\right) = \sum_{Q=0}^{Q} \left(-\ln\left(\frac{N-Q}{N}\right) - \hat{\lambda}\right)^2 \binom{N}{Q} p_\lambda^Q (1-p_\lambda)^{N-Q} \quad (2)$$

in which p_λ is

$$\begin{aligned} p_\lambda \quad &= e^{-T/\gamma}(1-e^{-\hat{\lambda}}) \\ &+\tfrac{e^{-\hat{\lambda}}-mp_{sCIC}}{2}\left(1-erf\left(\tfrac{T}{\sigma\sqrt{2}}\right)\right) \\ &+p_{sCIC}\textstyle\sum_{k=1}^{m}(1-e^{-T/\gamma_{m-k}})e^{-\hat{\lambda}} \end{aligned} \tag{3}$$

Photon counted sky spectrum is shown in the Fig 1, and a wavelenght calibration lamp is shown in Fig 2. The tresholding photon-counting method has been implemented as a part of a software package *pc-em-tools*[2].

5. CONCLUSION

We observe a clear continuum in the range 5500 – 9800 Å in our photon-counted. The observation is done low in the horizon, away from the ecliptic and Milky Way plane. We have a direct continuum detection without any ambiguity regarding the grating scattered light. Our system sensitivity does not allow a measurement of the airglow continuum beyond 9800 Å, but an upper bound on the level of airglow continuum can be determined in the range 9800 – 11 000 Å.

Facilities: NOT (ALFOSC)

Software: Astropy (Astropy Collaboration et al. 2013, 2018, 2022), Astroquery (A. Ginsburg et al. 2019), Matplotlib (J. D. Hunter 2007), Numpy (C. R. Harris et al. 2020), Reproject[3]

[2] https://github.com/JoJoScholarly/pc-em-tools/releases/tag/v0.1.1-beta

[3] https://github.com/astropy/reproject

REFERENCES

Adler-Golden, S. 1997, Journal of Geophysical Research: Space Physics, 102, 19969, doi: 10.1029/97ja01622

Andersen, M. I., & Andersen, J. 1992, in ESO Workshop on High Resolution Spectroscopy with the VLT, Vol. 40, 235

Astropy Collaboration, Robitaille, T. P., Tollerud, E. J., et al. 2013, A&A, 558, A33, doi: 10.1051/0004-6361/201322068

Astropy Collaboration, Price-Whelan, A. M., Sipőcz, B. M., et al. 2018, AJ, 156, 123, doi: 10.3847/1538-3881/aabc4f

Astropy Collaboration, Price-Whelan, A. M., Lim, P. L., et al. 2022, ApJ, 935, 167, doi: 10.3847/1538-4357/ac7c74

Baranne, A. 1972, in Auxiliary instrumentation for large telescopes, ed. S. Laustsen & R. A. (ESO/CERN), 227–239

Broadfoot, A. L., & Kendall, K. R. 1968, J. Geophys. Res., 73, 426, doi: 10.1029/JA073i001p00426

Brooke, J. S. A., Bernath, P. F., Western, C. M., et al. 2016, Journal of Quantitative Spectroscopy and Radiative Transfer, 168, 142, doi: https://doi.org/10.1016/j.jqsrt.2015.07.021

Ellis, S. C., & Bland-Hawthorn, J. 2008, MNRAS, 386, 47, doi: 10.1111/j.1365-2966.2008.13021.x

Ellis, S. C., Bland-Hawthorn, J., Lawrence, J., et al. 2012, MNRAS, 425, 1682, doi: 10.1111/j.1365-2966.2012.21602.x

Enard, D. 1982, in Society of Photo-Optical Instrumentation Engineers (SPIE) Conference Series, Vol. 331, Instrumentation in Astronomy IV, ed. D. L. Crawford, 232–242, doi: 10.1117/12.933460

Evans, W. F. J., Gattinger, R. L., Broadfoot, A. L., & Llewellyn, E. J. 2011, Atmospheric Chemistry and Physics, 11, 9595, doi: 10.5194/acp-11-9595-2011

Gadsden, M., & Marovich, E. 1973, Journal of Atmospheric and Terrestrial Physics, 35, 1601, doi: 10.1016/0021-9169(73)90179-7

Gattinger, R. L., McDade, I. C., Alfaro Suzán, A. L., et al. 2010, Journal of Geophysical Research: Atmospheres, 115, doi: 10.1029/2009jd013205

Ginsburg, A., Sipőcz, B. M., Brasseur, C. E., et al. 2019, AJ, 157, 98, doi: 10.3847/1538-3881/aafc33

Hanuschik, R. W. 2003, A&A, 407, 1157, doi: 10.1051/0004-6361:20030885

Harpsøe, K. B. W., Andersen, M. I., & Kjægaard, P. 2012, A&A, 537, A50, doi: 10.1051/0004-6361/201117089

Harris, C. R., Millman, K. J., van der Walt, S. J., et al. 2020, Nature, 585, 357, doi: 10.1038/s41586-020-2649-2

Hunter, J. D. 2007, Computing In Science & Engineering, 9, 90

Maihara, T., Iwamuro, F., Yamashita, T., et al. 1993, PASP, 105, 940, doi: 10.1086/133259

Nguyen, H. T., Zemcov, M., Battle, J., et al. 2016, PASP, 128, 094504, doi: 10.1088/1538-3873/128/967/094504

Noll, S., Kimeswenger, S., Proxauf, B., et al. 2017, Journal of Atmospheric and Solar-Terrestrial Physics, 163, 54, doi: 10.1016/j.jastp.2017.05.012

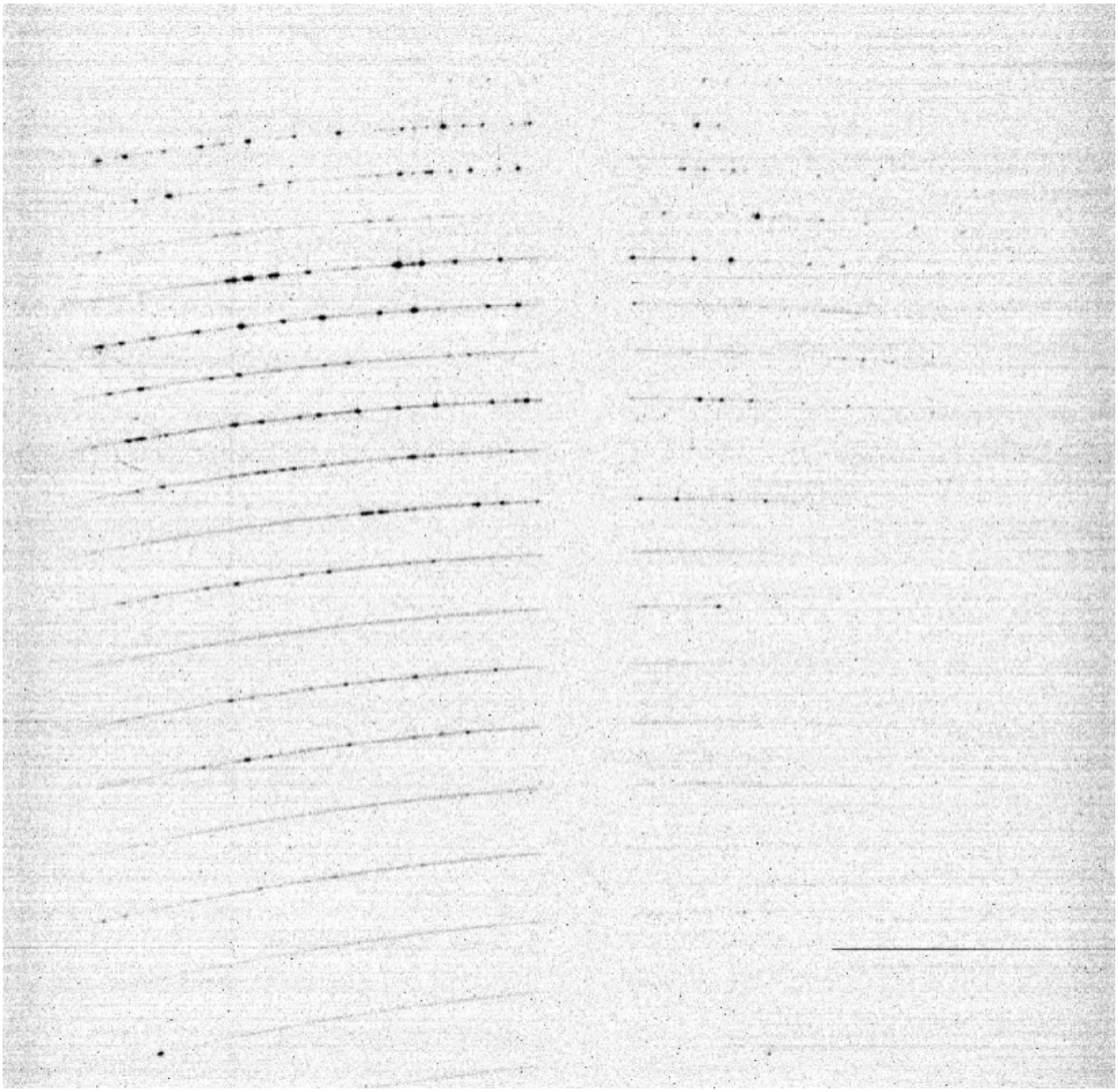

Figure 1. Thresholding photon counted 2D spectrum of the airglow. Both the airglow lines and the continuum are present. Due to the double-X-dispersed design, the continuum cannot be due to the grating scattered light. Shadow of the input folding prism can be seen as cut of the trace at the center of the detector.

Noll, S., Plane, J. M. C., Feng, W., et al. 2024, Atmospheric Chemistry and Physics, 24, 1143, doi: 10.5194/acp-24-1143-2024

Noll, S., Schmidt, C., Hannawald, P., Kausch, W., & Kimeswenger, S. 2025, Geoscientific Model Development, 18, 4353, doi: 10.5194/gmd-18-4353-2025

Noxon, J. F. 1978, Planetary and Space Science, 26, 191, doi: 10.1016/0032-0633(78)90019-3

Oliva, E., Origlia, L., Scuderi, S., et al. 2015, A&A, 581, A47, doi: 10.1051/0004-6361/201526291

Sobolev, V. G. 1978, Planetary and Space Science, 26, 703, doi: 10.1016/0032-0633(78)90103-4

Sternberg, J. R., & Ingham, M. F. 1972, MNRAS, 159, 1, doi: 10.1093/mnras/159.1.1

Sullivan, P. W., & Simcoe, R. A. 2012, PASP, 124, 1336, doi: 10.1086/668849

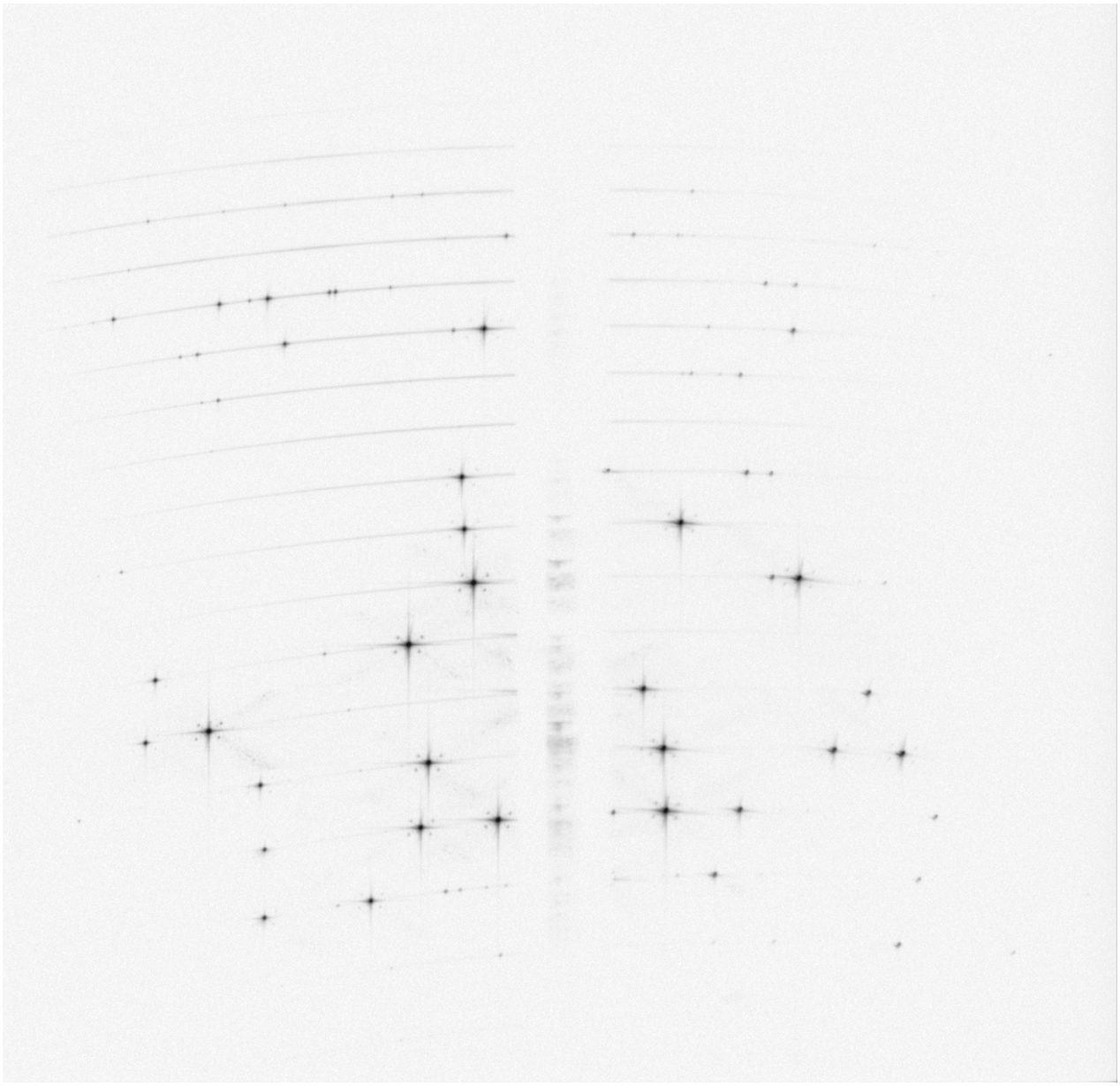

Figure 2. Neon lamp spectra for wavelength calibration. The grating scattered light and the Rowland ghosts are visible in the proximity of the brightest emission lines.

Trinh, C. Q., Ellis, S. C., Bland-Hawthorn, J., et al. 2013, MNRAS, 432, 3262, doi: 10.1093/mnras/stt677

Unterguggenberger, S., Noll, S., Feng, W., et al. 2017, Atmospheric Chemistry and Physics, 17, 4177, doi: 10.5194/acp-17-4177-2017

Viuho, J., Andersen, M. I., & Fynbo, J. U. 2022, Measuring the near-IR airglow continuum with stray light reduced spectrograph, doi: 10.1117/12.2630668

Viuho, J. K. M., Fynbo, J. P. U., & Andersen, M. I. 2025, A&A, 699, doi: 10.1051/0004-6361/202553726

Wraight, P. C. 1977, Planetary and Space Science, 25, 787, doi: 10.1016/0032-0633(77)90130-1